DYNAMICS AT THE GAS LIQUID INTERFACE:
QUANTUM STATE RESOLVED STUDIES OF DCL, CO AND OCS

by

TIMOTHY ANDREW LIVINGSTON LARGE

B.S., University of Washington, 2013

A thesis submitted to the
Faculty of the Graduate School of the
University of Colorado in partial fulfillment
of the requirement for the degree of
Doctor of Philosophy
Department of Physics
2021

Committee Members:

David Nesbitt

Heather Lewandowski

Eric Cornell

J. Mathias Weber

Carl Lineberger

Livingston Large, Timothy Andrew (Ph.D., Physics)

Dynamics at the Gas Liquid Interface: Quantum State Resolved Studies of DCl, CO and OCS

Thesis directed by Professor David J. Nesbitt

The gas-liquid interface is explored via quantum state resolve direct absorption molecular beam scattering. Both rovibrational populations and Doppler profiles are measured in order to elucidate the dynamics at the gas-liquid interface. This work explores the collisional dynamics between several different molecules (DCl, CO and OCS) and the liquid surface of the three prototypical liquid scattering surfaces (PFPE, glycerol and squalane) as function of both the incident collisional energy and the temperature of the surface. Each of these molecules has had an interesting story to tell.

The scattering of deuterium chloride (DCl) was shown to follow the known empirical scattering pathways. These can be split up into two distinct paradigms, thermal desorption (TD) where molecules collide with the surface, trap in the surfaces bound well, thermalize with the surface and then desorb at the temperature of the surface, and impulsive scattering (IS) where molecules hits the surface hard, undergoes a few collisions and then scatters from the surface. In this IS pathway, empirically it has been seen that the molecules scatter with a rotational distribution that is temperature-like but hotter than the surface. It was shown that a simple impulsive scattering model of DCl, when convolved with gaussian distributed surface roughness, can predict a temperature like rotational distribution. Carbon monoxide scattering from these prototypical liquids showed behavior that did not follow the two temperature model. At low collision energies, a sub thermal scattering pathway was discovered. By comparing molecular dynamics between molecules that undergo TD dynamics and CO, it was proposed that due to the shallow attractive interaction CO undergoes with the surface is not deep enough for CO to promote the TD pathway and thus a low energy IS pathway is probably seen. Due to the low energy vibrations of OCS, populated vibrational states can be observed in both the incident and the outgoing molecules. Low

energy collisional studies showed that vibrational energy transfer does not occur for TD trajectories. At high collisional energies, the same behavior was seen for the IS pathway. Remarkably, at these high energies, it was shown the vibrational energy transfer occurs along the TD pathway.

To Oscar,

Acknowledgements

I could not have earned a Ph.D. without the generous support of those around me. I have the sincerest gratitude to my research advisor, David J. Nesbitt. Through his gifts of time and mentorship, he has help shape me into the scientist I am today. He has taught me the importance of clear communication and I shall always strive to be a clearer communicator. I would also like to thank him for his kindness and support during some of the difficult life events that have happened during graduate school.

My work at JILA could not have occurred without the help and support of all the staff at JILA. They make it a wonderful place to work. I would especially like to thank Hans Green of the machine shop and Terry Brown and Carl Sauer of the electronics shop. Through years of my near constant questions, some of their extensive knowledge of the practical world has rubbed off on me. Without their help, my experiment would be a much poorer version of itself.

I would like to thank the Nesbitt group members, past and present, for the years of good discussions, friendship, and support. You guys have made this time I have spent here quite fun.

And finally, I would like to thank my family and friends for all their support over the years. I could not do this alone and I am so glad I had you guys.

CONTENTS

CHAPTER

VII.

APPENDIX

TABLES

FIGURES

Chapter 1

Introduction

Dynamics at the gas-liquid interface play a crucial role in many important chemical environments, from atmospheric chemistry and environmental science, to catalysis and other engineering fields.[1-6] Interfaces play a particularly crucial role in heterogeneous chemistry, often providing reagents with lower barrier pathways toward chemical reactions that might be kinetically unfavorable in the gas phase. Due to the complexity of the liquids surface, the dynamics of these systems is not well known, and thus are a worthwhile system to study.

To understand the interface between the liquid and gas phases, we must first have some understanding of what the liquid interface looks like on its own. When one looks at the surface of a lake or pond on a windless day, you will see a pristine flat surface. However, any perturbation of the surface will generate waves that travel across the surface. These ripples are a form of capillary waves. These are waves on a liquid surface whose dynamics are significantly dominated by the effects of surface tension. However, even on a perfectly still day, the liquid surface will not be perfectly flat. Thermal fluctuations constantly perturb and roughen the surface. For the length scales of these experiments, the dynamics of capillary waves can be broken up into two ranges, gravity-capillary waves and proper capillary waves. These both behave very similarly with the only difference being that at longer length scales, the restoring force of gravity compared to surface tension become comparable thus the dispersion relationship of the gravity-capillary waves depends on both of these forces. The only importance of this is that without any directional restoring force (like gravity), there would be no well defined flat surface. As has been seen in many a space station video in microgravity, a liquid without any restoring force will curl up in a ball due to the surface tension relaxing the liquid into the lowest energy shape with the ratio of surface area to volume being maximized. This restoring force does not have to be gravity. Since the key importance of this regime for us is that a directional force defines the plane of the surface, any force that prevents the liquid from balling up will work. For our vertical liquid surfaces, the self adhesion of the liquid to itself and the adhesion to the rotating glass wheel helps define the plane of the liquid interface.

This continuum model of capillary waves is quite good at describing the physics of the liquid interface. However, because it is a continuum model, there is going to be some short length scale at which it fails. To understand where this occurs, a more complete model of the surface is needed.[7-8] To achieve this, viscous damping can be added, which primarily affects the model at short length and time scales (which will be defined below). When one treats this problem completely, the damping coefficient grows with increasing momentum until the system moves from an underdamped regime, where damping is only a minor perturbation, to an overdamped regime, where the viscous damping damps out all frequencies that are too high or the length scales are too short. By setting both the characteristic pressures and characteristic timescales for both capillary and viscous forces to be equal, we can calculate the viscocapillary (vc) length and time scales. The vc length scale is $l_{vc} = \frac{\mu^2}{\sigma\,\rho}$ and the time scale is $t_{vc} = \frac{\mu^3}{\sigma^2\,\rho}$ where μ is the dynamical viscosity, σ is the surface tension and ρ is the mass density of the liquid. These length and time scales vary wildly, with water having one of the fastest timescales and the shortest lengths scales. For water, this damping length scale is 74 nm with an upper allowed frequency of 2.5 GHz. On the other side of the viscosity scale, glycerol has a transition length scale of 14 cm with an upper frequency of 0.9 Hz. As we can see, these scales vary all over the range of interest. Since even the shortest length scales for water are much larger than the size of the molecules and atoms that make

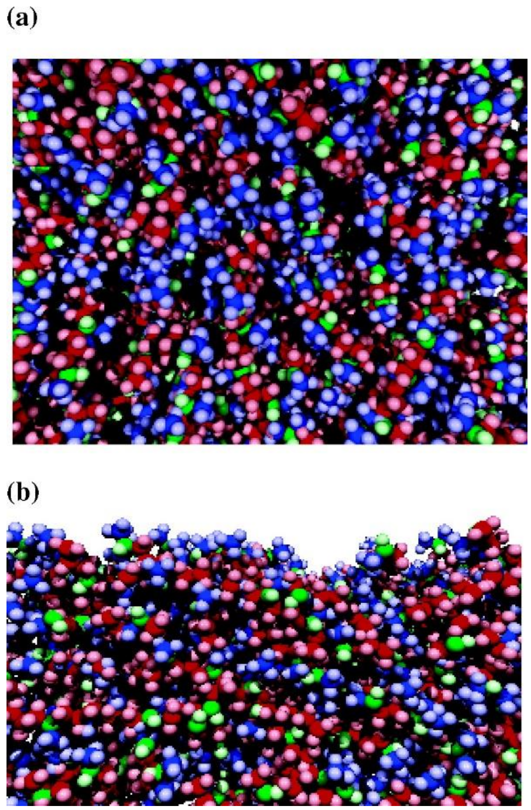

Figure 1.1 :Snapshot of the liquid squalane surface at 298. Dark blue spheres are primary carbon atoms, red spheres are secondary, and green spheres are tertiary carbon atoms. Hydrogen atoms, inserted retrospectively, are represented in the respective lighter color. (a) Plan view along *z*-axis and (b) side view along *y*-axis. "Reprinted with permission from *J. Phys. Chem. B* 2006, 110, 24, 11717-11724. Copyright 2006 American Chemical Society.

up the surface, this length scale allows for a clear demarcation between these continuum models and a full molecular representation at the shortest of length scales. At this time, there is no complete theory of the liquid surface which included all details of the local molecular motion due to the extreme complexity with many degrees of freedom and low symmetry preventing simplification. One way around this is to simulate a small part of the liquid surface using molecular dynamics[9-13]. The Minton group has run some molecular dynamics simulations of a squalane surface where figure 1.1 shows a vertical slice through this surface[12] and shows visually how complicated the local surface structure is. Unlike solid surfaces where, generally, surface reorganization happens quite slowly, locking the surface into a fixed configuration, liquid surfaces have a much faster reorganization time, which means that a set static configuration for a liquid surface is not possible to generate. All thermodynamically allowed surface configurations would appear with thermal weighting in the measurement region of most experiments. Thus, we can see that understanding the liquid interface requires both understanding the local structure of the surface but also the macroscopic properties of the liquid.

Gas-liquid surface scattering is a relatively young field at least in comparison to the rest of surface science. Since isolating bare liquid surfaces has required cleverness and improvements in vacuum technology, it only has been in the last 20-30 years that this problem has received appreciable attention from the research community. To understand how atoms and molecules interact with the liquid surface, a two pathway empirical paradigm has been used by the community[14]. These two pathways have been summarized in figure 1.2. Early work with atomic-liquid interface scattering detected by time of flight mass spectroscopy has shown that the velocity

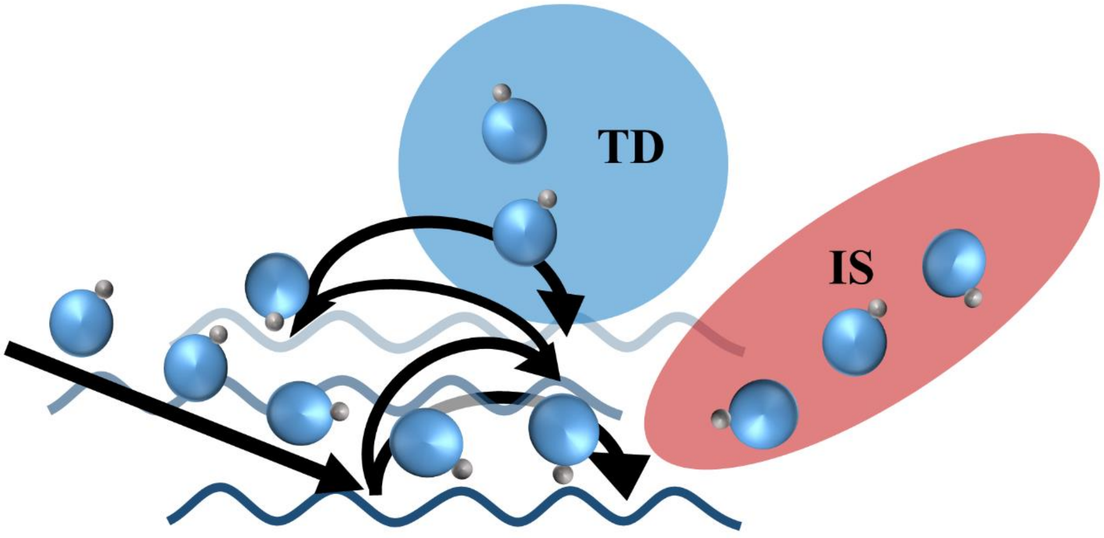

Figure 1.2 a diagrammatic representation of both the TD and IS pathways. "Reprinted with permission from *J. Phys. Chem. C* 2019, 123, 6, 3449–3460. Copyright 2019 American Chemical Society."

distribution can be broken up into a fast component with peaked velocity distribution and a slower component that matches with a thermal Maxwell-Boltzmann distribution[15-18]. As the collision energy decreases, this fast component both slows down and decreases in intensity implying that at low enough energies, only the thermal component will survive. When Perkins from the Nesbitt group extended these studies to molecules, it was seen that this two pathway paradigm survives.[9, 14, 19-26] Using the molecule CO_2, Perkins saw that the lower energy pathway is thermal in both the translational and rotational degrees of freedom. This pathway has been given the name thermal desorption (TD). This is where a molecule collides with the surface, dissipating enough of the collisional translational energy to be trapped in the local van der Waals surface well. In this well, it interacts with the surface long enough to exchange energy and become thermalized to the surface. It then goes through a barrierless exit channel and appears as thermal rotational and translational distributions effectively evaporating from the surface. Typically, everything else that does not scatter via the TD pathway is considered part of the impulsive scattering (IS) pathway. Even though this is a less rigorous scattering pathway, it does have some well defined characteristics. Translationally, one expects a non-thermal translational distribution whose central velocity scales with the beam energy. Rotationally, one sees a thermal-like rotational distribution. However, this “temperature” is not necessarily a rigorous temperature a priori but more a measure of average rotational energy. This pathway generally retains more energy than kT_s and thus clearly does not have sufficient time to come to equilibrium with the surface. This pathway is for all the molecules that do not trap and thermalize. They collide with the surface and exchange energy but they do not interact long enough with the surface to lose all “memory” of their initial conditions. By understanding this empirical model and where it fails, we can develop a better understanding of collision dynamics at the gas-liquid interface.

The structure of the rest of the thesis is as follows. Chapter 2 will discuss some of the improvements and changes that have been made to the experimental apparatus. Chapter 3 will explore the dynamics of DCl scattering and how thermal averaging of simple impulsive collisional models can generate temperature-like rotational distributions. Chapter 4 discusses the curious case of CO. In this chapter, it is shown that the weak attractive forces between the surface and the CO molecule turn off the trapping part of the TD channel, leaving only a single sub-thermal IS channel. Chapter 5 explores low energy collision of OCS with the liquid surface and how little to no vibrational energy transfer occurs even though thermalization was seen with respect to the rotational degrees of freedom. Chapter 6 explores higher energy scattering of OCS. Like the TD channel of the lower energy studies, the IS channel does not exchange vibrational energy with the surface. However, TD pathway shows markedly different behavior, with the vibrational degrees of freedom nearly completely thermalizing with the surface. The dynamical behavior of the TD pathway appears to conflict with the “memoryless” behavior that has been previously seen and assumed, thus implying that there is more to understand about the dynamics of this simple pathway.

Chapter 1 References

1. Kolb, C. E., et al., An Overview of Current Issues in the Uptake of Atmospheric Trace Gases by Aerosols and Clouds. *Atmos. Chem. Phys.* **2010**, *10*, 10561-10605.
2. Worsnop, D. R.; Zahniser, M. S.; Kolb, C. E.; Vandoren, J.; Davidovits, P., Uptake of Gaseous HNO_3, N_2O_5, and HCl into Sulfuric-Acid Droplets. *Abstr. Pap. Am. Chem. S.* **1990**, *200*, 122-Phys.
3. Watson, L. R.; Vandoren, J. M.; Davidovits, P.; Worsnop, D. R.; Zahniser, M. S.; Kolb, C. E., Uptake of HCl Molecules by Aqueous Sulfuric-Acid Droplets as a Function of Acid Concentration. *J. Geophys. Res.-Atmos.* **1990**, *95*, 5631-5638.
4. Vandoren, J. M.; Watson, L. R.; Davidovits, P.; Worsnop, D. R.; Zahniser, M. S.; Kolb, C. E., Temperature-Dependence of the Uptake Coefficients of HNO_3, HCl, and N_2O_5 by Water Droplets. *J. Phys. Chem.* **1990**, *94*, 3265-3269.
5. Hammerich, A. D.; Finlayson-Pitts, B. J.; Gerber, R. B., Mechanism for Formation of Atmospheric Cl Atom Precursors in the Reaction of Dinitrogen Oxides with HCl/Cl^- on Aqueous Films. *Phys. Chem. Chem. Phys.* **2015**, *17*, 19360-19370.
6. Hammerich, A. D.; Finlayson-Pitts, B. J.; Gerber, R. B., NO_x Reactions on Aqueous Surfaces with Gaseous HCl: Formation of a Potential Precursor to Atmospheric Cl Atoms. *J. Phys. Chem. Lett.* **2012**, *3*, 3405-3410.
7. Denner, F.; Pare, G.; Zaleski, S., Dispersion and Viscous Attenuation of Capillary Waves with Finite Amplitude. *Eur. Phys. J.-Spec. Top.* **2017**, *226*, 1229-1238.
8. Denner, F., Frequency Dispersion of Small-Amplitude Capillary Waves in Viscous Fluids. *Phys. Rev. E* **2016**, *94*.
9. Nogueira, J. J.; Vazquez, S. A.; Mazyar, O. A.; Hase, W. L.; Perkins, B. G.; Nesbitt, D. J.; Martinez-Nunez, E., Dynamics of CO_2 Scattering Off a Perfluorinated Self-Assembled Monolayer. Influence of the Incident Collision Energy, Mass Effects, and Use of Different Surface Models. *J. Phys. Chem. A* **2009**, *113*, 3850-3865.
10. Martinez-Nunez, E.; Rahaman, A.; Hase, W. L., Chemical Dynamics Simulations of CO_2 Scattering Off a Fluorinated Self-Assembled Monolayer Surface. *J. Phys. Chem. C* **2007**, *111*, 354-364.
11. Zhang, J. M.; Upadhyaya, H. P.; Brunsvold, A. L.; Minton, T. K., Hyperthermal Reactions of O and O_2 with a Hydrocarbon Surface: Direct C-C Bond Breakage by O and H-Atom Abstraction by O_2. *J. Phys. Chem. B* **2006**, *110*, 12500-12511.
12. Kohler, S. P. K.; Reed, S. K.; Westacott, R. E.; McKendrick, K. G., Molecular Dynamics Study to Identify the Reactive Sites of a Liquid Squalane Surface. *J. Phys. Chem. B* **2006**, *110*, 11717-11724.
13. Wiens, J. P.; Nathanson, G. M.; Alexander, W. A.; Minton, T. K.; Lakshmi, S.; Schatz, G. C., Collisions of Sodium Atoms with Liquid Glycerol: Insights into Solvation and Ionization. *J. Am. Chem. Soc.* **2014**, *136*, 3065-3074.
14. Perkins, B. G.; Haber, T.; Nesbitt, D. J., Quantum State-Resolved Energy Transfer Dynamics at Gas-Liquid Interfaces: IR Laser Studies of CO_2 Scattering from Perfluorinated Liquids. *J. Phys. Chem. B* **2005**, *109*, 16396-16405.
15. King, M. E.; Nathanson, G. M.; Hanninglee, M. A.; Minton, T. K., Probing the Microscopic Corrugation of Liquid Surfaces with Gas-Liquid Collisions. *Phys. Rev. Lett.* **1993**, *70*, 1026-1029.

16. Saecker, M. E.; Nathanson, G. M., Collisions of Protic and Aprotic Gases with Hydrogen-Bonding and Hydrocarbon Liquids. *J. Chem. Phys.* **1993**, *99*, 7056-7075.
17. Saecker, M. E.; Nathanson, G. M., Collisions of Protic and Aprotic Gases with a Perfluorinated Liquid. *J. Chem. Phys.* **1994**, *100*, 3999-4005.
18. King, M. E.; Fiehrer, K. M.; Nathanson, G. M.; Minton, T. K., Effects of Thermal Roughening on the Angular Distributions of Trapping and Scattering in Gas-Liquid Collisions. *J. Phys. Chem. A* **1997**, *101*, 6556-6561.
19. Perkins, B. G.; Nesbitt, D. J., Quantum-State-Resolved CO_2 Scattering Dynamics at the Gas-Liquid Interface: Incident Collision Energy and Liquid Dependence. *J. Phys. Chem. B* **2006**, *110*, 17126-17137.
20. Perkins, B. G.; Nesbitt, D. J., Quantum-State-Resolved CO_2 Scattering Dynamics at the Gas-Liquid Interface: Dependence on Incident Angle. *J. Phys. Chem. A* **2007**, *111*, 7420-7430.
21. Perkins, B. G.; Nesbitt, D. J., Correlated Angular and Quantum State-Resolved CO_2 Scattering Dynamics at the Gas-Liquid Interface. *J. Phys. Chem. A* **2008**, *112*, 9324-9335.
22. Perkins, B. G.; Nesbitt, D. J., Stereodynamics in State-Resolved Scattering at the Gas-Liquid Interface. *P. Natl. Acad. Sci. USA* **2008**, *105*, 12684-12689.
23. Perkins, B. G.; Nesbitt, D. J., Quantum State-Resolved CO_2 Collisions at the Gas-Liquid Interface: Surface Temperature-Dependent Scattering Dynamics. *J. Phys. Chem. B* **2008**, *112*, 507-519.
24. Perkins, B. G.; Nesbitt, D. J., Toward Three-Dimensional Quantum State-Resolved Collision Dynamics at the Gas-Liquid Interface: Theoretical Investigation of Incident Angle. *J. Phys. Chem. A* **2009**, *113*, 4613-4625.
25. Perkins, B. G.; Nesbitt, D. J., Stereodynamics at the Gas-Liquid Interface: Orientation and Alignment of CO_2 Scattered from Perfluorinated Liquid Surfaces. *J. Phys. Chem. A* **2010**, *114*, 1398-1410.
26. Perkins, B. G.; Nesbitt, D. J., High Resolution Dopplerimetry of Correlated Angular and Quantum State-Resolved CO_2 Scattering Dynamics at the Gas-Liquid Interface. *Phys. Chem. Chem. Phys.* **2010**, *12*, 14294-14308.

Chapter 2

Experimental

The experiments in this thesis were performed with the same direct absorption spectroscopy apparatus. Dr. Brad Perkins originally designed and developed the apparatus and a detailed description of the spectrometer and scattering chamber can be found in his thesis.[1] The sample holder was upgraded by Andrew Gisler and a description of this lazy Susan sample holder can be found in the following paper[2]. Several major upgrades have been performed in pursuit of this thesis and shall be discussed in this chapter.

2.1 Quantum Cascade Lasers

Quantum cascade laser (QCL) diodes are modern bandgap engineered diodes[3-4]. They are still fairly new devices with many kinks to be worked out, but they open the possibilities of easier single frequency access to midinfrared light. Unlike cryogenic lead salt diode lasers, these diodes can be operated at room temperature, making them more practical and robust. When several thin layers (<10's of nanometers) of different semiconductors with differing bandgaps are layered next to each other, a set of "particle-in-a-finite-well" states are created in both the conduction and valence band of this semiconductor system. These are called quantum wells. By varying the thickness of both the wells and the barriers, a coupled system of finite wells can be engineered. Because this system's properties are only weakly dependent on the semiconductor material properties and strongly on the organization of these thin layers, many of the important properties can be designed to specifications rather than having to rely on material properties found in nature. A standard diode laser emits light when an electron is driven across the bandgap from the conduction band to the valence band, emitting a single photon of light. This is quite different from

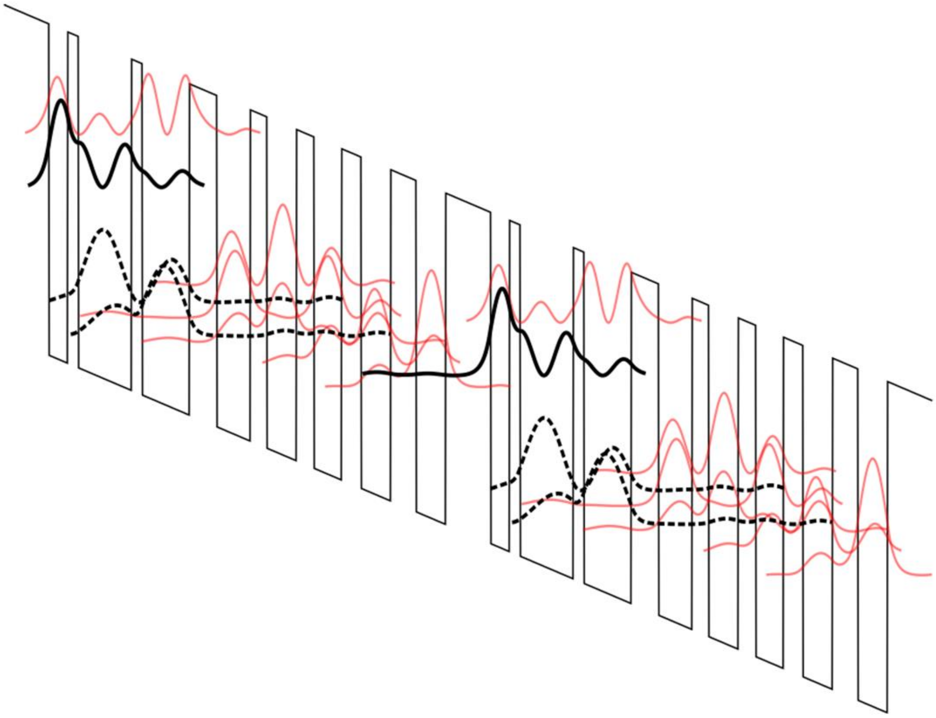

Figure 2.1 An example QCL diode interband structure. Solid black lines show the upper lasing levels while the dotted line show the lower lasing levels. Other allowed states in the system are shown in red. This figure is used under GNU Free Documentation License and is attributed to Evans82 at English Wikipedia

how a quantum cascade laser works, which use subband transitions between the engineered levels in the semiconductor device. When one applies a strong enough voltage to one of these patterned quantum well devices, these particle in a well states get shifted by a strong linear voltage gradient across the device. This can be seen in figure 2.1. If designed properly, this can create a quantum well that has an optical transition across a predefined energy gap. If multiple of these wells are put next to each other, an electron can undergo an optical transition, be captured in the lower state and be injected into the next well's lasing level. This allows for one electron to generate multiple photons of a designed wavelength. This has the added benefit of allowing these devices to generally be operated at room temperature. With a normal midinfrared laser diode, the thermal energy at room temperature would populate the conduction band enough to turn off the population inversion and quench the lasing. With a QCL, the bottom couple of rungs of the staircase will be thermally populated, but because there are multiple wells on top of each other, there are still lasing levels that can generate light.

For our specific laser systems, we use a QCL diode inside of an external cavity laser (ECQCL). The specific lasers that are used are Daylight Solution's single frequency mode hop free tuning laser. These laser diodes are broadband emitting laser diodes whose frequency is narrowed by using a grating to feedback the light. These lasers are in a double Littrow cavity configuration. A Littrow cavity feeds the first order diffraction peak from the grating back into the diode to create a cavity. Unlike the normal Littrow cavity where the output coupler is the zeroth order diffraction peak from the grating, the light is taken out of the backside of the diode. This preserves many of the advantageous tuning properties of a Littrow cavity, while removing the beam steering that occurs due to turning the grating to tune the laser. An important part of our spectroscopic data collection is the ability to scan over a frequency range without hopping to a different laser mode at a different frequency. This can be minimized by tuning all the laser's cavity conditions at the same rate. This is called mode hop free tuning. In an ideal world, a Littrow cavity diode laser can be designed to support only one laser mode over its entire tuning range. In practice, this is difficult. With proper design, Daylight Solutions has been able to provide a laser that can continuously tune for around 1 cm^{-1} before it undergoes a mode hop. This is done this by balancing the two important cavity conditions while tuning, the optical length of the cavity and the angle at which the laser light diffracts off the tuning grating. In practice, there are other engineering concerns that must be balanced when building a laser, but the general idea is that the rotational pivot point of the grating needs to be along the plane of the grating and slightly past the back facete of the diode (optical length of the cavity from the grating surface along the optical axis of laser).

This reliance on the grating for frequency selection has some downsides. One of the major downsides is that the laser frequency acquires sensitivities to mechanical noise and vibrations. This is made even worse by the fact that the grating plus its tuning mechanism has an underdamped response function with a Q of at least 10 and a resonant frequency at ~ 240 Hz. This low frequency mechanical resonance means that the mechanical vibrations and external noise can couple directly into the frequency of the laser. This has been mitigated by several strategies, which boil down to mechanically isolating the laser system from the rest of the experiment. To eliminate coupling from the optics table and all other devices on the optics table, the laser is supported on sorbethane feet with the correct amount of additional weight to damp most low frequency vibrations between

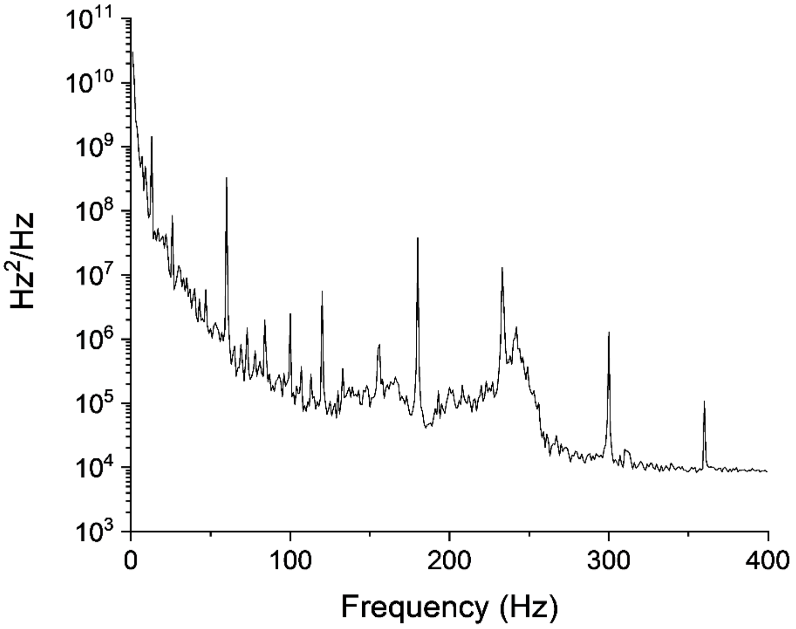

Figure 2.2 Laser Frequency noise spectral density. Three major features can be seen. i.) the mechanical resonance of the grating tuning mechanism at 240 Hz, ii.) 60 Hz line noise through from the current controller, and iii.) 1/f pickup noise.

the laser and the table. This isolation was enhanced by damping all vibrations that travel along the power and cooling cables by securing them in vibrationally dampening foam secured to the optics table. The final step was to reduce the noise that travelled through the cooling water itself. This is accomplished by turning down cooling pump speed to the minimal value that achieves the required cooling of the laser, while imparting the least amount of turbulence on the water itself. Figure 2.2 shows the frequency noise spectral density. There are several noise sources that are identified. As mentioned above, the noise around 240 Hz comes from the mechanical resonance of the grating. It has the characteristic form of a mechanical resonance and matches well with the sensitivity plot measured from the PZT tuning of the laser. Another identified source of noise is bleed through of 60 Hz line noise and its harmonics (120, 180, 240, 300, 360, etc.) from the laser current controller. The final source of noise that has been identified is 1/f noise that is picked up by the grating. A significate proportion of this noise comes from the turbulence of the water cooling system. Though this has been reduced, it can be reduced further by turning off the cooling pump. This is not a solution to this problem because the laser absolutely needs water cooling to prevent thermal overload of the system. If one only considers the noise above a KHz, the laser has a linewidth on order only a couple of MHz but due to the low frequency noise, this fairly narrow laser wanders over ~5-15 MHz depending on the stability of the cavity at a frequency and how well the isolation is working. Without isolation, linewidths of 25-75 MHz were seen.

Two different QCL diode are used for the experiments in this thesis. The original diode is used for the DCl work in chapter 3, with the newer diode for the CO and OCS work in chapter 4-6. The original diode tuning range is from 2075 to 2275 cm^{-1} with ~ 100 mW of infrared light across the spectrum. In the summer of 2015, the laser cavity was sent off to Daylight Solutions to tune up the laser cavity, since the tuning range was creeping in from the edges of the spectrum.

After realignment during their normal thermal cycling tests, the diode underwent thermal overload and was destroyed. They could not replace this diode and after 6 months or more of negotiations, a new diode was chosen. This diode covers a range of 1980 – 2200 cm^{-1} with an average power of ~300 mW. However, this laser is significantly red shifted from the previous laser preventing access to all DCl's states above R(13). Thus, with the new laser, the target molecules of choice shifted to CO and OCS, which have redshifted band origins compared to DCl. One must be careful when operating in the lower part of the frequency range of the new diode. The antireflection coating of the diode is not perfect in this region thus the laser frequency can get caught on diode modes and mode hop quite frequently between two modes 10 cm^{-1} apart. This can be mitigated by shifting around the temperatures of either the diode (by controlling the TEC setpoint) and/or the base of the laser cavity (by changing the temperature setpoint of the cooling water). This can shift around the alignment enough to prevent mode hops in the region of interest at the cost of moving them to other frequency regions.

2.2 Spectrometer

A simplified schematic of the optical table can be seen in figure 2.3a. Since the light generated in the ECQCL is several orders of magnitude more powerful than what is usable in these experiments, the power is cut by a factor of ~50 by a weak reflection from a tilted BaF window and then adjustably by crossed Rochon polarizers. This leaves, after transmission through the rest of the system, ~10-50 uW on each of our LN_2 cooled InSb photodetectors. This power level is chosen to maximize the power on the detectors while minimizing the nonlinearity of the photodetectors. Our frequency diagnostics comes in three pieces. We use a commercial wavemeter as rough calibration of our spectrum. This traveling Michelson interferometer, similar to others

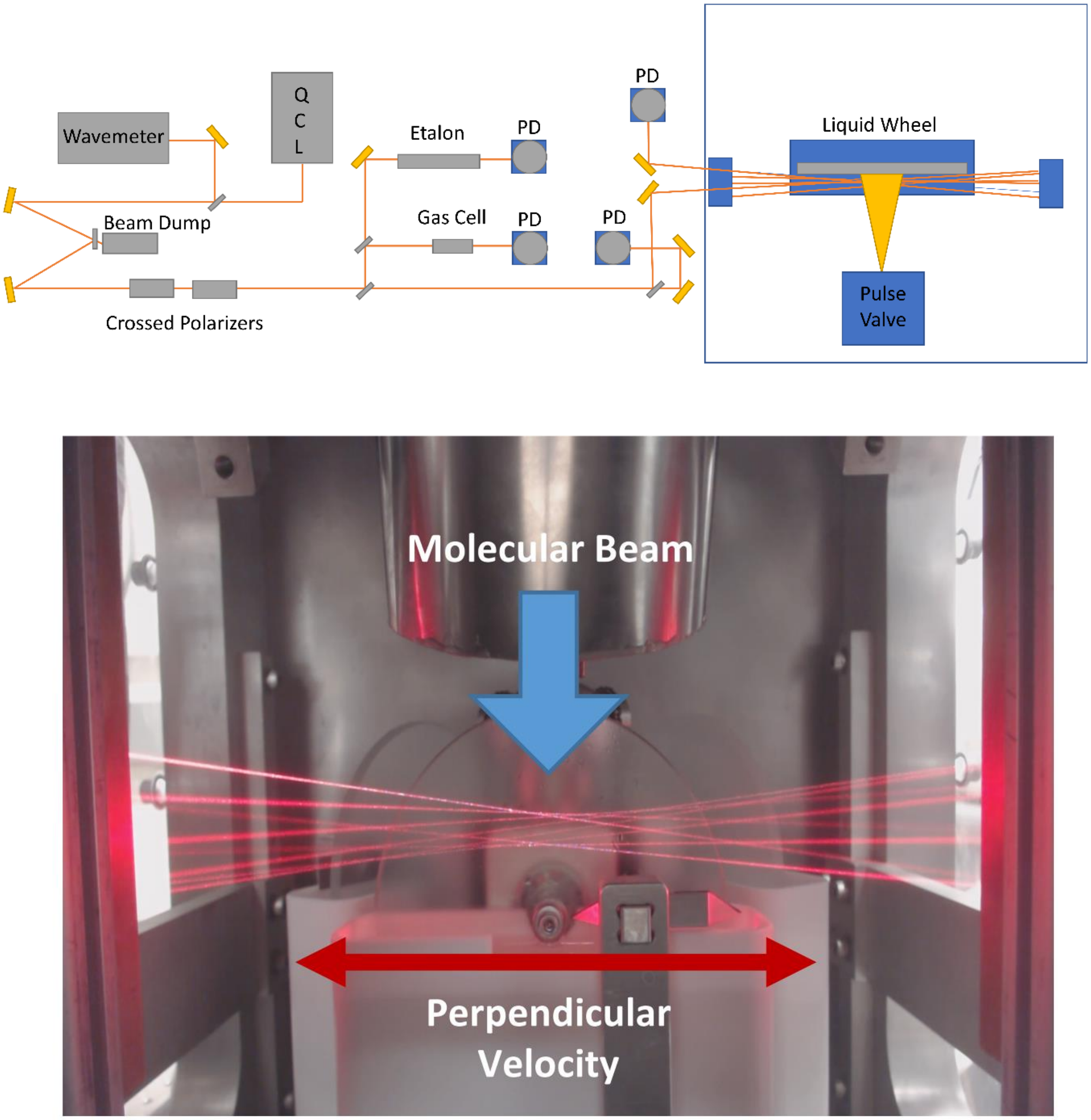

Figure 2.3 a) A schematic layout of the optics table used for these experiments. PD = Infrared Photodiodes b) An image of the internals of the vacuum chamber. Traced out in red is the path of the Harriot cell light.

used in lab, gives a frequency measurement several times a second, allowing for real time diagnostics of the laser frequency. During a scan, signals from both a bowtie etalon and a gas cell are recorded. The dry air purged bowtie etalon has a finesse of ~20-30 and a FSR of 249.566(30) MHz. Thus, by interpolating between the etalon fringes, the relative tuning of the laser can be

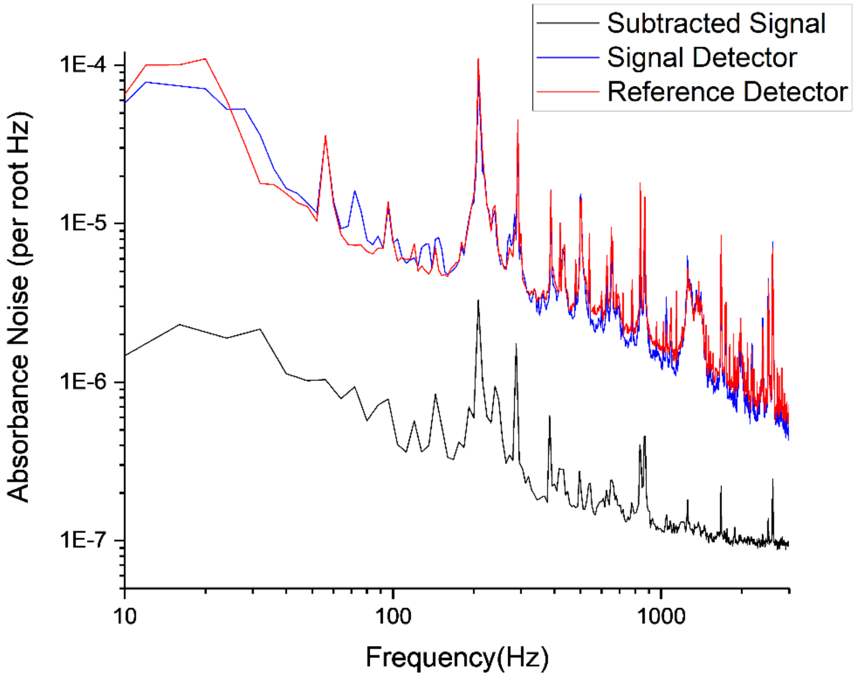

Figure 2.4 Absorbance noise spectral density. The reference detector signal is scaled to the signal detector signal and then they are subtracted from each other, removing common mode noise and leave us with the subtracted signal, whose noise has been reduced by 20-40 db depending on the frequency. The shot noise noise floor for these powers is ~1*10^{-7} per root Hz.

calculated. With an appropriate choice of reference gas (often the gas under study), the absolute frequencies of the measured reference lines can be used to calibrate the starting frequency of each scan. The scattering signal is measured in a shot-noise limited spectrometer. This is achieved via a balance detection scheme, with one of the two arms containing the scattering system in the vacuum chamber. The signal from the reference detector is scaled to DC value of the signal detector and then, the two channels are subtracted, leaving only the differential signal, which contained the absorbance from the scattered molecules. This setup achieves absorbance sensitivities of around 1.0*10^{-5} in the bandwidth of the experiment. An absorbance spectral noise density plot can be seen in Fig 2.4. Due to practical limitations on electronic, the reduction in common mode noise is between ~20-40 db.

2.3 Scattering Chamber

The 60 L square vacuum chamber contains the scattering system. This chamber is pumped by a liquid N_2 cooled 6-inch diffusion pump that maintains an operating pressure below $1*10^{-4}$ torr during full operation, which means the minimum mean free path is several times the length of the vacuum chamber. This prevents any collisions with background gasses while the scatterer molecules travel from the beam sources to the surface and then from the surface to the measurement region. The scattering system is made up of the molecular beam source, the scattering target and the multipass cell. Fig. 2.3b shows an image of the vacuum system with the path of the infrared light traced out by a HeNe laser. Our beam source is of Proch and Trickl design[5]. The molecular beams used in this thesis were prepared generally as directed in the Perkins thesis[1]. CO and OCS behave much like CO_2 in a supersonic expansion. However, DCl is a much “stickier” molecule and thus, special effort must be made to prevent clustering. Since the flux of the beam sources is proportional to the source pressure and the area of the orifice and the collisional rate (~”clustering” rate) is proportional to the square of the source pressure and the diameter of the orifice, one should use a large diameter orifice with a low source pressure to minimize the total clustering of the molecular beam. The molecule’s rovibrational populations are characterized by measuring the incident beam 1-2 cm downstream from the molecular beam skimmer and the incident beam energy is measure using a time of flight microphone setup that is described in detail elsewhere.[6] The scattered signal is measured in a 16 pass concentric Herriot cell highlighted in Fig. 2.3b. The single pass cell length is ~40 cm. This beam path lies parallel to the plane of liquid surface and perpendicular to the molecular beam. This means that the Doppler broadening reports on the velocity perpendicular to the scattering plane defined by the liquid surface normal and the molecular beam.

2.4 Liquids of study

This thesis involve three different classes of liquids that sample different scattering dynamical regimes: 1) perfluorinated polyether, (PFPE, Krytox 1506, $F\text{-}[CF(CF_3)CF_2O)]_{14(avg)}\text{-}CF_2CF_3$), as prototype for a rough but chemically inert liquid surface, 2) squalane (2,6,10,15,19,23-hexamethyltetracosane, $C_{30}H_{62}$), as prototype for strongly hydrophobic surface, and 3) glycerol (1,2,3-propanetriol, $C_3H_8O_3$), as prototype for a highly hydrophilic surface due to multiple protruding OH groups. Each liquid is degassed under ~1 mTorr vacuum at room temperature for several hours to remove dissolved atmospheric gases, or at slightly elevated temperatures (~ 350 K) for the glycerol liquid samples to allow for more complete degassing within a reasonable time frame.

2.5 Thermal control of liquid surface

For the studies that involve different surface temperatures, a temperature regulation system was added. In the studies of DCl in chapter 3, the copper liquid trough was directly cooled by a cold plate connected to a recirculating ethanol chiller. This allowed for temperature stabilization between -20C to 40C. For the studies of CO in chapter 4, efforts were put forth to reduce thermal gradients and increase temperature stability and accuracy. The liquid trough was better thermally isolated with Teflon spacers and the glass wheel was replaced with a bead blasted steel wheel. Since the thermal conductivity of the metal parts is much larger than the Teflon spacers, the liquid + metal system will be held a constant temperature. Temperature stabilization was achieved by adding a thermoelectric cooler (TEC) between the cold plate of the ethanol chiller. This TEC was controlled by a Thorlabs QCL controller (ITC4002QCL) with an integrated TEC controller. It stabilized the temperature to a thermistor (RC44008) epoxied to the front of the copper trough. Accounting for the thermistor’s accuracy and the systematic errors introduced through the TEC controller, the combined systematic and probabilistic errors in the temperature stabilization give an absolute error of under .5 kelvin over the entire operating range of the thermal system. This system as also used for the temperature dependent work on OCS in chapter 5 and 6.

2.6 LN_2 trap

For the work in chapter 5 and 6, a LN_2 cooled cold plate was added at the top of the vacuum chamber and achieves a temperature of 90 K when cooled. This was implemented to reduce the background OCS in the vacuum chamber. Since the FWHM of a room temperature OCS transition is ~100 MHz and the laser’s linewidth is ~10 MHz, there is no appreciable frequency noise from the scattered signal. However, since the frequency noise on the background gas in the chamber is not common mode on both the signal and reference detectors, it passes straight through the common mode subtraction circuit and appears as extra noise. This noise is reduced by the cryopumping by a factor of ~10-100, due to an equivalent reduction of background OCS.

Chapter 2 References

1. Perkins, B. G., Jr. Quantum State-Resolved Energy Transfer Dynamics at the Gas -Liquid Interface. Ph.D., University of Colorado at Boulder, Boulder, 2009.
2. Gisler, A. W.; Nesbitt, D. J., On Probing Ions at the Gas-Liquid Interface by Quantum State-Resolved Molecular Beam Scattering: The Curious Incident of the Cation in the Night Time. *Faraday Discuss.* **2012**, *157*, 297-305.
3. Curl, R. F.; Capasso, F.; Gmachl, C.; Kosterev, A. A.; McManus, B.; Lewicki, R.; Pusharsky, M.; Wysocki, G.; Tittel, F. K., Quantum Cascade Lasers in Chemical Physics. *Chem. Phys. Lett.* **2010**, *487*, 1-18.
4. Weida, M. J.; Caffey, D.; Rowlette, J. A.; Arnone, D. F.; Day, T., Utilizing Broad Gain Bandwidth in Quantum Cascade Devices. *Opt. Eng.* **2010**, *49*.
5. Proch, D.; Trickl, T., A High-Intensity Multi-Purpose Piezoelectric Pulsed Molecular-Beam Source. *Rev. Sci. Instrum.* **1989**, *60*, 713-716.
6. Nizkorodov, S. A.; Harper, W. W.; Chapman, W. B.; Blackmon, B. W.; Nesbitt, D. J., Energy-Dependent Cross Sections and Nonadiabatic Reaction Dynamics in F($^2P_{3/2}$), $^2P_{1/2}$)+n-H_2 -> HF(V,J)+H. *J. Chem. Phys.* **1999**, *111*, 8404-8416.

Chapter 3

Quantum State and Doppler Resolved Scattering of Thermal/Hyperthermal DCl at the Gas-Liquid Interface: Support for a Simple “Lever Arm” Model of the Energy Transfer Dynamics*

3.1 Introduction

The dynamics of collisions at the gas liquid interface are essential to many aspects of atmospheric and environmental chemistry.[1] Interfaces play a particularly crucial role in heterogeneous chemistry, often providing reagents with lower barrier pathways toward chemical reactions that might be kinetically unfavorable in the gas phase.[2-3] The interaction of gas molecules with aerosol droplets is of special importance to atmospheric chemistry;[4] one example of key impact being the depletion of ozone in the upper atmosphere catalyzed by chlorine atoms (Cl) and chlorine generated hydrocarbon radicals.[5-6] For example, it has been shown that an important pathway to generating highly active Cl radicals is oxidation of hydrogen chloride by N_2O_5 on water droplets, for which the reagents HCl and N_2O_5 must first physisorb and thermally accommodate on the gas-liquid interface. As a result, an understanding of energy transfer dynamics in molecular collisions with liquid surfaces rises to considerable significance.

One direction in which the atmospheric community has made considerable progress is in measuring the temperature dependent *equilibrium* properties at the gas-liquid interface, for which both enthalpy and entropy of solvation can be extracted from gas-droplet absorption measurements. For example, from ~100 μm water droplets moving through a low-pressure gas, Davidovits and coworkers have been able to measure uptake of gas molecules into the liquid as a function of interaction time and droplet temperature.[7-8] In experiments with hydrogen chloride

---

*Published in J Phys. Chem. C, 123, 3449, (2019) on water droplets, for example, it has been proposed that the rate-limiting step to solvation is physical adsorption of HCl onto the liquid surface. Despite the considerable power of these droplet-train techniques, the uptake processes are detected by total loss of reagent HCl and cannot be easily decoupled into more fundamental reaction steps. One critical limitation of the above methods is that they sample an equilibrium state and therefore do not provide *kinetic* information on molecular interactions with gas liquid interface.

An alternative approach to probing such kinetics at the gas liquid interface is by scattering a cold, monoenergetic molecular beam from a surface of interest and measuring the resulting fluxes under low pressure, collision free conditions. This allows for the extraction of more dynamical information about both i) the gas-liquid interfacial properties and ii) the molecule-specific interactions with the surface. By way of example, previous studies by several groups using molecular beam scattering have revealed compelling evidence for microscopic branching into two dynamical scattering pathways.[9-16] Specifically, incident molecules can either i) collide with the surface and thermally accommodate through a sequence of collisional interactions, trapping on the surface, and then undergoing a final desorption step (trapping-desorption (TD)) or ii) impulsively scatter (IS) into an energized rotational/translational state distribution through one or a few collisional interactions with the interface (see Fig. 3.1). On the one hand, earlier quantum state resolved studies with CO_2 reported that both rotationally and translationally scattered molecules from the thermal desorption (TD) pathway emerged in a Boltzmann-like distribution characteristic of the surface temperature (T_S).[17] On the other hand, it was also noted, in NO gas-liquid scattering studies, that this same fully accommodated TD pathway resulted in asymptotic rotational and electronic temperatures that were out of equilibrium with and *cooler* than the surface.[18-21] By detailed balance, it was suggested that NO

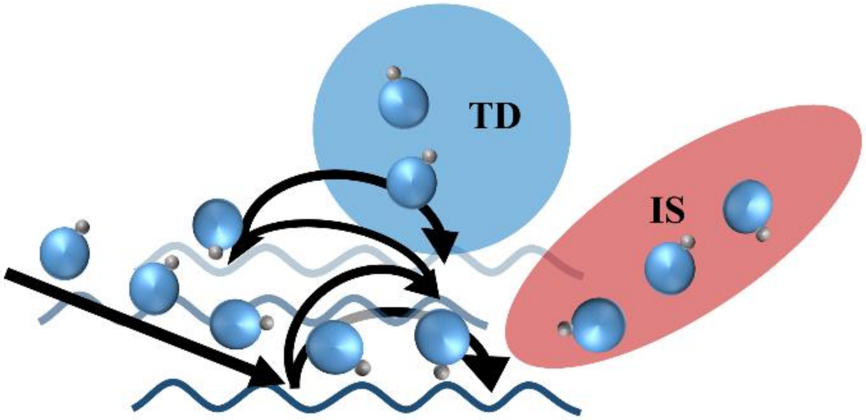

Figure 3.1: Cartoon depiction of the dominant DCl scattering pathways: Microscopic branching between i) trapping desorption (TD) processes, based on multiple collisions with the interface and leading to complete thermalization, vs. ii) impulsive scattering (IS) processes, which involve only a relatively few collisions with the surface and thereby allowing for scattering into much hotter internal (rovibrational) and external (translational) channels.

might experience rotational and/or electronic state dependent dynamical barriers while leaving the surface, asymptotically causing the flux to fall out of equilibrium with T_S.

By way of contrast, the impulsive scattering (IS) pathway is not required to lose memory of its original collision dynamics and, as a result, often results in flux distributions forward peaked in the scattering plane.[16, 22] In CO_2, the Doppler velocity distributions perpendicular to the scattering plane were also effectively described as a Maxwell Boltzmann temperature distribution[23] and in equilibrium with the rotational distributions. Most relevantly, rotational distributions in the IS component of such scattered NO and CO_2 have been routinely found to be well described by a "temperature" ($T_{IS(rot)} >> T_S$),[17-26] despite the lack of any dynamical picture for "equilibration" within the IS quantum state manifolds.

Pioneering studies on DCl scattering at the gas-glycerol interface have been performed with time of flight methods by the Nathanson group.[27-37] As noted in previous gas-liquid interfacial studies, their methods again reveal two distinct scattering pathways, one achieving complete thermalization with the surface (TD) and the other scattering impulsively (IS) with an average energy content often much higher than the surface thermal energy (kT_S). Furthermore, Nathanson's powerful combination of mass spectroscopy and time of flight methods revealed that proton exchange between DCl → HCl at the surface of liquid glycerol requires trapping and thermalization of the incident DCl.[27-28, 30, 34] Indeed, as one plausible model, it was proposed that these DCl molecules must first dissociate into the liquid and recombine with other solvated ions (such as H_3O^+ or OH^-) in the glycerol. The present work nicely complements these studies, in which we focus on quantum state resolved scattering dynamics of DCl at the gas-liquid interface, using direct infrared laser absorption and high resolution (< 10 MHz) laser Dopplerimetry methods to probe the internal rotational and out-of-plane translational velocity distributions in the scattered molecules.

The chapter is organized as follows. In Sec. 3.2, we briefly summarize the quantum state resolved experimental techniques. This is followed in Sec. 3.3 by presenting results from thermal (E_{inc} = 1.5(1) kcal/mol) and hyperthermal (E_{inc} = 11.5(5) kcal/mol) DCl scattering studies from a series of prototypical liquids, which successfully explore both TD and IS components in the energy transfer collision dynamics. These rotational distributions are then analyzed in Sec. 3.4, appealing to the simple but physically motivated "lever arm" models of McCaffery and coworkers[38-43] (e.g., angular momentum transfer via hard sphere scattering from the liquid surface) to help interpret the observed trends. One unexpected success is the combination of these "lever arm" scattering models with capillary wave theory[44] to provide a first analytical framework for rationalizing the Boltzmann temperature-like behavior observed empirically in present and previous studies.[17-26] The chapter concludes with summarizing comments and directions for future experiments in Sec. 3.5.

3.2 Experimental/Methods

A detailed overview of the experimental apparatus has been given elsewhere, thus only essential details and modifications[17, 24, 45] specific to the present work need to be considered. A schematic diagram of the scattering chamber is shown in Fig. 3.2. The instrument consists of a supersonic molecular beam, a freshly cleaned liquid surface and a near quantum shot noise limited infrared laser direct absorption spectrometer. To help deconstruct contributions from trapping desorption (TD) and impulsive scattering (IS) pathways, both thermal and hyperthermal

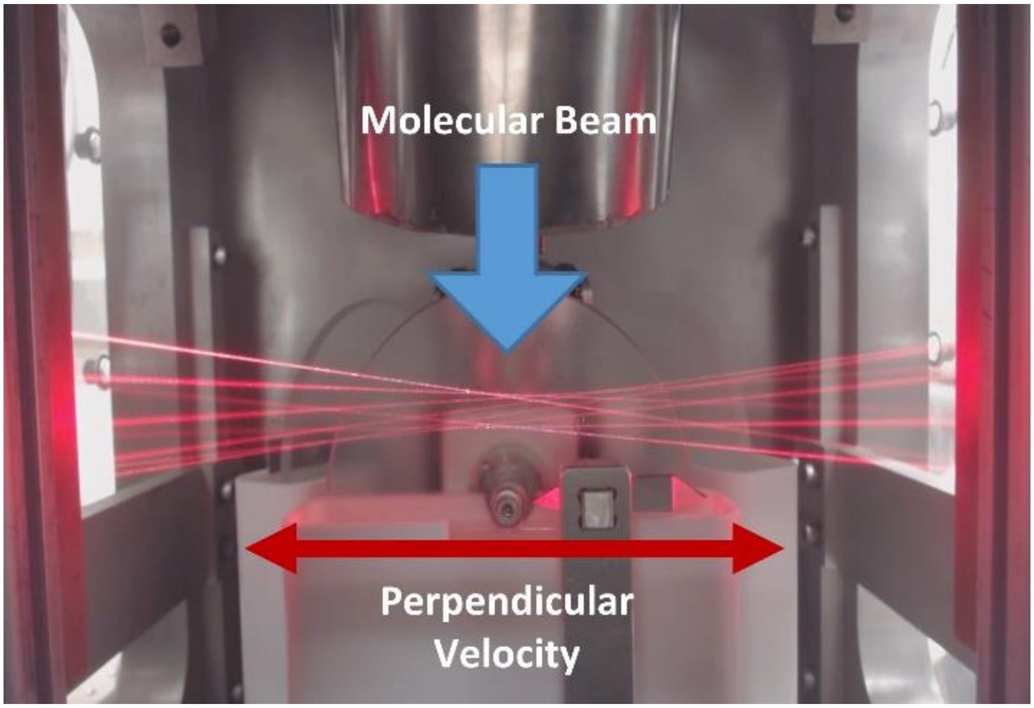

Figure 3.2. Gas-liquid scattering chamber with a skimmed molecular beam impinging on a Fenn-type rotating wheel assembly. Also shown is a visualization of the infrared multipass Herriott cell geometry for quantum state and high resolution Doppler resolved detection of the scattered DCl (v,J,$v_\perp$) molecular density.

molecular beams are explored. The thermal molecular beam is generated from a 10% DCl/Ar mixture supersonically expanded through a piezoelectric 300 μm pinhole valve with a pulse length of 400 μsec and collimated with a 3 mm skimmer situated 1.5 cm from the nozzle orifice. The hyperthermal molecular beam is generated by reverse seeding DCl in a 6.7% mixture with H_2, expanded through a slightly larger 500 μm pinhole nozzle but with the same 400 μsec pulse length and skimmer geometry. The translationally thermal and hyperthermal beams have energies of 1.5(1) kcal per mol and 11.5(5) kcal per mol, respectively, as measured with a fast *in vacuo* hearing aid microphone/time of flight setup.[46] Both molecular beams are rotationally cold (T_{rot} = 9.5(1) K), which translates into more than 75% of the DCl population in the J = 0 or 1 rotational state. The thermal and hyperthermal studies have been performed at incident angles of 45° (5) and 65° (8), respectively, with scattered DCl species detected in the corresponding near specular angular direction. Due to the geometry of the scattering chamber, the 45° beam collects scattered signal from -25° to 70° and the 65° beam collects signal -40° to 75°. However, both of these beam collection efficiencies are peaked around 60°-70°. The hyperthermal energy scattering results exhibit negligible contamination from DCl (J = 0, 1) in the incident beam, due to the more glancing scattering geometry and therefore a greater degree of angular/spatial separation in the scattered flux.

The liquid surface is prepared in the method of Lednovich and Fenn,[47] using a rotating (ω ≈ 0.2 Hz) frosted glass wheel (12.7 cm diameter) half-submerged in the liquid reservoir and scrapped with a stationary razor blade to present a clean, thin (≈ 500 μm) gas-liquid surface to the impinging molecular beam. These studies have examined three prototypical liquids to sample three broad classes of gas-liquid scattering dynamics (see Table 1): 1) Perfluorinated polyether, (PFPE, Krytox 1506, $F\text{-}[CF(CF_3)CF_2O)]_{14(avg)}\text{-}CF_2CF_3$) as a chemically inert liquid dominated by CF functional groups, thus imparting the interface with partially negatively charged F atoms and a strongly dipolar character, 2) Squalane (2,6,10,15,19,23-hexamethyltetracosane, $C_{30}H_{62}$) as a prototypical hydrophobic hydrocarbon with predominantly CH surface groups and thus only a weakly positive dipolar interfacial character, and 3) Glycerol (1,2,3-propanetriol, $C_3H_8O_3$) as a small hydrophilic hydrocarbon chain, with multiple OH groups giving it a mixed positive and negative dipolar character depending on bond orientation at the gas-liquid interface. Each liquid is degassed under ~1 mtorr vacuum at room temperature for several hours to remove dissolved gases (H_2O, O_2, N_2, CO_2), with elevated temperatures for the glycerol liquid samples to allow for complete degassing within a reasonable time frame.

Table 3.1: Liquid properties

	PFPE	*Squalane*	*Glycerol*
Surface Tension (dyne/cm)	17	30	63
Density (g/cc)	1.87	0.81	1.26
Molar Mass (amu)	2400	422	92
Molecular Size (nm)	1.29	0.95	0.49
Vapor Pressure (Torr, 25 Celsius)	7×10^{-7}	2×10^{-8}	1.7×10^{-4}
Surface Groups	CF_2 and CF_3	CH_2 and CH_3	Bonded OH, CH_2
*Estimated Surface Roughness (Å)**	8.0	6.2	4.4

*Root mean square (rms) width of the surface region (δ) is approximately $[(kT_{liq}/2\pi\gamma)\times \ln(2\pi L_c/d)]^{1/2}$ where γ is the surface tension, $L_c = [\gamma/(g\,\rho)]^{1/2}$ and d is simple density based estimate of the molecular size ((molecular mass/density)$^{1/3}$).

During pulsed valve operation (11 Hz repetition rate), the chamber is maintained at $< 1 \times 10^{-4}$ Torr with a liquid N_2 cooled 6" diffusion pump, even for relatively high vapor pressure liquids such as glycerol. This translates into mean free path conditions ($\lambda \approx 100$ cm) comfortably longer than the chamber dimensions and guarantees that nascently scattered DCl (v = 0, J) can travel collision free from the surface to the laser probe region. For the hyperthermal collision energy studies, the liquids reside in one of three Teflon reservoirs mounted on a rotating plate, providing convenient interchangeable access to the molecular beam *in vacuo* with only a nominal time delay. For the temperature-dependent studies, the liquids are housed in a copper reservoir in contact with an aluminum block, whose temperature is controlled by a circulating ethanol flow. Temperatures can be varied from -20 to 40 Celsius, with the lower and upper values constrained by the liquid melting points and excessive vapor pressure in the chamber, respectively.

The scattered DCl number densities are measured via high resolution Beers law absorption spectroscopy, with light generated by an external cavity quantum cascade laser [48-50] (ECQCL, Daylight Solutions MHF-QCL, 4.6 um laser chip) directed through a 16 pass Herriot cell parallel to the wetted wheel surface. Light intensities are measured differentially before and after the Herriot cell on liquid N_2 cooled Indium Antimony (InSb) photodetectors in a fast servo loop subtraction circuit to yield high bandwidth (60 MHz) rejection of common mode laser noise. The resulting absorbance spectral sensitivities (2-3x10^{-7} per $Hz^{1/2}$ for 10 μW on each detector) are within a factor of two of the fundamental quantum shot noise limit.

The infrared laser is scanned across each Doppler broadened transition in 2 MHz steps, with signals integrated over the rising edge (300 μsec) for every gas pulse (11 Hz rep rate) to eliminate collisionally relaxed DCl molecules recrossing the laser multipass region. The infrared laser is calibrated by combination of a low pressure (< 1 Torr) DCl reference gas cell for absolute frequencies and 249.566(33) MHz fringe spacings from a Fabry-Perot cavity to facilitate precision least squares fits to the Doppler profiles. The laser tunes from R(0) (2101.63

cm^{-1}) through R(18) (2249.49 cm^{-1}) in DCl, which, for a rotational constant of $B_{DCl} \approx 5.4$ cm^{-1}, provides access to lower states from $E_{rot} = 0$ up to 1800 cm^{-1}. The frequency noise of the ECQCL is < 10 MHz FWHM over a single scan, which is 10-20 fold narrower than typical scattered Doppler velocity contributions of 140 MHz. The laser polarization is normal to the liquid surface. The use of a few mW and frequency stable quantum cascade lasers allows for a dramatically reduced absorbance noise floor as well as a decrease in frequency noise compared to our previous Pb-Salt diode laser capabilities operating with only a few μW power levels. This has greatly expanded the flexibility of our experimental apparatus and allows gas-liquid scattering dynamics with much weaker oscillator strength projectiles such as DCl ($S_0 = 16.4$ km/mol, compared to CO_2 with $S_0= 665$ km/mol) to be studied with quantum state resolved, direct absorption laser methods.[51-52]

3.3 Results and Analysis

3.3.1 Low energy DCl scattering yields fully TD distributions in equilibrium with the liquid

The natural metric to consider in a pulsed scattering experiment is the scattered flux (F, #/cm^2/s), since particle number is rigorously conserved among all possible scattering pathways. However, high resolution direct absorption methods measure column integrated density (#/cm^2), arising from integration of the number density (N(l)) along the laser path and equivalent to the flux of molecules passing through the probe laser divided by the transit time velocity. This yields a differential absorbance

$$dA = S_{J',v',J,v}\ N(l)\, dl = S_{J',v',J,v}\, F(l) * \left(\frac{t_{transit}}{d_{transit}}\right) dl = S_{J',v',J,v} \left\langle\frac{F(v_{transit},l)}{v_{transit}}\right\rangle dl \qquad \text{Eq. 1}$$

where $S_{J',v',J,v}$ is the rovibrational line strength and can be calculated from the integrated cross section, the Hönl-London factors and Herman-Wallis rovibrational coupling terms.[52] The angle brackets imply an averaging over the transit time velocities ($v_{transit}$). For the present geometry (laser perpendicular to the scattering plane), Eq. (1) integrates to yield:

$$\frac{A(j,v,\mathrm{v}\perp)}{S_{J',v',J,v}} = \langle\frac{F(v_{transit})}{v_{transit}}\rangle * l_{effective}$$

$$\approx \langle\frac{F_{total}*P(v_{transit})}{v_{transit}}\rangle * l_{effective} * P(j,v,v_{\perp}) = N * P(j,v,v_{\perp}) \qquad \text{Eq. 2}$$

Since the laser linewidth is much narrower than Doppler shifts for the scattered DCl, the absorption is directly proportional to the quantum state probabilities P(j,v) times the Doppler distribution along the probe laser beam ($\mathrm{v}_{\perp}$). The flux distribution can approximately be separated into the transit velocity scattering distribution and the scattering distribution of the rest of the resolved parameters and thus the unresolved factors can be collapsed into a single

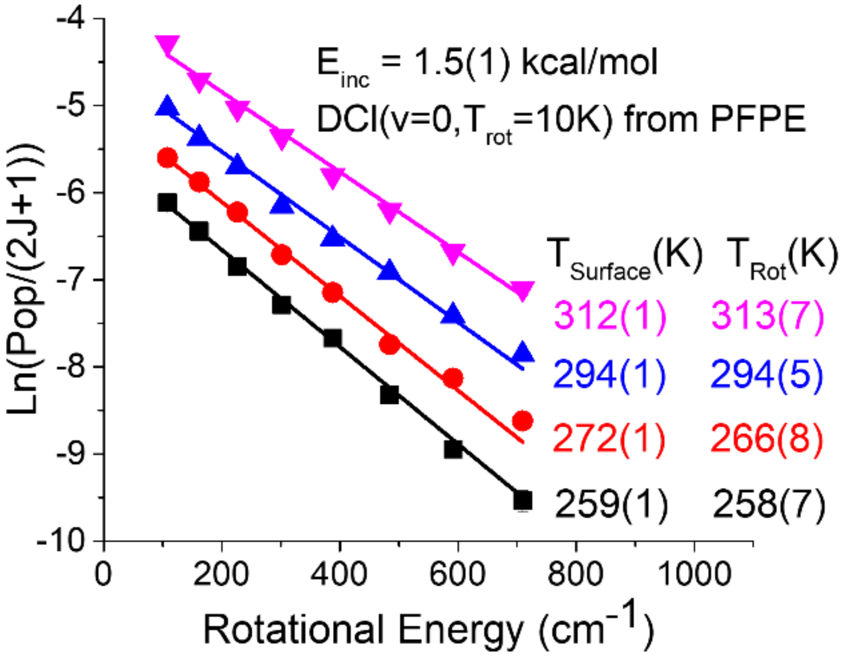

Figure 3.3: Sample Boltzmann plots (E_{inc} = 1.5(1) kcal/mol) for scattering of DCl from the gas-perfluoropolyether (PFPE) interface as a function of surface temperature. Note that good agreement between T_S and T_{rot}, consistent with fully equilibrated TD dynamics at low incident energies.

normalization factor (N). The validity of this approximation is discussed elsewhere, but when used in the context of a two temperature model, this separation is found to slightly overpredict the branching ratio into the TD component but accurately capture the TD and IS rotational temperatures.[22]

Time of flight mass spectroscopy studies by Nathanson and coworkers[27-30] suggest that the trapping desorption (TD) fraction of the scattered molecules completely thermalize, lose all memory of the incident collision dynamics, and eventually desorb *in equilibrium* with the surface temperature, T_S. Though explicitly confirmed in quantum state resolved studies in our group[26, 53] for CO_2 ($B_{CO2} \approx 0.40$ cm^{-1}) with respect to rotational, vibrational and translational degrees of freedom, the expected behavior for a light hydride such as DCl ($B_{DCl} \approx 5.45$ cm^{-1}) is perhaps less obvious. By way of due diligence, therefore, we have performed a series of DCl scattering studies at thermal collision energies as a function of the liquid surface temperature T_S. Fig. 3.3 displays sample Boltzmann plots (ln [Pop/(2J+1)] vs. E_{rot}) for DCl populations scattered from PFPE at low collision energies ($E_{inc} \approx 1.5(1)$ Kcal/mol), for which single temperature fits to the data recapitulate the surface temperatures (T_S) to within measurement uncertainty. A confounding effect that must be acknowledged is the possibility of non-isotropic m_J distributions.

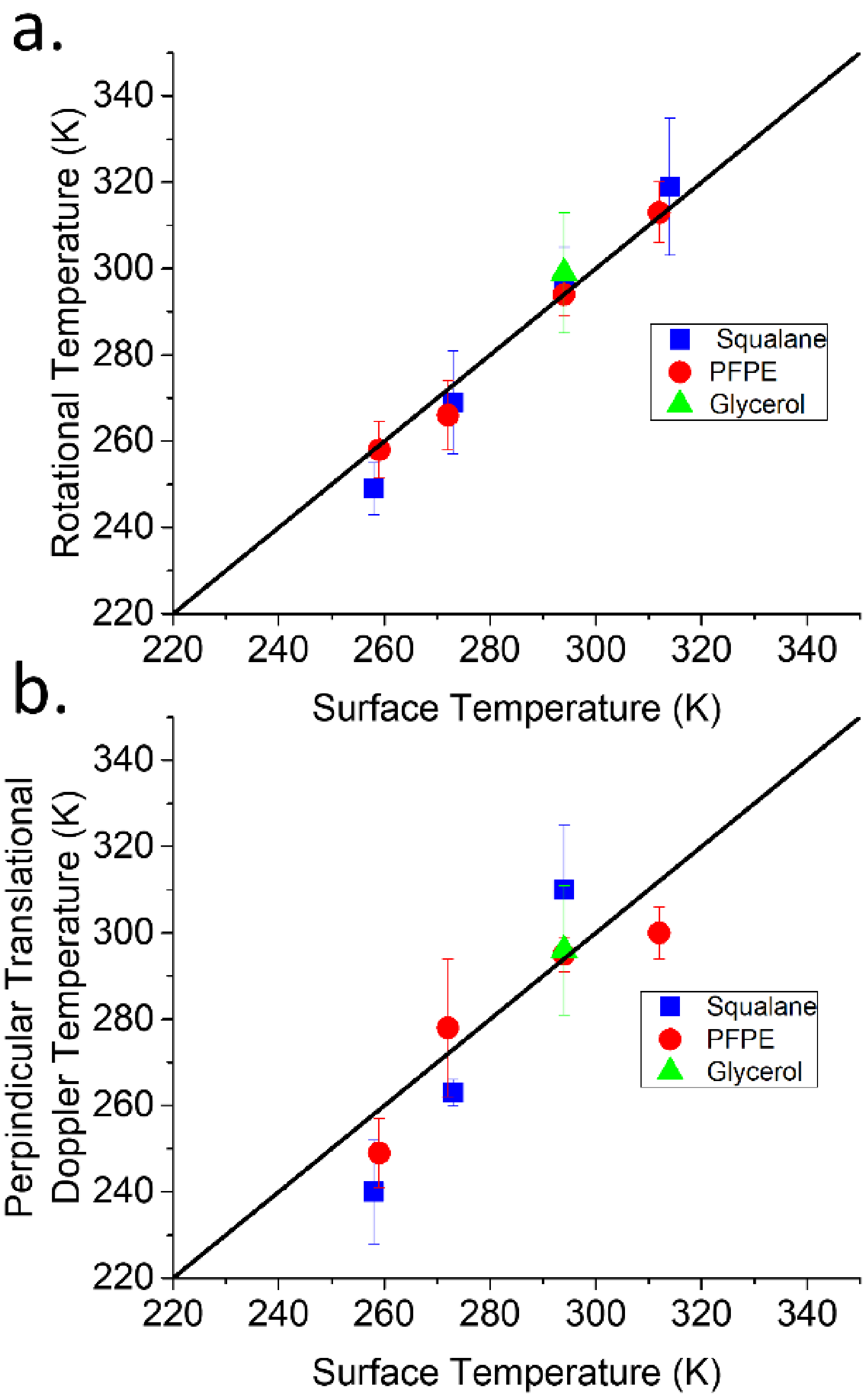

Figure 3.4. Summary of low energy (E_{inc} = 1.5(1) kcal/mol) scattering as a function of surface temperature (T_S) for three different liquids. (a) The upper panel displays the dependence of the DCl rotational temperature on T_S, with (b) the lower panel highlighting the dependence of the perpendicular Doppler distributions on surface temperature. Both plots are in agreement with a simple $T \approx T_S$ prediction (solid line), which would imply full thermalization and equilibration of the scattered DCl with the surface prior to desorption.

The polarization of the laser and the geometry of the detection system used leads to a correction of the absorption strength that is proportional to $<J_y>$, which is the degree of forwards or backwards end over end tumbling of the scattered molecule. The size of the effect has been measured at high collision energies (10.6 kcal per mol) for CO_2 and it has been seen to be on the order of about 2.5% decrease in the strength of the absorption at ~ 1000 cm^{-1} rotational energy with decreasing magnitude as the rotational energy decreases.[54] At rotational energies where the TD scattering dominates, the effect is weak enough to be considered zero with the detection sensitivities determined by shot noise. In this current experiment at low collision energies, we expect the effect to be much smaller than the error bars on the data being presented thus it can be entirely ignored for this analysis. Fig. 3.4a presents a summary of results for all the liquid temperatures explored for each of the three different liquids. By microscopic reversibility and detailed balance considerations, this has clear implications.[55-59] Specifically, this requires that over a range of collision energies consistent with T_S, DCl must exhibit unity sticking probability independent of initial rotational quantum state. In other words, DCl at near thermal energies must undergo *purely trapping desorption* (TD) dynamics on each of the three gas-liquid interfaces in a J-independent fashion.

We can test this further by also probing the Doppler velocity components along the laser probe direction, for which a Gaussian velocity distribution can be used as a physically motivated model for the transverse DCl velocities desorbing from the surface. Fig. 3.4b summarizes the corresponding Doppler velocity based temperature (T_{Dopp}) as a function of T_S. Consistent with the above expectations, the TD component sampled via low collision energy scattering thermalizes for all three test liquids in both rotational and transverse translational degrees of freedom, yielding $T_{Dopp} \approx T_{rot} \approx T_S$ over an appreciable range of liquid temperatures. Although our current detection geometry does not permit us to sample translational distributions in the scattering plane, time of flight studies by the Nathanson group directly probe the velocities in the scattering plane and they see the signatures of DCl thermalizing with the surface.[27] Along with the data measured in this chapter, this leads us to conclude that DCl truly does thermalize with the surface in both the translational and rotational degrees of freedom at low collision energies.

3.3.2 IS scattering model

The fully *equilibrated* behavior observed in Sec 3.3.1 for near thermal ($E_{inc} \approx 1.5(1)$ kcal/mol) scattering provides the necessary backdrop for both distinguishing and analyzing contributions from the *non-equilibrium* IS component of the collision dynamics under hyperthermal ($E_{inc} \approx 11.5(5)$ kcal/mol) conditions. To establish a context, it has been routinely noted in previous quantum state resolved studies with CO_2 and NO scattering from similar liquids that the IS component of the flux scatters into rotational and translational distributions characteristically much *hotter* than the surface temperature, yet modeled surprisingly well by a hot Boltzmann distribution in internal rotation and velocity components perpendicular to the scattering plane.[17-18, 25-26] However, it is important to stress the absence of any *a priori* dynamical basis for why the IS component should emerge in a hyperthermal yet temperature-like distribution. This is particularly so, as the IS angular distributions *in the scattering plane* observed in TOF studies by Nathanson, Minton, and others[15, 39, 60] are strongly anisotropic, with a clear propensity for a broadened but “lobular” forward scattering into more nearly specular directions. Indeed, the fact that i) rotational quantum state and ii) transverse velocity distributions in the IS channel can be so well characterized by a “temperature” should be recognized as an entirely unexpected and fundamentally surprising result. Indeed, upon closer inspection with improved experimental tools, analysis techniques, and signal-to-noise, one should expect this simple "dual temperature" microscopic branching picture into thermalized TD and IS channels to fail. As illustrated herein (*vide infra*), DCl scattering from these three test liquids provides first indications of the breakdown of such "two–temperature" models.

The experimental tool which most clearly highlights this breakdown is high resolution Dopplerimetry on the transverse velocity distributions for the scattered DCl. As the simplest model that incorporates non-equilibration dynamics in the DCl IS distributions, we allow the transverse velocity Doppler profiles to be characterized by a different temperature ($T_{IS,trans}$) than for end-over-end rotation ($T_{IS,rot}$). Such a model predicts the Doppler absorption profiles to be described by:

$$\frac{A(J,v_\perp)}{S_{J',v',J,v}} \propto \left\{\alpha\, P_{rot}(J,T_{TD}) P_{trans}(v_\perp,T_{TD}) + (1-\alpha) P_{rot}\left(J,T_{IS,rot}\right) P_{trans}\left(v_\perp,T_{IS,trans}\right)\right\} \quad \text{Eq. 3}$$

where $P_{rot}(J,T_{TD})$, $P_{rot}(J,T_{IS,\,rot})$ and $P_{trans}(v_\perp,T_{IS,trans})$ are the rotational (TD, IS) and transverse velocity (IS) distributions, respectively. If we fix T_{TD} at the surface temperature (as consistent with the data in Fig. 3.4), Eq. 3 permits a global fit of the complete set of DCl(J) absorption profiles to i) the TD vs IS branching ratio (α), ii) the two IS temperatures ($T_{IS,trans}$, $T_{IS,rot}$), and iii) one overall normalization constant. The results of such a fit for a sample set of absorption profiles are illustrated in Figure 3.5, for which the model captures the data quite well. The central frequency region of the profiles is dominated by the TD channel, while the wings reflect the strongly Doppler shifted IS components in the scattered signal. This use of global fitting parameters for the full set of DCl ($v=1 \leftarrow 0$, $J' \leftarrow J''$) transitions greatly reduces parameter correlation and permits teasing apart the IS/TD pathways far more robustly than from the velocity integrated column integrated densities themselves. Indeed, the importance of such a

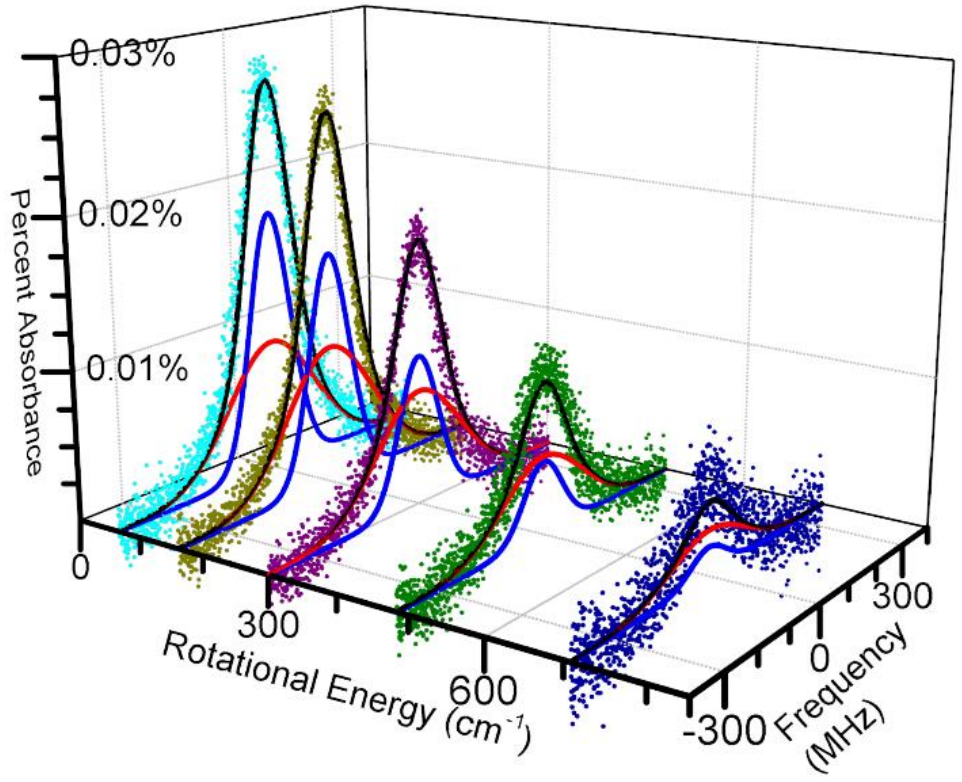

Figure 3.5: Doppler resolved data for sample DCl (v = 0, J) rotational states, providing support for a global fit to transverse Doppler (T_{Dopp}) and rotational ($T_{IS,rot}$) temperatures. The blue and red lines reflect the trapping-desorption (TD) component and the impulsively scattered (IS) components, respectively. See text for details.

approach can be most clearly appreciated in Fig. 3.6, which reveals the deconstruction of TD, IS and total rotational components in the fit as a function of J state. Specifically, the TD and IS subcomponents are quite similarly shaped (though, notably, with the fits always yielding $T_{IS} \geq T_{TD}$). This similarity adds in (destabilizing) linear dependence to the data, which makes it essential to also combine the transverse Doppler profile information in order to deconvolve the distributions stably and successfully.

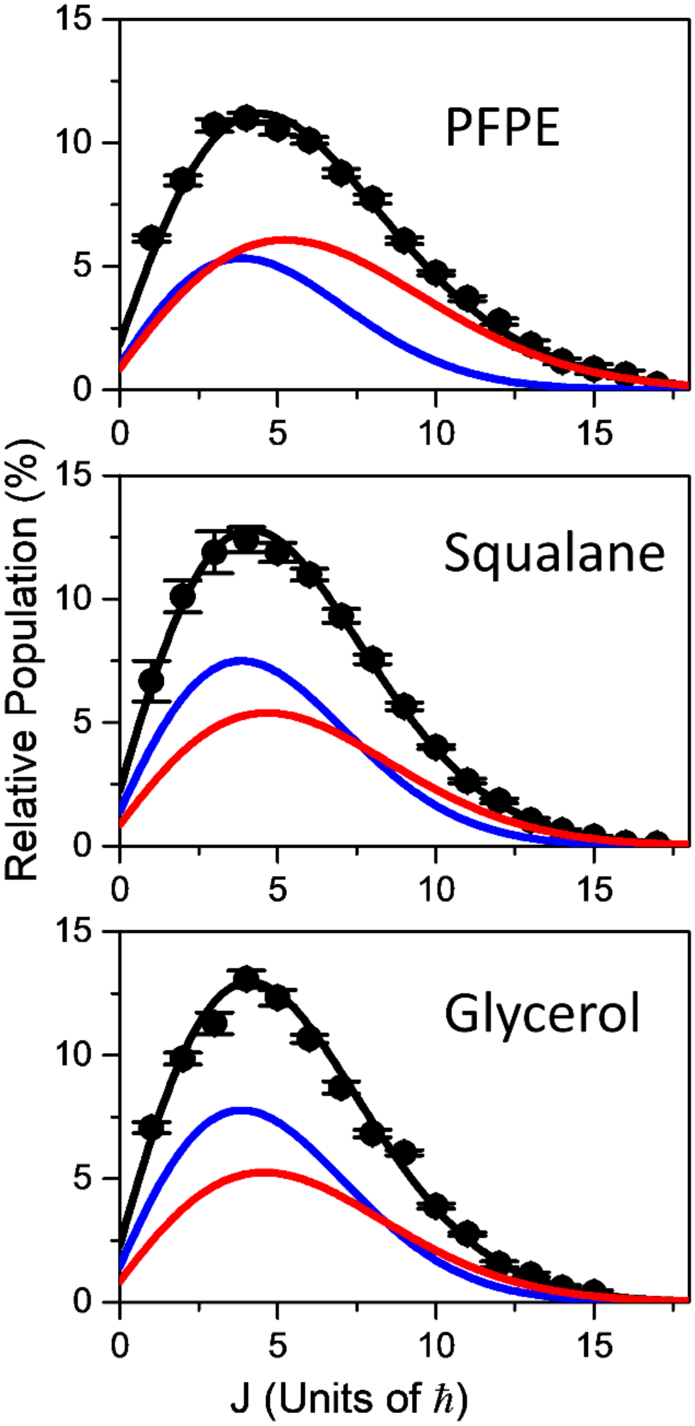

Figure 3.6: Scattered DCl(J) populations for the three different liquids at E_{inc} = 11.5(5)kcal/mol. (top panel: PFPE, middle panel: squalane and lower panel: glycerol. As in Fig. 5, the blue and red lines reflect the TD and IS components, respectively, from a least squares fit (see text for details).

3.3.3 IS Dynamics of DCl scattering at high E_{inc}

One surprising result immediately evident in the hyperthermal (11.5(5) kcal/mol) DCl scattering data is that the average rotational state *only* increases to J~5-6 from the average thermally populated state of J ≈ 4. This corresponds to a very modest (≈ 0.3 kcal/mol) increase in rotational energy, i.e., only a small fraction (3%) of the ~11 kcal/mol incident translational energy. This differs qualitatively from previous IS scattering studies for both CO_2 and NO projectiles, in which a substantial fraction (10-20%) of the incident translational energy is funneled into rotational degrees of freedom.[17-18, 25] Specifically, DCl undergoes far less efficient translational to rotational (T to R) energy transfer at the liquid surface, as further elucidated with a simple “lever arm” collision model in Sec 3.4. This weak rotational excitation of hydrides has been seen before in the scattering of OH done by McKendrick and coworkers.[13] In summary, with both the rotational populations *and* transverse Doppler distributions fit simultaneously, all the data can be robustly deconstructed into two well defined pathways, i) a thermally accommodated (TD) component emerging fully in equilibrium with T_S and ii) a *non-equilibrium*, hyperthermal DCl scattering distribution characterized by rotational temperatures (400 K) only slightly hotter than and yet translational temperatures (1000 K) very much hotter than the gas-liquid interface.

The data also reveal that the propensity to transfer incident hyperthermal energy differs dramatically for out-of-plane translational vs. rotational degrees of freedom. In contrast with an exceedingly modest excitation of DCl rotation, the liquid interface proves to be far more efficient at transferring the incident in-plane momentum into the out-of-plane component. These results are summarized in Fig. 3.7b, which displays the DCl rotational (T_{rot}) and transverse velocity (T_{Dopp}) temperatures observed for each of the three liquids. Specifically, the fitted temperatures

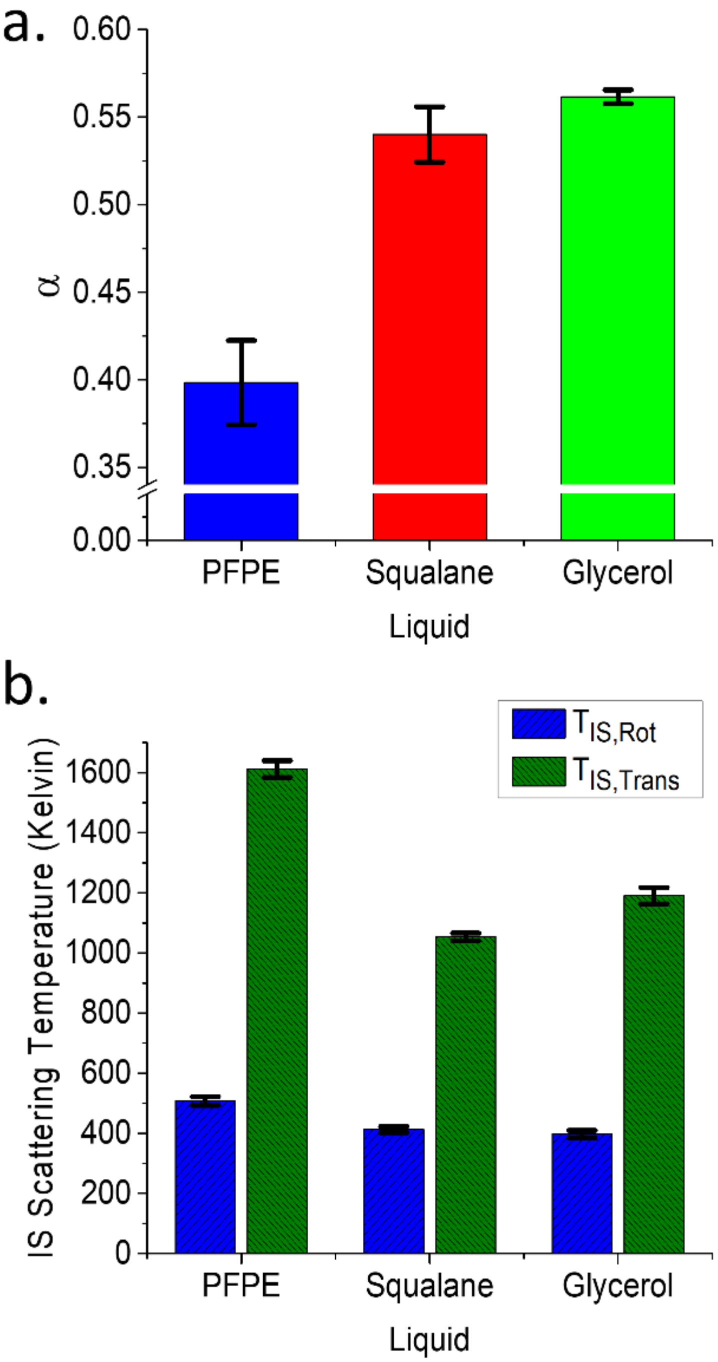

Figure 3.7: Summary of fit parameters for hyperthermal (E_{inc} = 11.5(5) kcal/mol) scattering conditions. (a) Top panel reflects the fractional trapping desorption coefficient ($\alpha = N_{TD}/(N_{IS} + N_{TD})$, where N is the total population in that channel. Lower panel displays the rotational (blue) and out-of-plane (green) temperatures from combined Boltzmann fits to the integrated absorption and high resolution Doppler profile data. Note the 3-4 fold differences between $T_{IS,trans}$, and $T_{IS,rot,}$ indicating a lack of equilibration between these degrees of freedom for the IS channel.

for (and thus collisional energy transfer into) translational degrees of freedom transverse to the scattering plane are 300%-400% larger than transferred into DCl rotation. Even for elastic scattering (not a good approximation), this would correspond to outgoing speeds requiring angular spreads of 25° RMS in the scattered flux to achieve the 250-300 MHz Doppler linewidths (FWHM) in the IS scattered component, with a correspondingly broader angular range if translational energy is lost to the surface.

Along with lower rotational excitation efficiencies, a larger fraction of DCl thermally accommodates on the surface than observed previously for CO_2 (see Table 3.2 and Fig. 3.7a). For DCl scattering from PFPE, 40% of the collisions can be attributed to a long-lived TD interaction with the liquid vs. only a 30% for CO_2.[25] Such an increase in the trapping fraction for DCl vs. CO_2 certainly can be partially attributed to the much deeper well depths at the gas-liquid interface for DCl. This is perhaps not surprising since DCl has a strong dipole moment μ = 1.080 D[61] vs. μ = 0 D for centrosymmetric CO_2, while having comparable polarizabilities and quadrupole moments.[61-62]

Table 3.2: Summary of least squares DCl scattering parameters

Liquid	*Alpha*	*T_{IS} Rotational (K)*	*T_{IS} Doppler (K)*
PFPE	0.398(24)	508(15)	1612(28)
Squalane	0.540(16)	412(10)	1054(13)
Glycerol	0.556(9)	397(13)	1191(27)

It might at first seem to be a simple task to use the trapping desorption ratios (α) from these fits as a metric for *absolute* branching between various scattering pathways. As noted previously, however, the multipass absorption geometry samples only the transverse velocity component from Dopplerimetry and thus is not able to extract relative fluxes (i.e. velocity-weighted densities) from the measured J-state distributions. This geometry also samples a broad distribution of scattering angles, which can confound the separation of the pathways in an absolute fashion thus making α useful for comparing trends among similar experimental setups. Additionally, DCl can undergo signal loss via i) proton exchange to form HCl or ii) temporary solvation into the bulk liquid, the latter of which would result in signal loss due to residence times in excess of the integration window. Interestingly, in work by Nathanson et al on H/D proton exchange of hydrogen halides at the glycerol surface, nearly all of the proton exchange signal was shown to result from a TD pathway, i.e. the H/D exchanged product species comes off with a Maxwell-Boltzmann velocity distribution at T_S.[27-28, 30-32] Thus, the lack of incorporation of such loss channels in our model translates into a lower limit for the measured fraction of molecules that thermalize with the surface. Finally, we note that one can circumvent these flux vs density issues for DCl projectiles with resonant multiphoton ionization (REMPI) and 3D velocity map imaging methods, as recently demonstrated for HCl scattering from self-assembled monolayers (SAMs) of alkane thiols on Au films.[53]

We next turn to the dependence of the collision dynamics on the nature of the liquid surface (see Fig. 3.7). Most noticeable in Fig. 3.7b is that hyperthermal DCl systematically scatters from PFPE with considerably more energy in both rotational and translational degrees of freedom compared with the other liquids studied. This is in good agreement with both time-of-flight CO_2 studies by the Nathanson group and infrared based studies from our group.[17, 63-65]

Indeed, these studies show in general that the heavy, rough, and fluorinated surface leads to increased rotational excitation and less overall energy deposition into the surface. Secondly, glycerol and squalane liquids exhibit similar levels of T→R excitation for DCl. This behavior has also been noted previously in molecular beam CO_2 scattering studies from these liquids and has been used to argue that the presence of hydroxyl groups do not play a strong role in rotational excitation for impulsive scattering (IS) collision events[17]. In terms of transverse velocity distributions, however, a statistically greater momentum is transferred into the out of plane degree of freedom for glycerol than for squalane. This is in contrast to what was reported in previous CO_2 scattering studies, for which all three liquids were shown to produce perpendicular velocity distributions within experimental error.[17] If the OH groups were oriented parallel to the surface, this might offer a possible explanation for the differences between DCl and CO_2 scattering from glycerol. Such planar OH groups generate electric fields pointed along the surface, which would couple more strongly to the DCl dipole than to the vanishing dipole moment in CO_2, rationalizing stronger forces perpendicular to the scattering plane than for a non-polar hydrocarbon surface. The sum frequency generation studies of Oh-e et al.[66] provide additional support for this picture, with no free OH stretch and only a small amount hydrogen bonded OH groups detected, which implies OH groups lying predominantly parallel to interfacial plane or pointing down into the bulk.

3.4 Discussion

3.4.1 A simple lever-arm model

Although quantum state resolved molecular scattering from the gas-liquid interface represents an extremely complex dynamical event, it is a challenging but worthwhile exercise to explore simple, physically motivated models to reproduce the basic scattering phenomena. Indeed, there has been an extensive literature on quantum state resolved scattering of molecules in the gas phase and on single crystal surfaces, for which there have been many major theoretical advances.[40-43, 56, 58-59, 67-69] As a starting point, we can build intuition for molecular scattering from a liquid surface by considering the much simpler problem of diatomic scattering from a hard potential wall. This choice maps onto a long-studied problem in the gas and gas-solid phase energy transfer community,[67, 69-79] specifically tapping into the impulsive atom + diatom, "hard cube" and effective mass models by McCaffery, Tully, Minton and coworkers.[38-43] The essential physics captured in each of these treatments is that angular momentum transfer is dominated by impulsive collisions exerted on the atom or molecular rotor at the classical turning point, for which simple analytic expressions can be derived based on conservation of linear momentum, angular momentum and energy. Based on these pioneering efforts, we extend impulsive models for energy transfer on a wavy but locally flat surface (see Fig. 3.8a), as a simple entry point for incorporating stochastic capillary wave structure at the gas-liquid interface.

For the origin at the center of mass of a non-rotating diatomic (AB) colliding with a locally flat surface, conservation of angular momentum requires that

$$L = L' + J \qquad \text{Eq. 4}$$

where J is the asymptotic rotational angular momentum of AB and L and L' represent the initial and final orbital angular momenta before and after an impulsive collision. The initial orbital angular momentum (L) is given by

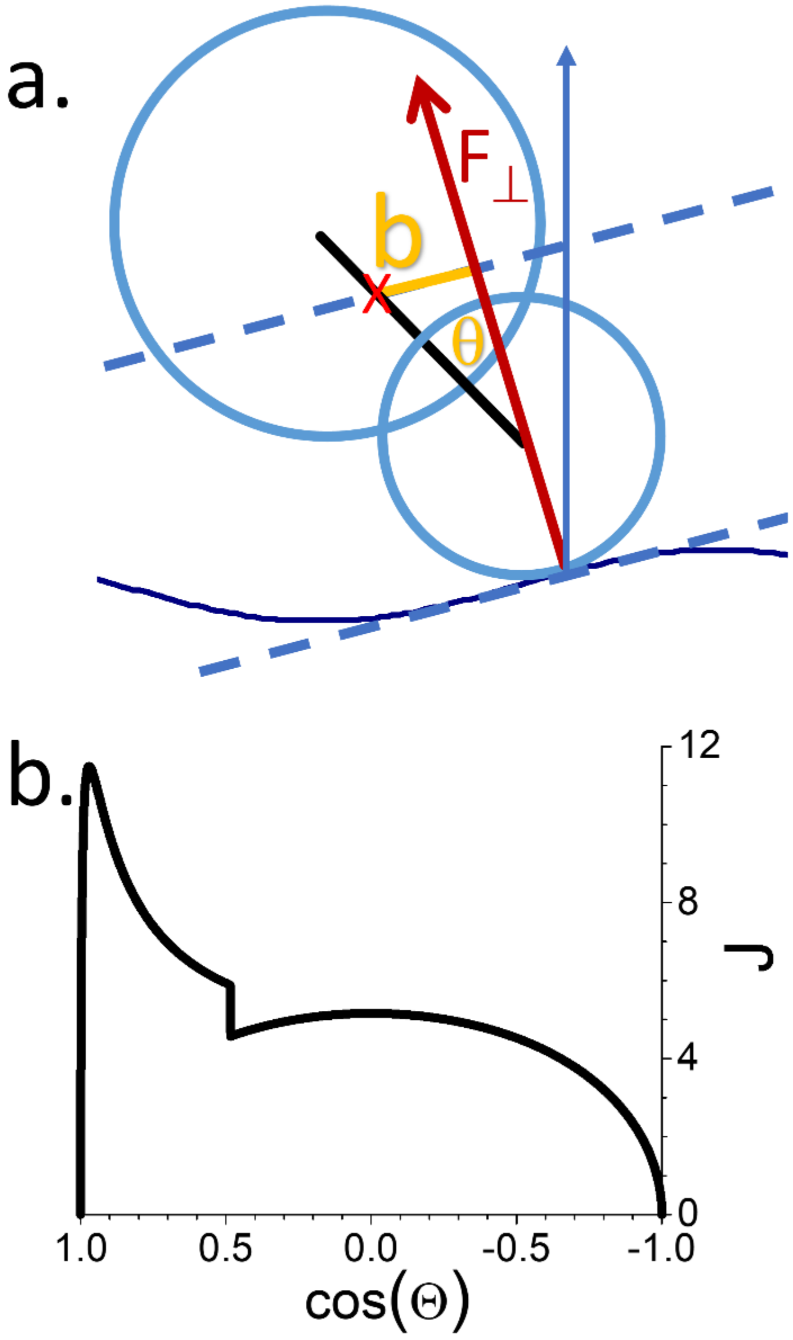

Figure 3.8: (a) Schematic “lever arm” model for impulsive scattering of a diatomic molecule from the gas-liquid interface. This diagram shows the two van der waal radii spheres with the black bar fixing the bond length of the molecule. The red arrow is the force normal to the surface of the liquid and the yellow bar represents the impact parameter of the surface collision. (b) Angular momentum (units of ħ) transferred due to torque of as a function of DCl orientation at the point of impulsive contact ($\theta = 0$ corresponds to the D atom directed antiparallel to the local surface normal).

$$L = \mu\, v_r\, b \qquad \text{Eq. 5}$$

where v_r represents the relative speed of the molecule + liquid surface system of reduced mass μ. The impact parameter b with which the torque on AB is generated is determined by the perpendicular distance between the AB center of mass and the force vector F originating at the impulsive classical turning point. From conservation of energy and momentum tangential to the surface, one can easily show for impulsive scattering that the final rotational angular momentum must be:

$$J = \frac{2\, I\, \mu\, v_r\, b}{\mu\, b^2 + I} \qquad \text{Eq. 6}$$

where I is the AB moment of inertia. If we further assume the surface mass to be much heavier than the scattering molecule, μ becomes the mass of AB. Due to limited degrees of freedom measured in this experiment, this assumption is made to simplify the model and not out of a priori scientific fact. Most of the analysis will be done with an infinite surface mass to avoid ad hoc parameters. All the terms in Eq. 6 are known except for the "lever arm" b, which will be a function of the locus of classical turning points for a given intermolecular potential energy surface and collision energy. Indeed, McCaffery et al. developed and used this exact scattering model to describe gas phase rotational excitation of CO by H atom collisions in the gas phase, treating the H-CO intermolecular potential as a hard wall ellipsoid[38] and averaging over all possible lever arm values of b weighted by the probability P(b) that such a lever arm would occur. For the present diatom-liquid surface scattering model, further simplification can be invoked since a locally flat surface makes explicit calculation of P(b) from the gas-surface potential even easier.

As the simplest representation of the AB + surface potential, we consider a dumbbell model of two hard spheres separated by a bond length R. Depending on which atom experiences the impulsive collision event, the lever arm length is given geometrically by:

$$b(\theta) = \begin{cases} \frac{m_{Cl}\,R}{m_{Cl}+m_D}\sin\theta\,,\ \theta < \theta_0 \\ \frac{m_D\,R}{m_{Cl}+m_D}\sin\theta\,,\ \theta \geq \theta_0 \end{cases} \qquad \text{Eq. 7}$$

where R = 1.275 Å is the DCl bond length, θ is the angle of the DCl bond axis with respect to the surface normal ($\theta = 0$ corresponds to the D atom pointing towards the surface), and θ_0 is the angle at which the impulsively colliding atom switches from D to Cl. For hard sphere radii r_{Cl}, r_D, this angle can be determined from:

$$\cos\theta_0 = \frac{(r_{Cl}-r_D)(m_{Cl}+m_D)}{R(m_{Cl}-m_D)} \qquad \text{Eq. 8}$$

These hard sphere radii can be estimated from the van der Waals radii of the respective atoms (1.75 Å for Cl and 1.20 Å for D), for which Eq. 8 predicts $\theta_0 \approx 61^{o}$. With θ_0 determined, Eqs. 6-8 permit one to calculate J as a function of cos(θ) for a given velocity component ($v_{\perp}$) normal to the average surface plane, which under the current hyperthermal beam conditions (E_{inc} = 11.5(5) kcal/mol, $\theta_{inc} = 65^{o}$) is $v_{\perp} \approx 6.8(1)x\ 10^4 cm/s$.

The resulting plot of J(θ) vs. cos(θ) for DCl scattering impulsively from a locally flat surface is displayed in Fig. 3.8b, revealing a particularly strong dependence of angular momentum transfer on orientation of the incident DCl. Orientations with either the D ($\theta = 0^{o}$) or Cl ($\theta = 180^{o}$) atom pointing exactly toward the surface obviously generate zero angular momentum. However, the angular momentum transfer grows quite steeply with tilt away from the cos(θ) = 1.0 and -1.0 limits, with maximal transfer occurring for striking with the D end with cos(θ) ≈ 0.971 ($\theta \approx 13.8^{o}$), but also with a smaller but much broader maximum for the Cl end near $\cos(\theta_0) \approx 0.0724$ ($\theta \approx 85.8^{\circ}$). This is consistent with simple physical observation that striking the lighter of the two atoms generates the larger "lever arm" for torqueing on the diatom. If at the moment of impact, the DCl angular orientation is assumed to be isotropic ($\theta = [0^{\circ}, 180^{\circ}]$, $\varphi = [0^{\circ}, 360^{\circ}]$), we can simply average over Eq. 6 to predict a mean final angular momentum of $\langle J \rangle \approx 5.1$. Considering the extreme simplicity of such a model treatment, we wish to emphasize that this is already in excellent qualitative agreement with the only modest levels of DCl rotational excitation ($\langle J_{exp} \rangle \approx 5.8$-$6.6$) observed for all three liquids (see Fig. 3.6).

The actual quantum state distributions can be predicted from this "lever arm" model by using Monte Carlo methods to sample orientation of the molecular bond axis with respect to the local surface normal. For an isotropic distribution of θ, φ sampled from the usual $\sin(\theta)d\theta d\phi$ Jacobian, we can therefore histogram $J(\theta)$ into integer values and thus predict rotational quantum state distribution for impulsive collisions with a static flat liquid surface. The resulting histogram from such a calculation is shown in Fig. 3.9a, which reveals a highly peaked rotational distribution with a pronounced maximum near $J \approx 5$. This peaking is of course simply an example of "rotational rainbow" structure, both predicted and observed in crossed molecular beam and gas-single crystal scattering studies.[80-82] This sharp rainbow peak is clearly the result of the broad maximum in $J(\theta)$ around $J \approx 5$, $\cos(\theta) \approx -0.1$, which is the essential ingredient for a classical rainbow (see Fig. 3.8b).[80-82] Interestingly, this rainbow feature clearly identifies that the reduced levels of DCl rotational excitation observed experimentally arise from the higher probability of scattering with the Cl vs. D atom end first, which results in correspondingly smaller impact parameters for rotationally exciting the DCl subunit. However, it is also important to note that Fig. 3.8b predicts dramatic enhancement of the rotational excitation efficiency for *non-isotropic sampling of the D atom orientation* prior to the collisional event, as could be achieved for a light dipolar hydride such as DCl by strongly charged species or molecular ions in the interfacial region.[83]

3.4.2 Averaging over capillary waves predicts hot yet Boltzmann-like rotational distributions

We can push this "lever arm" analysis further to capture even more of the trends observed in gas-liquid interfacial collisions. Specifically, the angular momentum predictions from our simple "lever arm" model (e.g., see Fig. 3.9a) may be correct *on average* but greatly overestimate the degree of sharp "rainbow" structure in the J distributions. This is due to our assumption of impulsive collisions on a locally flat collision surface, whereas any gas-liquid interface of course exhibits substantial roughness due to capillary wave excitation. As the next stage of treatment, therefore, we empirically incorporate surface roughness in our gas-liquid collision model, the major source of which is from thermal activated capillary waves. From the theoretical analysis by Phillips,[44] the root mean square angle for surface deviation from normal is found to be:

$$\tan\theta_{rms} = \sqrt{\frac{\pi\, k_b T}{8\gamma\sigma^2}} \qquad \text{Eq. 10}$$

where γ is the surface tension and σ is the molecular diameter of the liquid. This model of surface roughness predicts a range of $\theta_{rms} \approx 18.2^{o}$ (PFPE) to 13.7^{o} (squalane) to 18.1^{o} (glycerol) for the capillary wave angular deviations, with values of the input parameters found in Table 1.

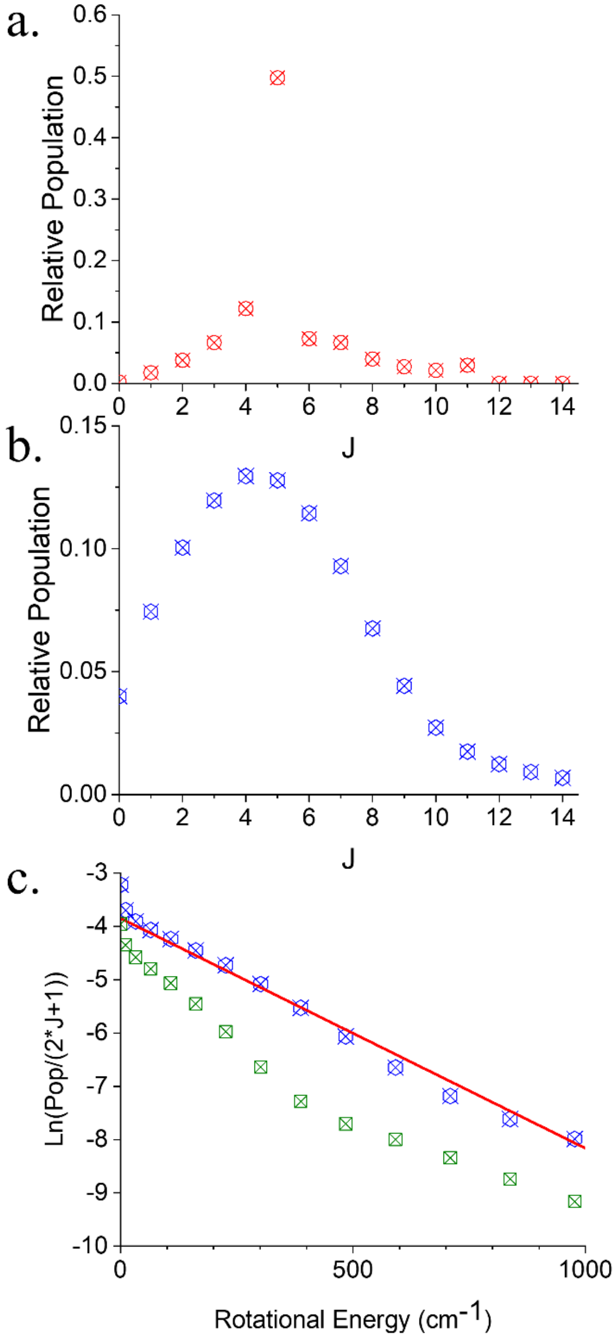

Figure 3.9: Simulated PFPE surface scattering using parameters found in table 1. (a) Distribution of DCl (J) populations predicted from a simple "lever arm" model. (b) Predicted populations thermally averaged over the distribution of local surface tilt angles (θ_s) due to capillary waves at the gas-liquid interface. (c) Blue data corresponds to Boltzmann plot of data in (b) and green data is for a finite mass of 120 amu, whose linearity reflects a "near temperature-like" behavior (T ≈ 400-500 K) consistent with observations from many quantum state resolved gas-liquid experiments.

The obvious next step is to combine these lever arm model predictions with the above capillary wave estimates of surface roughness. A simple way to incorporate surface roughness would be to assume the surface to be locally flat at the point of impact, but to allow the direction of the surface normal to fluctuate according to predictions of capillary wave theory in Eq. 10. The only difference is that we must now also additionally average over fluctuations in the normal velocity component,

$$\|v_r\| = \vec{v} \cdot \vec{n} = \|v\| * (\cos\theta_s * \cos\theta_{inc} + \cos\phi_s * \sin\theta_s * \sin\theta_{inc}) \qquad \text{Eq. 11}$$

where (θ_s, ϕ_s) are the instantaneous spherical polar angles associated with the local surface normal (with $\phi_s = 0$ pointing in the forward scattering direction) and θ_{inc} is the incident molecular beam angle measured with respect to the global surface normal. Most importantly, such averaging will contribute to a blurring of the sharp rotational rainbow-like structure in Fig. 3.9a.

We can perform such an angular average explicitly. If there is no preferential azimuthal direction in the liquid surface, ϕ_s will be evenly distributed over $[0, 360^o]$. However, the distribution in the local tilt angle $\theta_s$is not uniform, with θ_s distributed as a Gaussian around $\theta_s \approx 0$ weighted by usual the $\sin(\theta_s)$ Jacobian for a spherical polar coordinate system:

$$P(\theta_s) \propto \sin\theta_s * e^{-\frac{1}{2}(\frac{\theta_s}{\theta_0})^2} \approx \theta_s * e^{-\frac{1}{2}\frac{\theta_S^2}{(\pi k_S T_S/8\gamma\sigma^2)}} \quad , \qquad \text{Eq. 12}$$

where θ_0 is the rms angular roughness from capillary wave theory (θ_{rms} in Eq. 10) and $\sin(\theta_s) \approx \theta_s$ can be taken in the small angle limit. The gaussian angular distribution naturally follows from Phillips' work. See appendix A for a clear derivation of this fact. The predicted J distribution from Eqs. 10-12 is plotted in Fig. 3.9b, where we have taken values for γ and σ consistent with PFPE (i.e., θ_0 = 18.1°, see Table 3.1). Most importantly, averaging over capillary wave distributions at the gas-liquid interface has smoothed over the strongly peaked rainbow-like features predicted for a static, locally flat surface (Fig. 3.9a), resulting in quantum state distributions much more visually consistent with experimental observation (e.g., Fig. 3.6).

As a final observation, we can take this analysis one step further by recasting the above J distributions in terms of a Boltzmann plot, i.e., ln[Pop/(2J+1)] vs E_{rot} (see Fig. 3.9c). The resulting plots are remarkably linear, indeed quite characteristic of a "temperature-like" behavior at $T \approx 400$ - 500 K. Figure 3.9c also contains the data for a finite surface mass of 120 amu, which shows a slightly colder but still linear "temperature-like" behavior. This is a particularly striking result, specifically that thermal averaging of an impulsive, classical rotational excitation model over surface capillary wave roughness recapitulates the "hot-but-Boltzmann-like" distributions experimentally observed in many quantum state resolved scattering studies to date.[17-20, 22-26] To the best of our knowledge, this is the first theoretical justification for the appearance of such "dual temperature" (i.e., T_{TD} and T_{IS}) behavior in rotational gas-liquid scattering dynamics, despite the ubiquitous evidence for such behavior in the literature.

This, however, is not a complete explanation of IS scattering. Several major assumptions were made in this model for the sake of simplicity. Finite surface mass has been shown to accurately explain angular distributions in atom-liquid scattering and it is completely possible that variations in surface mass can add to the averaging over the rotational rainbow structure.[39] Also MD studies have shown that surface interactions often undergo multiple collisions and each of these collisions cannot be categorized as a truly impulsive collision.[84] This does not weaken the fact that impulsive molecular scattering produces rotational rainbows and that gaussian averaging over such rotational rainbows gives temperature-like rotational behavior. The largest source of gaussian broadening is most likely from surface capillary waves but there are many sources that can have strong contributions to this averaging. A more accurate model should be developed and it would encompass all of these effects.

Given these level arm model results, it would appear that characterization of the IS component with some effective "temperature" does not require any true equilibration taking place during the gas-liquid surface interaction. This is in agreement with experiment as well as the identification of IS scattering as arising from gas-liquid scattering dynamics with insufficient time to lose all memory of the incident collision conditions. This is also particularly noteworthy in light of the fact that the in-plane velocity distributions for the IS scattering component have been routinely determined from time-of-flight studies by Nathanson, Minton, and others to be i) lobularly peaked toward the near specular angle and ii) with velocities poorly represented by a translational temperature.[10, 15-16, 39] It is our hope that future theoretical and experimental efforts will permit further developments in this direction to provide a simple, quasi-predictive model for quantum state resolved impulsive scattering of molecules from the gas-liquid interface.

3.5 Conclusions and Summary

Jet cooled DCl(J = 0, 1) has been scattered at thermal (1.5(1) kcal/mol) and hyperthermal (11.5(5) kcal/mol) collision energies from surfaces of three prototypical liquids (PFPE, squalene, and glycerol), with the data revealing several key ideas. First of all, the TD component of DCl desorbing in equilibrium (in both rotationally and transverse velocity distributions) with the liquid ($T_{Dopp} \approx T_{rot} \approx T_S$) implies by detailed balance that the sticking coefficient for DCl in the reverse direction must be unity over a similar range of thermal collision energies.[55-59]

Secondly, impulsive scattering of hyperthermal DCl molecules proves to be far less efficient at channeling incident translational energy into rotational degrees of freedom (<J> ~ 5,

$T_{IS,rot} \approx$ 400-500 K) than for CO_2 or NO. We interpret this as simply arising from the much larger rotational constant ($B_{DCl} \approx 5.4$ cm^{-1} vs. $B_{CO2} \approx .5$ cm^{-1}) larger rotational spacings, and thus the correspondingly larger changes in rotational energy required for a light hydride rotor. In contrast, however, DCl transfers its incident momentum very strongly into the out-of-plane velocity component, achieving Boltzmann temperatures ($T_{IS,trans} \approx$ 1000−1600 K) from fits to the high resolution Doppler profiles 3-4 fold higher than the corresponding rotational temperatures ($T_{IS,rot}$ $\approx$ 400-500 K).

Thirdly, we present a simple physical "lever arm" model based on early gas and interfacial phase collisional energy transfer studies by McCaffery, Tully and Minton and coworkers,[38-43] that successfully rationalizes both the low levels of average DCl rotational excitation observed but also makes clear predictions for how angular orientation of the incident projectile can strongly impact the degree of rotational excitation. Viewed from this perspective, such a "lever arm" model provides an intriguing potential route to probing the degree of anisotropic orientation of impulsively scattered molecules (especially light and strongly polar hydrides) as they collide with a gas-liquid surface. Finally and most importantly, appropriately averaging such "level arm" model predictions over capillary wave surface roughness yields rotational distributions for hyperthermal collision energies that recapitulate the ubiquitous pattern of "hot-but-Boltzmann-like" temperatures reported empirically in the literature for over a decade. More comprehensive theory will clearly be needed to make these connections more quantitative, but the current results leave us hopeful that the prospects for understanding the essential underlying physics of quantum state resolved energy transfer of molecules at the gas-liquid interface are improving.

Chapter 3 References

1. Kolb, C. E., et al., An Overview of Current Issues in the Uptake of Atmospheric Trace Gases by Aerosols and Clouds. *Atmos. Chem. Phys.* **2010**, *10*, 10561-10605.
2. Xie, X. W.; Li, Y.; Liu, Z. Q.; Haruta, M.; Shen, W. J., Low-Temperature Oxidation of CO Catalysed by CO_3O_4 Nanorods. *Nature* **2009**, *458*, 746-749.
3. Yin; Liebscher, J., Carbon−Carbon Coupling Reactions Catalyzed by Heterogeneous Palladium Catalysts. *Chem. Rev.* **2007**, *107*, 133-173.
4. Kroll, J. H.; Seinfeld, J. H., Chemistry of Secondary Organic Aerosol: Formation and Evolution of Low-Volatility Organics in the Atmosphere. Atmos. Environ. **2008**, *42*, 3593-3624.
5. Hammerich, A. D.; Finlayson-Pitts, B. J.; Gerber, R. B., Mechanism for Formation of Atmospheric Cl Atom Precursors in the Reaction of Dinitrogen Oxides with HCl/Cl- on Aqueous Films. *Phys. Chem. Chem. Phys.* **2015**, *17*, 19360-19370.
6. Hammerich, A. D.; Finlayson-Pitts, B. J.; Gerber, R. B., NO_x Reactions on Aqueous Surfaces with Gaseous HCl: Formation of a Potential Precursor to Atmospheric Cl Atoms. *J. Phys. Chem. Lett.* **2012**, *3*, 3405-3410.
7. Vandoren, J. M.; Watson, L. R.; Davidovits, P.; Worsnop, D. R.; Zahniser, M. S.; Kolb, C. E., Temperature-Dependence of the Uptake Coefficients of HNO_3, HCl, and N_2O_5 by Water Droplets. *J Phys. Chem-Us* **1990**, *94*, 3265-3269.
8. Watson, L. R.; Vandoren, J. M.; Davidovits, P.; Worsnop, D. R.; Zahniser, M. S.; Kolb, C. E., Uptake of HCl Molecules by Aqueous Sulfuric-Acid Droplets as a Function of Acid Concentration. *J. Geophys. Res-Atmos* **1990**, *95*, 5631-5638.
9. Nathanson, G. M., Molecular Beam Studies of Gas-Liquid Interfaces. *Annu. Rev. Phys. Chem.* **2004**, *55*, 231-255.
10. Tesa-Serrate, M. A.; Smoll, E. J.; Minton, T. K.; McKendrick, K. G., Atomic and Molecular Collisions at Liquid Surfaces. *Annu. Rev. Phys. Chem.* **2016**, *67*, 515-540.
11. Waring, C.; King, K. L.; Bagot, P. A. J.; Costen, M. L.; McKendrick, K. G., Collision Dynamics and Reactive Uptake of OH Radicals at Liquid Surfaces of Atmospheric Interest. *Phys. Chem. Chem. Phys.* **2011**, *13*, 8457-8469.
12. Wu, B. H.; Zhang, J. M.; Minton, T. K.; McKendrick, K. G.; Slattery, J. M.; Yockel, S.; Schatz, G. C., Scattering Dynamics of Hyperthermal Oxygen Atoms on Ionic Liquid Surfaces: [emim][NTf_2] and [C_{12}mim][NTf_2]. *J. Phys. Chem. C* **2010**, *114*, 4015-4027.
13. Bagot, P. A. J.; Waring, C.; Costen, M. L.; McKendrick, K. G., Dynamics of Inelastic Scattering of OH Radicals from Reactive and Inert Liquid Surfaces. *J. Phys. Chem. C* **2008**, *112*, 10868-10877.
14. Wiens, J. P.; Nathanson, G. M.; Alexander, W. A.; Minton, T. K.; Lakshmi, S.; Schatz, G. C., Collisions of Sodium Atoms with Liquid Glycerol: Insights into Solvation and Ionization. *J. Am. Chem. Soc.* **2014**, *136*, 3065-3074.
15. King, M. E.; Fiehrer, K. M.; Nathanson, G. M.; Minton, T. K., Effects of Thermal Roughening on the Angular Distributions of Trapping and Scattering in Gas-Liquid Collisions. *J Phys. Chem. A* **1997**, *101*, 6556-6561.
16. King, M. E.; Nathanson, G. M.; Hanninglee, M. A.; Minton, T. K., Probing the Microscopic Corrugation of Liquid Surfaces with Gas-Liquid Collisions. *Phys. Rev. Lett.* **1993**, *70*, 1026-1029.

17. Perkins, B. G.; Nesbitt, D. J., Quantum-State-Resolved CO_2 Scattering Dynamics at the Gas-Liquid Interface: Incident Collision Energy and Liquid Dependence. *J. Phys. Chem. B* **2006**, *110*, 17126-17137.
18. Ziemkiewicz, M. P.; Zutz, A.; Nesbitt, D. J., Inelastic Scattering of Radicals at the Gas-Ionic Liquid Interface: Probing Surface Dynamics of Bmim-Cl, Bmim-BF_4, and Bmim-Tf_2N by Rovibronic Scattering of NO [$^2p_{1/2}$(0.5)]. *J. Phys. Chem. C* **2012**, *116*, 14284-14294.
19. Zutz, A.; Nesbitt, D. J., Nonadiabatic Spin-Orbit Excitation Dynamics in Quantum-State-Resolved NO($^2\Pi_{1/2}$) Scattering at the Gas-Room Temperature Ionic Liquid Interface. *J. Phys. Chem. C* **2015**, *119*, 8596-8607.
20. Zutz, A.; Nesbitt, D. J., Quantum State-Resolved Molecular Scattering of NO ($^2\Pi_{1/2}$) at the Gas-[$C_n$mim][TF_2N] Room Temperature Ionic Liquid Interface: Dependence on Alkyl Chain Length, Collision Energy, and Temperature. *AIP. Adv.* **2016**, *6*.
21. Ziemkiewicz, M. P.; Roscioli, J. R.; Nesbitt, D. J., State-to-State Dynamics at the Gas-Liquid Metal Interface: Rotationally and Electronically Inelastic Scattering of NO[$^2\Pi_{1/2}$ (0.5)] from Molten Gallium. *J. Chem. Phys.* **2011**, *134*.
22. Perkins, B. G.; Nesbitt, D. J., Toward Three-Dimensional Quantum State-Resolved Collision Dynamics at the Gas-Liquid Interface: Theoretical Investigation of Incident Angle. *J Phys. Chem. A* **2009**, *113*, 4613-4625.
23. Perkins, B. G.; Nesbitt, D. J., High Resolution Dopplerimetry of Correlated Angular and Quantum State-Resolved CO_2 Scattering Dynamics at the Gas-Liquid Interface. *Phys. Chem. Chem. Phys.* **2010**, *12*, 14294-14308.
24. Perkins, B. G.; Haber, T.; Nesbitt, D. J., Quantum State-Resolved Energy Transfer Dynamics at Gas-Liquid Interfaces: IR Laser Studies of CO_2 Scattering from Perfluorinated Liquids. *J. Phys. Chem. B* **2005**, *109*, 16396-16405.
25. Perkins, B. G.; Nesbitt, D. J., Quantum-State-Resolved CO_2 Scattering Dynamics at the Gas-Liquid Interface: Dependence on Incident Angle. *J. Phys. Chem. A* **2007**, *111*, 7420-7430.
26. Perkins, B. G.; Nesbitt, D. J., Quantum State-Resolved CO_2 Collisions at the Gas-Liquid Interface: Surface Temperature-Dependent Scattering Dynamics. *J. Phys. Chem. B* **2008**, *112*, 507-519.
27. Ringeisen, B. R.; Muenter, A. H.; Nathanson, G. M., Collisions of HCl, DCl, and HBr with Liquid Glycerol: Gas Uptake, D -> H Exchange, and Solution Thermodynamics. *J. Phys. Chem. B* **2002**, *106*, 4988-4998.
28. Ringeisen, B. R.; Muenter, A. H.; Nathanson, G. M., Collisions of DCl with Liquid Glycerol: Evidence for Rapid, near-Interfacial D -> H Exchange and Desorption. *J. Phys. Chem. B* **2002**, *106*, 4999-5010.
29. Chorny, I.; Benjamin, I.; Nathanson, G. M., Scattering, Trapping, and Ionization of HCl at the Surface of Liquid Glycerol. *J. Phys. Chem. B* **2004**, *108*, 995-1002.
30. Muenter, A. H.; DeZwaan, J. L.; Nathanson, G. M., Collisions of DCl with Pure and Salty Glycerol: Enhancement of Interfacial D -> H Exchange by Dissolved NaI. *J. Phys. Chem. B* **2006**, *110*, 4881-4891.
31. DeZwaan, J. L.; Brastad, S. M.; Nathanson, G. M., Evidence for Interfacial $[FDCl]^-$ in Collisions between DCl and F^- in KF-Glycerol Solutions. *J. Phys. Chem. C* **2008**, *112*, 15449-15457.
32. DeZwaan, J. L.; Brastad, S. M.; Nathanson, G. M., The Roles of Salt Concentration and Cation Charge in Collisions of Ar and DCl with Salty Glycerol Solutions of NaI and CaI_2. *J. Phys. Chem. C* **2008**, *112*, 3008-3017.

33. Brastad, S. M.; Albert, D. R.; Huang, M. W.; Nathanson, G. M., Collisions of DCl with a Solution Covered with Hydrophobic and Hydrophilic Ions: Tetrahexylammonium Bromide in Glycerol. *J. Phys. Chem. A* **2009**, *113*, 7422-7430.
34. Dempsey, L. P.; Brastad, S. M.; Nathanson, G. M., Interfacial Acid Dissociation and Proton Exchange Following Collisions of DCl with Salty Glycerol and Salty Water. *J. Phys. Chem. Lett.* **2011**, *2*, 622-627.
35. Brastad, S. M.; Nathanson, G. M., Molecular Beam Studies of HCl Dissolution and Dissociation in Cold Salty Water. *Phys. Chem. Chem. Phys.* **2011**, *13*, 8284-8295.
36. Faust, J. A.; Nathanson, G. M., Microjets and Coated Wheels: Versatile Tools for Exploring Collisions and Reactions at Gas-Liquid Interfaces. *Chem. Soc. Rev.* **2016**, *45*, 3609-3620.
37. Faust, J. A.; Sobyra, T. B.; Nathanson, G. M., Gas-Microjet Reactive Scattering: Collisions of HCl and DCl with Cool Salty Water. *J. Phys. Chem. Lett.* **2016**, *7*, 730-735.
38. Whitely, T. W. J.; McCaffery, A. J., Angular Momentum Analysis of Rotational Transfer of Superthermal Relative Velocity Distributions. *J. Phys. B-At. Mol. Opt.* **1996**, *29*, 6133-6141.
39. Zhang, J. M.; Garton, D. J.; Minton, T. K., Reactive and Inelastic Scattering Dynamics of Hyperthermal Oxygen Atoms on a Saturated Hydrocarbon Surface. *J. Chem. Phys.* **2002**, *117*, 6239-6251.
40. Tully, J. C., Washboard Model of Gas Surface Scattering. *J. Chem. Phys.* **1990**, *92*, 680-686.
41. Doll, J. D., Simple Classical Model for Scattering of Diatomic-Molecules from a Solid Surface. *J. Chem. Phys.* **1973**, *59*, 1038-1042.
42. Nichols, W. L.; Weare, J. H., Rotational Energy-Distributions for Homonuclear Diatomic Beams Scattered from Solid-Surfaces - Hard-Cube Model. *J. Chem. Phys.* **1977**, *66*, 1075-1078.
43. Nichols, W. L.; Weare, J. H., Homonuclear Diatomic Scattering from Solid-Surfaces - Hardcube Model. *J. Chem. Phys.* **1975**, *62*, 3754-3762.
44. Phillips, L. F., Velocity and Angular Distributions of Molecules Emitted from a Liquid Surface. *Chem. Phys. Lett.* **1997**, *266*, 161-168.
45. Gisler, A. W.; Nesbitt, D. J., On Probing Ions at the Gas-Liquid Interface by Quantum State-Resolved Molecular Beam Scattering: The Curious Incident of the Cation in the Night Time. *Faraday Discuss.* **2012**, *157*, 297-305.
46. Nizkorodov, S. A.; Harper, W. W.; Chapman, W. B.; Blackmon, B. W.; Nesbitt, D. J., Energy-Dependent Cross Sections and Nonadiabatic Reaction Dynamics in $F(^2P_{3/2}, ^2P_{1/2})+n\text{-}H_2 \rightarrow HF(v,J)+H$. *J. Chem. Phys.* **1999**, *111*, 8404-8416.
47. Lednovich, S. L.; Fenn, J. B., Absolute Evaporation Rates for Some Polar and Nonpolar Liquids. *Aiche. J.* **1977**, *23*, 454-459.
48. Curl, R. F.; Capasso, F.; Gmachl, C.; Kosterev, A. A.; McManus, B.; Lewicki, R.; Pusharsky, M.; Wysocki, G.; Tittel, F. K., Quantum Cascade Lasers in Chemical Physics. *Chem. Phys. Lett.* **2010**, *487*, 1-18.
49. Weida, M. J.; Caffey, D.; Rowlette, J. A.; Arnone, D. F.; Day, T., Utilizing Broad Gain Bandwidth in Quantum Cascade Devices. *Opt. Eng.* **2010**, *49*.
50. Knabe, K.; Williams, P. A.; Giorgetta, F. R.; Armacost, C. M.; Crivello, S.; Radunsky, M. B.; Newbury, N. R., Frequency Characterization of a Swept- and Fixed-Wavelength External-Cavity Quantum Cascade Laser by Use of a Frequency Comb. *Opt. Express* **2012**, *20*, 12432-12442.

51. Davies, P. R.; Orville-Thomas, W. J., Infrared Band Intensities and Bond Polarities: Part I. Bond Moment Constants in CO_2, OCS, CS_2, CSe_2 and SCSe. *J. Mol. Struct.* **1969**, *4*, 163-177.
52. Arunan, E.; Setser, D. W.; Ogilvie, J. F., Vibration-Rotational Einstein Coefficients for HF DF and HCl DCl. *J. Chem. Phys.* **1992**, *97*, 1734-1741.
53. Hoffman, C. H.; Nesbitt, D. J., Quantum State Resolved 3D Velocity Map Imaging of Surface Scattered Molecules: Incident Energy Effects in HCl Plus Self-Assembled Monolayer Collisions. *J. Phys. Chem. C* **2016**, *120*, 16687-16698.
54. Perkins, B. G.; Nesbitt, D. J., Stereodynamics at the Gas-Liquid Interface: Orientation and Alignment of CO_2 Scattered from Perfluorinated Liquid Surfaces. *J. Phys. Chem. A* **2010**, *114*, 1398-1410.
55. Iche, G.; Nozieres, P., Simple Stochastic Description of Desorption Rates. *J. Phys-Paris* **1976**, *37*, 1313-1323.
56. Rendulic, K. D., Sticking and Desorption - a Review. *Surf. Sci.* **1992**, *272*, 34-44.
57. Rettner, C. T.; Schweizer, E. K.; Mullins, C. B., Desorption and Trapping of Argon at a 2H-W(100) Surface and a Test of the Applicability of Detailed Balance to a Nonequilibrium System. *J. Chem. Phys.* **1989**, *90*, 3800-3813.
58. Tully, J. C., The Dynamics of Adsorption and Desorption. *Surf. Sci.* **1994**, *299*, 667-677.
59. Wenaas, E. P., Equilibrium Cosine Law and Scattering Symmetry at Gas-Surface Interface. *J. Chem. Phys.* **1971**, *54*, 376.
60. Lohr, J. R.; Day, B. S.; Morris, J. R., Scattering, Accommodation, and Trapping of HCl in Collisions with a Hydroxylated Self-Assembled Monolayer. *J. Phys. Chem. B* **2005**, *109*, 15469-15475.
61. Nelson, R. D.; Lide, D. R.; Maryott, A. A., *Selected Values of Electric Dipole Moments for Molecules in the Gas Phase*; U.S. National Bureau of Standards: Washington, 1967, p v, 49 p.
62. Graham, C.; Imrie, D. A.; Raab, R. E., Measurement of the Electric Quadrupole Moments of CO_2, CO, N_2, Cl_2 and BF_3. *Mol. Phys.* **1998**, *93*, 49-56.
63. Saecker, M. E.; Nathanson, G. M., Collisions of Protic and Aprotic Gases with a Perfluorinated Liquid. *J. Chem. Phys.* **1994**, *100*, 3999-4005.
64. Saecker, M. E.; Nathanson, G. M., Collisions of Protic and Aprotic Gases with Hydrogen-Bonding and Hydrocarbon Liquids. *J. Chem. Phys.* **1993**, *99*, 7056-7075.
65. Saecker, M. E.; Nathanson, G. M., Bouncing Gases Off Liquids - Collisions of Protic and Aprotic Solutes with Hydrocarbon and Hydrogen-Bonding Solvents. *Abstr. Pap. Am. Chem. S.* **1992**, *203*, 237-Phys.
66. Oh-e, M.; Yokoyama, H.; Baldelli, S., Structure of the Glycerol Liquid/Vapor Interface Studied by Sum-Frequency Vibrational Spectroscopy. *Appl. Phys. Lett.* **2004**, *84*, 4965-4967.
67. Adelman, S. A.; Doll, J. D., Generalized Langevin Equation Approach for Atom-Solid-Surface Scattering - General Formulation for Classical Scattering Off Harmonic Solids. *J. Chem. Phys.* **1976**, *64*, 2375-2388.
68. Schinke, R., Rotational Rainbows in Diatom (Solid) Surface Scattering. *J. Chem. Phys.* **1982**, *76*, 2352-2359.
69. Rettner, C. T.; Auerbach, D. J.; Tully, J. C.; Kleyn, A. W., Chemical Dynamics at the Gas−Surface Interface. *J. Phys. Chem.* **1996**, *100*, 13021-13033.
70. Miller, W. H., Coupled Equations and Minimum Principle for Collisions of an Atom and a Diatomic Molecule Including Rearrangements. *J. Chem. Phys.* **1969**, *50*, 407.

71. Pack, R. T., Space-Fixed Vs Body-Fixed Axes in Atom-Diatomic Molecule Scattering - Sudden Approximations. *J Chem Phys* **1974**, *60*, 633-639.
72. Arthurs, A. M.; Dalgarno, A., The Theory of Scattering by a Rigid Rotator. *P. Roy. Soc. Lond. A MAT.* **1960**, *256*, 540-551.
73. Coltrin, M. E.; Kay, B. D., Quasiclassical Trajectory Study of Rotational Energy-Transfer in the Scattering of NH_3 from a Flat, Rigid Gold Surface. *J. Chem. Phys.* **1988**, *89*, 551-561.
74. Flynn, G. W., Collision-Induced Energy-Flow between Vibrational-Modes of Small Polyatomic-Molecules. *Accounts Chem. Res.* **1981**, *14*, 334-341.
75. Moore, C. B., Vibration-Rotation Energy Transfer. *J. Chem. Phys.* **1965**, *43*, 2979.
76. Kleyn, A. W.; Luntz, A. C.; Auerbach, D. J., Rotational Energy-Transfer in Direct Inelastic Surface Scattering - NO on Ag(111). *Phys. Rev. Lett.* **1981**, *47*, 1169-1172.
77. Flynn, G. W.; Parmenter, C. S.; Wodtke, A. M., Vibrational Energy Transfer. *J. Phys. Chem.* **1996**, *100*, 12817-12838.
78. Huang, Y. H.; Rettner, C. T.; Auerbach, D. J.; Wodtke, A. M., Vibrational Promotion of Electron Transfer. *Science* **2000**, *290*, 111-114.
79. Neumark, D. M.; Wodtke, A. M.; Robinson, G. N.; Hayden, C. C.; Lee, Y. T., Molecular-Beam Studies of the $F+H_2$ Reaction. *J. Chem. Phys.* **1985**, *82*, 3045-3066.
80. Park, G. B.; Kruger, B. C.; Meyer, S.; Kandratsenka, A.; Wodtke, A. M.; Schafer, T., An Axis-Specific Rotational Rainbow in the Direct Scatter of Formaldehyde from Au(111) and Its Influence on Trapping Probability. *Phys. Chem. Chem. Phys.* **2017**, *19*, 19904-19915.
81. Korsch, H. J.; Lewis, Z. V.; Poppe, D., On Classical Rotational Rainbow Structures for Initially Rotating Molecules. *Z. Phys. a-Hadron Nucl.* **1983**, *312*, 277-284.
82. Korsch, H. J.; Richards, D., On Classical Rotational Rainbows. *J. Phys. B-at Mol. Opt.* **1981**, *14*, 1973-1981.
83. Jungwirth, P.; Tobias, D. J., Ions at the Air/Water Interface. *J. Phys. Chem. B* **2002**, *106*, 6361-6373.
84. Nogueira, J. J.; Vazquez, S. A.; Mazyar, O. A.; Hase, W. L.; Perkins, B. G.; Nesbitt, D. J.; Martinez-Nunez, E., Dynamics of CO_2 Scattering Off a Perfluorinated Self-Assembled Monolayer. Influence of the Incident Collision Energy, Mass Effects, and Use of Different Surface Models. *J. Phys. Chem. A* **2009**, *113*, 3850-3865.

Chapter 4

Low Energy CO Scattering at the Gas-Liquid Interface: Experimental/Theoretical Evidence for a Novel Sub-Thermal Impulsive Scattering (STIS) Channel*

4.1 Introduction

Ever since the earliest experimental attempts to probe fundamental scattering at the gas-liquid interface, compelling evidence has been reported for two physically distinct pathways.[1-4] The first is the thermal desorption pathway (TD), whereby the incident molecular projectile traps transiently on the liquid surface and undergoes multiple collisional interactions, which causes it to *lose all memory* of the incident collision conditions (e.g., speed, direction, quantum state), and desorb in perfect equilibrium with the liquid temperature (T_S). This TD pathway has been presumed to dominate at collision energies comparable to the surface temperature ($E_{inc} \approx kT_S$), as confirmed by multiple energy-dependent studies of the final external (i.e., translational) and internal (i.e., rovibrational) quantum state distributions.[5,6] To help minimize further potential confusion in the literature, we note that such TD dynamics (i.e., “complete loss of incident quantum state memory”) is consistent with but does *not strictly require* the final distribution to be in perfect equilibrium with T_S. As one specific example, non-equilibrium distributions are in fact *rigorously predicted* by detailed balance considerations if there is some potential energy barrier (e.g., in projectile-surface displacement or angle) serving as a transition state bottleneck along the desorption coordinate. This is known to be the case, for example, for H_2 molecules scattering from Ni, Pt, and Fe, for which a potential barrier in the adsorption coordinate results in high p_z momentum distributions and narrower than $\cos(\theta)$ angular distributions in the corresponding desorption dynamics.[7] This behavior has also been seen in a multitude of systems[8] such as the oxidation of

---

*Published in J Phys. Chem. C, 124, 28006, (2020) CO on Rh(111), which has an exit channel barrier for the product (CO_2) leaving the surface.[9] Evidence for such transition state barrier complications in quantum state resolved scattering studies at the gas-liquid interface has not been reported to date. However, given the rapid progress in this field, it is likely only a matter of time, apparatus sophistication, and experimental sensitivity before such evidence will emerge.

As the familiar counterpart to TD, a second dynamical pathway emerges as a function of increasing collision energy dubbed impulsive scattering (IS), whereby the molecules *retain a partial memory* of the incident collision conditions. One of the earliest papers to identify and label this channel was published by Hurst et al. As noted by Hase and coworkers, this molecular memory is not an experimental observable, and thus such a "catch-all" pathway has no *a priori* rigorous definition.[10] For example, were the IS dynamical pathway to result in distributions that coincidentally matched those of pure TD scattering, these would be indistinguishable from (and by definition subsumed into) the TD pathway. Experimentally, however, distinguishable IS and TD pathways are routinely observed in numerous quantum state-resolved and time-of-flight (TOF) gas-liquid scattering studies.[1,5,11-14] Particularly under glancing incident scattering conditions, such IS deviations from pure $\cos(\theta)$ TD thermalization dynamics have been empirically well described by an additive, near specular component with translational distributions often hotter than the surface (though not necessarily Boltzmann) and with an average energy content scaling with the incident collision energy. A schematic cartoon of these two pathways is illustrated in Fig. 4.1, which portrays the two limits of i) pure $\cos(\theta)$ and ii) quasi-specular angular distributions for the TD and IS pathways, respectively.

Although no predictive theory currently exists that successfully recapitulates all observed gas-liquid scattering behavior, there have been several heuristic models that capture much of the

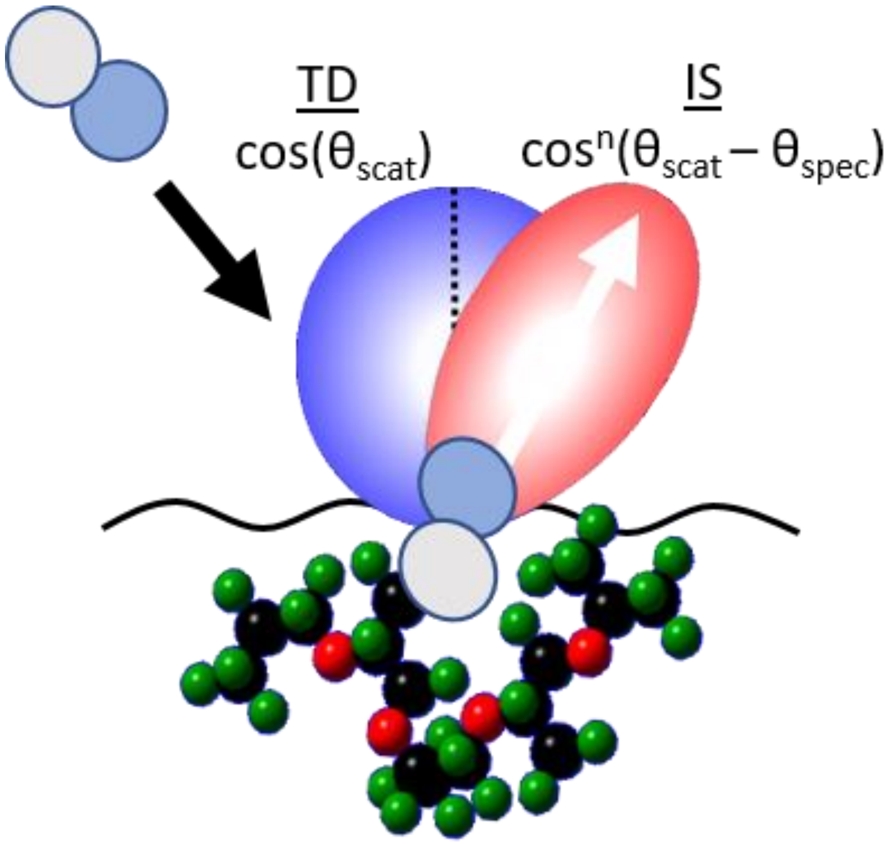

Fig. 4.1 A schematic of the TD/IS gas-liquid scattering paradigm.

essential physics. For example, pioneering work by Tully and coworkers on the IS pathway for gas-single crystal scattering has been based on an inertial ("hard cube") description of the local surface response.[15] Minton and coworkers extended these ideas into a simple but elegant kinematic collision model that succeeds in reproducing in-plane angular distributions for IS scattering based on the effective mass of such a cube.[16] One recurring conundrum, particularly evident for projectiles with internal (e.g., rotational/vibrational) degrees of freedom, is that the IS scattering distributions have often appeared hot but Boltzmann, i.e., well described by a hyperthermal IS "temperature," despite the absence of any reason why such a pathway should appear thermal. Fresh insight into this long-standing puzzle has been provided by recent work ("lever arm model") which reveals that averaging over the collision dynamics (e.g., capillary wave spatial fluctuations of the gas-liquid interface) can convert highly structured impulsive rainbow-like scattering distributions into a remarkably thermal-like distribution without invoking any equilibration.[17] However, no model has yet been forwarded that can predict these effective IS temperatures *a priori* and/or branching ratios (α) into IS/TD channels.

Thermal desorption, conceptually the simpler of the two IS/TD pathways, is the more universal process in gas-liquid scattering.[18] For gas-liquid systems studied with internal quantum state resolution, the standard paradigm has been that atoms/molecules undergo complete TD scattering behavior ($\alpha \approx 1$) at low collision energies ($E_{inc} \sim kT_S$) with finite branching ratios ($\alpha < 1$) into IS vs. TD pathways appearing only at hyperthermal energies.[5] As one of many systems, CO_2 gas-liquid scattering has been studied with full rovibrational quantum state and Doppler velocity resolution,[1] which for multiple liquids, surface temperatures, and incident angles demonstrate pure TD ($\alpha \approx 1$) at low collision energies and mixed TD/IS behavior ($\alpha < 1$) only at higher energies.[5,19] Indeed, it was largely based on this early work that such "dual temperature" models ($T_{TD} \approx T_S$, with T_{IS} treated as an empirical parameter) were originally postulated for molecular systems probed with both internal and external degrees of freedom.

The most robust empirical support for a dual temperature TD/IS pathway has been found in scattering studies with HCl/DCl. From time of flight studies by Nathanson and coworkers in the forward scattering direction, it was established that HCl/DCl undergo complete thermalization and $\cos(\theta)$ desorption from several liquid surfaces.[20-22] This was subsequently reinvestigated with both IR direct absorption and REMPI/VMI measurements, which confirmed that HCl/DCl at low energies equilibrates and undergoes thermal desorption in both external (translational) and internal (rotational) degrees of freedom ($T_{trans} \approx T_{rot} \approx T_S$).[17,23] The REMPI/VMI studies at higher collision energies took this one step farther and showed that, due to extreme glancing incident angles (75°), J state populations from both TD and IS pathways could be extracted by separate analysis of the *backward* and *forward* velocity components, respectively. This permitted a novel and completely independent test of the dual temperature TD/IS paradigm, demonstrating that the IS distributions still appear Boltzmann-like but with $T_{IS} >> T_{TD}$ and TD distributions with $T_{TD} \approx T_S$ Evidence for such thermal equilibration of the TD fraction to the surface temperature T_S has been seen in many other gas-liquid scattering experiments, for example, McKendrick, Minton, and coworkers report this for OH[24] + hydrocarbon surfaces and O_2 + Squalane.[16] The one notable exception for this paradigm has been NO,[25-27] which, at low collision energies, has been reported to scatter with rotational temperatures *colder* than the liquid surface. Specifically, T_{rot} was found to increase monotonically with surface temperature but with an incremental slope (dT_{rot}/dT_S) less than unity.[25-27] Sub-thermal behavior at low collision energies has been also seen in NO scattering from single-crystal metals and attributed to a combination of dynamical barriers and further rationalized by the complicated open shell rovibronic structure of NO.[28-30] Work by Polanyi et al., however, has shown that even the related closed shell CO exhibits a lack of equilibration with respect to T_S in scattering from single-crystal LiF (001).[31] Based on these results, one might therefore anticipate similar anomalies in low energy CO scattering of supersonic beams from gas-liquid interfaces.

In this paper, we explore the concept of thermal desorption in scattering experiments through both low energy quantum state resolved scattering and molecular dynamics studies. The paper is organized as follows. First, we describe the experimental methodology in Sec 4.2, followed in Sec. 4.3 by low energy scattering results as a function of liquid type (perfluorinated polyethers (PFPE), non-polar hydrocarbons, and polar glycerol) and liquid surface temperature (T_S = 253-303 K), for each of which the final quantum state distributions are notably *cooler* than T_S. To help interpret these experimental results, we present molecular dynamics calculations in Sec.

4.4, based on atom-atom intermolecular potentials for CO, DCl and CO_2 colliding with a fluorinated self-assembled monolayer surface (FSAMs), which prove to be in remarkably quantitative agreement with experiment. We exploit these simulations to examine projectile dependent interaction times at the gas-liquid interface and extend the MD results over a larger temperature footprint (T_S = 50 - 450 K), to elucidate the T_S-dependence on the collision dynamics. Finally, a discussion of possible reasons for this "sub-thermal impulsive scattering" (STIS) behavior for CO vs HCl, CO_2 is presented in Sec. 4.5, with conclusions summarized in Sec. 4.6.

4.2 Experimental

A detailed overview of the experimental apparatus has been presented elsewhere and thus only essential details and modifications for the current studies need be described.[5,17,32] This experiment consists of three key components: i) a temperature-stabilized liquid scattering target, ii) a supersonic molecular beam, and iii) a narrow linewidth, shot noise limited infrared absorption spectrometer. The temperature-stabilized scattering target is a modified version of the "lazy Susan" apparatus described in previous studies.[32] The liquid surface is prepared according to the method of Lednovich and Fenn,[18] using a rotating (~ 0.2 Hz) wheel (12.7 cm diameter) half-submerged in the liquid reservoir and scraped with a stationary razor blade to present a thin (~500 um), freshly prepared gas-liquid surface to the impinging molecular beam. To facilitate the temperature-dependent studies, we have replaced the Teflon liquid reservoir with a copper reservoir and the glass wheel by a bead-blasted stainless steel wheel to promote adhesion, with the liquid interfacial temperature-stabilized by a two-stage thermoelectric cooling system. A recirculating ethanol chiller (Lauda K-4/R) is used to regulate the temperature of a cold plate in the vacuum chamber from $-T_S \approx 20C$ to 30C. (Companies are named in the interest of completeness and not intended as commercial product support.) One side of this plate is attached to the lazy Susan apparatus and the other side to a thermoelectric cooler (TEC) attached to the fluid-filled copper reservoir. A thermistor attached directly to the copper vessel permits the TEC to servo-loop stabilize the reservoir to a primary target T_{res}, with the wheel temperature maintained within 1^{o} C of the desired setpoint. This reduces temperature gradients across all elements in thermal contact with the scattering fluid, which strengthens confidence that the liquid wheel surface is maintained at a well-determined temperature limited by thermistor uncertainty (± 0.5 K).

These studies involve three different classes of liquids that sample different scattering dynamical regimes: 1) perfluorinated polyether, (PFPE, Krytox 1506, $F\text{-}[CF(CF_3)CF_2O)]_{14(avg)}\text{-}CF_2CF_3$), as a rough but chemically inert liquid surface, 2) squalane (2,6,10,15,19,23-hexamethyltetracosane, $C_{30}H_{62}$), as a strongly hydrophobic surface, and 3) glycerol (1,2,3-propanetriol, $C_3H_8O_3$), as a strongly hydrophilic surface due to multiple protruding OH groups.[33] Each liquid is degassed under ~1 mTorr vacuum (1 Torr = 133 Pascal) at room temperature for several hours to remove dissolved gases (H_2O, O_2, N_2, CO_2), or at slightly elevated temperatures (~ 350 K) for the glycerol liquid samples to allow for more complete degassing within a reasonable time frame.

A low collision energy molecular beam is generated through a Proch and Trickl[34] style pinhole valve, with 5% CO in Argon expanded through a 500 um diameter pinhole at 100 Torr backing pressure. These low stagnation pressures are chosen intentionally to maximize CO signals while minimizing Ar-CO clustering in the incident beam. This 5% beam composition leads to an on-axis mean velocity of 550(30) m/sec measured with a time of flight microphone setup[35] yielding an average beam energy of $E_{inc} = 1.0(1)$ kcal/mol. The resulting molecular beam is collimated with a 3 mm diameter skimmer (Beam Dynamics) 2.25 cm from the pinhole orifice for a HWHM beam divergence of $\theta \approx 3.82^o$, with rotational temperatures of ∼10(2) K measured along the beam expansion axis using the infrared spectrometer described below. The pulse valve is aligned so the center of the molecular beam strikes the surface at $\theta_{inc} \approx -65^o$ away from normal incidence, with this highly glancing incident angle geometry chosen to maximize positively scattered CO absorption signals ($\theta > 0$) while minimizing CO(low J) contamination from the incident beam. Signals are collected in an angular wedge from $\theta \approx -40^o$ to 75^o, with the peak collection efficiency around the specular direction ($\theta_{spec} \approx +65\ ^o$) and 2/3 of the collected molecules coming from greater than $45\ ^o$. For rotational states $J \geq 5$ ($E_{rot} \geq 60$ cm^{-1}), the CO background ($A_{background} \sim 3 \times 10^{-5}$) due to incident beam contamination are an order of magnitude smaller than typical peak absorbance signals ($A > 4 \times 10^{-4}$) due to scattering.

The scattered populations are measured with a tunable laser direct absorption spectrometer operating near the quantum shot-noise limit. This spectrometer consists of i) a narrow linewidth external cavity quantum cascade laser (ECQCL, Daylight Solutions, 21047-MHF-013-D0724)[36], ii) frequency calibration/diagnostics, and iii) an *in vacuo* multipass cell with quantum shot-noise limited balanced detection. The ECQCL provides CW output greater than 250 mW over a frequency range of 1960 to 2200 cm $^{-1}$ with an optical linewidth $\Delta\nu < 10$ MHz in the experimental detection bandwidth (10 KHz). The laser frequency is calibrated with the combination of a fixed Fabry Perot etalon (FSR = 249.566(33) MHz) and a 5 cm gas transmission cell (500 mTorr of CO), which allows for both absolute (~5 MHz) and relative (~100 ppm) frequency diagnostics. The IR laser beam makes 16 passes through the scattering region in the vacuum chamber, with the light detected on two balanced InSb photodiodes (one before/after the multipass cell) in a fast servo subtraction circuit, removing common-mode technical noise down to the quantum shot-noise limit.

The net absorption sensitivity of the system is approximately 7 x 10^{-8} per $Hz^{1/2}$, which translates into a CO number density detection sensitivity of order 3 x 10^{8} #/cm^{3}/quantum state.

4.3 Experimental Results and Analysis

CO scattering from a series of liquids has been performed as a function of liquid surface temperature (T_S) to characterize the scattering pathways under low energy collision conditions (E_{inc} = 1.0(1) kcal/mol). The absorption signals reflect column integrated densities ($\rho_{v,J}$) which cannot be deconvolved into fluxes without prior knowledge of the coupled angular/speed scattering distribution ($f(v,\theta,\phi)$).[5,17] We can, however, express the experimental absorbance at a given Doppler detuning ($\nu_{Doppler}$) as the double integral

$$A(v, J, \nu_{Doppler}) = \int d\nu' \int dl[\rho_{v,J}(l,\nu')\sigma(\nu_{Doppler}-\nu')] \qquad \text{Eq. 1}$$

where $\rho_{v,J}(l,\nu')$ is the quantum state resolved density of absorbers at position l along the absorption path and $\sigma(\nu_{Doppler}-\nu')$ is the homogeneous absorption cross section per molecule (cm^2/#). Since $\sigma(\nu_{Doppler}-\nu')$ is much narrower than the Doppler widths, the integral over ν' can be performed to yield

$$A(v, J, \nu_{Doppler}) = S_{0J',v',J,v} \int dl\, \rho_{v,J}(l,\nu_{Doppler}) = S_{0J',v',J,v}\, P_{scatter}\, \rho_{CID} \qquad \text{Eq. 2}$$

where S_0 is the integrated absorption cross section (cm^2cm^{-1}/#) for the $v' \leftarrow v$, $J' \leftarrow J$ rovibrational transition, ρ_{CID} is the column integrated density (#/cm^2), and $P_{scatter}$ is the total probability of scattering into the v, J quantum state. The experimental absorption profiles are therefore a function of three variables, J, v and $v_{Doppler}$, where $v_{Doppler}$ is the velocity component along the laser beam axis and probed by Doppler tuning over the rovibrational transition. The laser beam is perpendicular to both the liquid surface normal and molecular beam. The Doppler velocity measured is the velocity perpendicular to the scattering plane created by the surface and the molecular beam, which will be refer to as the out-of-plane velocity/speed. At low incident energies, the expectation is that the CO projectile traps in the surface van der Waals well, undergoes many "memory destroying" collisional interactions, and then desorbs with its internal (rotational) and external (translational) degrees of freedom in equilibrium with the surface temperature ($T_{rot} \approx T_{trans} \approx T_S$). In our model, the scattering probability ($P_{scatter}$) is expressed as a product of an out-of-plane ($v_y = v_{Doppler}$) Maxwell-Boltzmann (MB) distribution times a thermalized rotational distribution:

$$P_{scatter}\,(J, v_{Doppler}) = P_{MB}(v_{Doppler}, T_{trans})\, P_{rot}(J, T_{rot}) \qquad \text{Eq. 3}$$

which allows us to characterize independent transverse Doppler and rotational distributions by different temperatures ($T_{trans} \neq T_{rot}$). If these two temperatures are both experimentally indistinguishable from the surface temperature ($T_{trans} \approx T_{rot} \approx T_S$), detailed balance considerations[7] imply that the incident CO undergoes complete thermalization and desorbs without any barrier restricting the exit channel dynamics.

However, this is decidedly *not* what is observed, as evident in Fig. 4.2A from a Boltzmann plot of the rotational state populations for CO scattering from PFPE at room

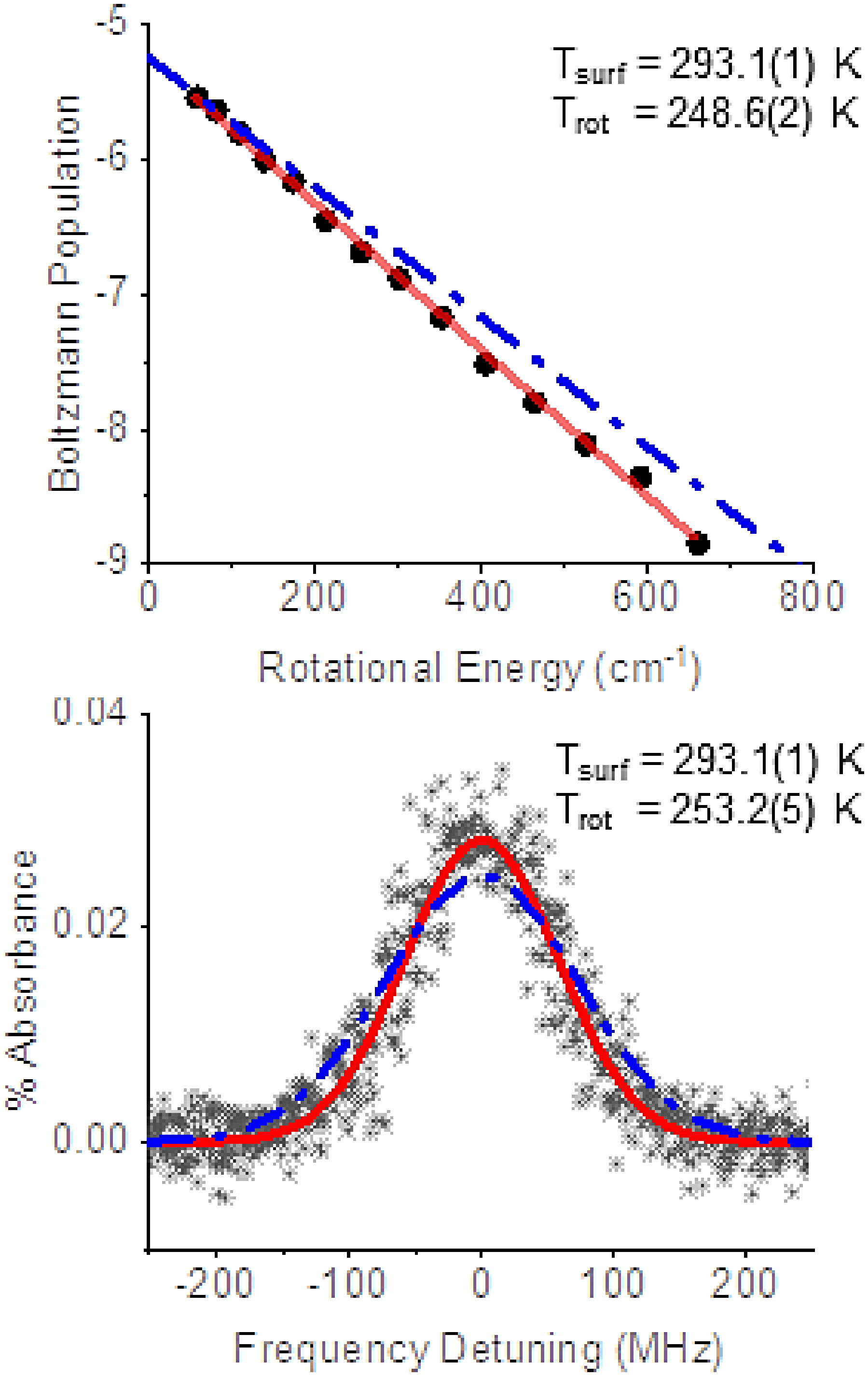

Fig. 4.2 Sample data for CO scattering from room temperature squalane at E_{inc} = 1.0 kcal/mol. A) Boltzmann plot of the rotational states. The blue dot-dash line represent a room temperature rotational distribution while the red solid line is the fit that predict subthermal behavior. Rotational states 5 through 18 are plotted. B) Same as in A) but for the translational degree of freedom for J =8.

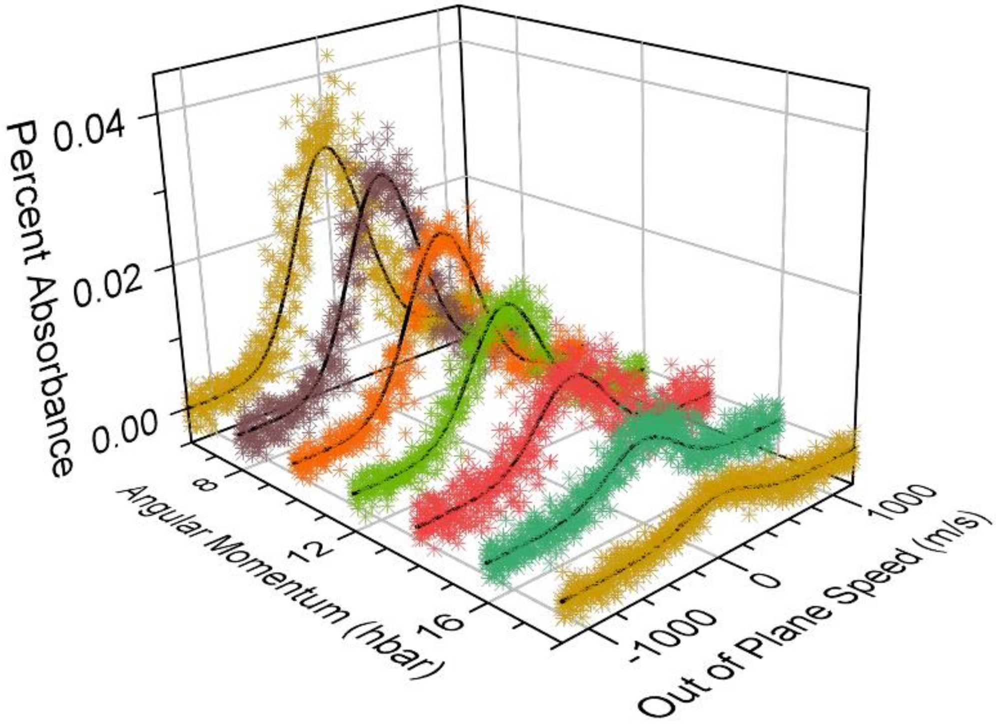

Fig. 4.3 Sample least squares fits (black line) to high resolution CO(J) Doppler velocity profiles obtained from scattering of CO + squalane at room temperature. To avoid visual congestion, only the odd rotational states from J = 5 -17 are shown out of the total J < 20 states detected.

temperature. Instead, the CO rotational distributions exhibit thermal Boltzmann-like behavior but with a “temperature” (solid red line) that is significantly colder ($\Delta T \approx$ -45(3) K) than the surface (T_S = 293.1(1) K, blue dashed line). This absence of complete equilibration with the surface is further corroborated by high-resolution Doppler profile data in Fig. 4.2B, for which distinctly sub-thermal scattering “temperatures” are also noted in least squares Gaussian fits to the out-of-plane velocity distributions, with comparison of the model fit with sample data summarized in Fig. 4.3. Also worth noting is that, although both the translational and rotational “temperatures” are clearly out of equilibrium with the liquid, they are indistinguishable from each other within experimental uncertainty ($T_{rot} \approx T_{trans} < T_S$). Thus, one simple physical picture for such behavior would be that the CO has enough interaction time with the liquid surface to equilibrate among its own internal/external (rotation/translation) degrees of freedom, but still not enough time to equilibrate completely with the surface itself. It is important to note that the translational "temperature" data in these studies probe only velocity components *perpendicular to the scattering plane*, with the corresponding *parallel velocity* components inaccessible to laser Dopplerimetry in the current experimental probe geometry.

We next explore the low energy CO gas-liquid scattering dynamics as a function of both i) the liquid and ii) the liquid temperature, with results summarized in Fig. 4.4. First of all, the data consistently indicate significant negative deviations ($\Delta T = T_{rot/trans} - T_S \approx -45(15)$ K) from full CO equilibration with the liquid surface, with both rotational and translational degrees of freedom indistinguishable and yet colder than T_S ($T_{trans} \approx T_{rot} < T_S$). Secondly, despite such deviations, there is nevertheless a clear sensitivity in the T_{rot} and T_{trans} values to the liquid temperature itself. Specifically, the $T_{trans} \approx T_{rot}$ values vary quasilinearly with changes in T_S, but with a subunity differential growth ($dT_{rot/trans}/dT_S \approx 0.50(8)$) over the range of experimentally accessible temperatures. Thirdly, such deviations from full T_D equilibrium behavior are only weakly dependent on the nature of the liquid, with a greater equilibration toward T_S demonstrated for soft hydrophobic hydrocarbon (squalane) vs. the more strongly interacting (glycerol or PFPE) gas-liquid interfaces. In summary, the rotational quantum state and Doppler resolved experimental data provide evidence for *non-equilibrium scattering dynamics* at the gas-liquid interface, even at low collision energies ($E_{inc} \approx kT_S$) for which conventional wisdom would predict complete trapping desorption (TD) equilibrium behavior. To help provide physical insight into such non-equilibrium behavior, we turn next to molecular dynamics simulations in Sec. 3,4, specifically attempting to

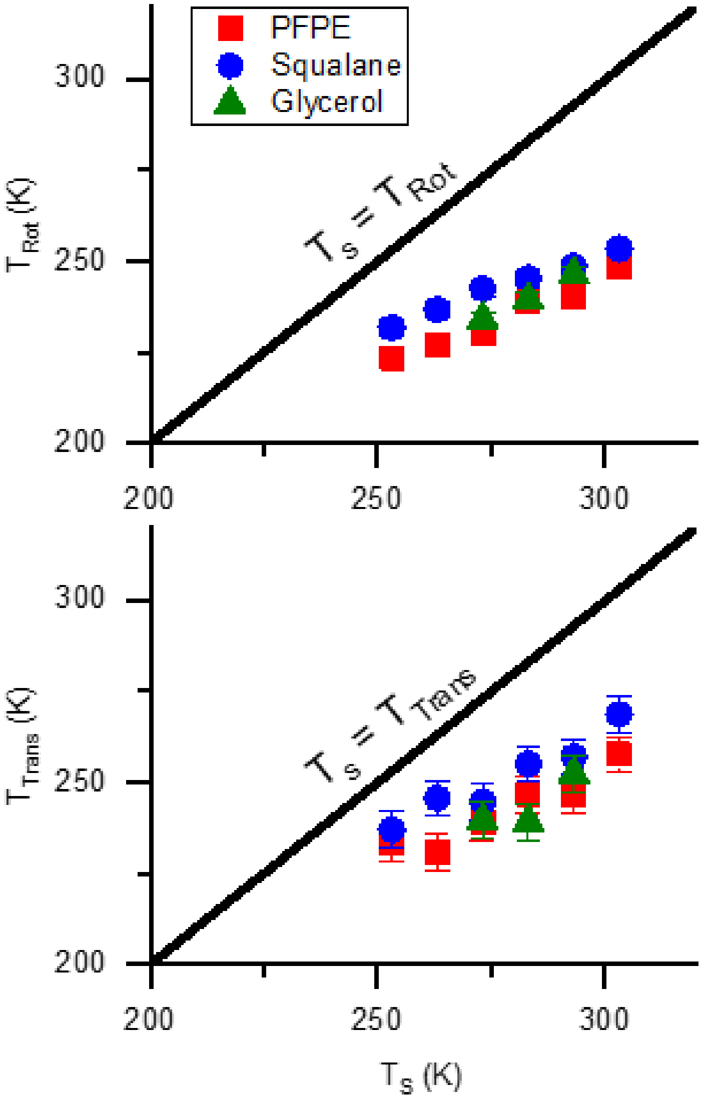

Fig. 4.4 Temperature dependence of low energy CO scattering for a series of liquids. The top panel shows the scattered rotational temperature (T_{rot}) as a function of T_S. The black line represents complete equilibration between rotational and surface temperatures. The bottom panel displays similar data and analysis with respect to the Doppler translational degree of freedom (T_{trans}). Error bars represent 1σ standard deviations of the mean. These measurements contain data from J=5-18

model low energy experimental scattering behavior for three projectiles (CO, DCl, CO_2) at a perfluorinated, hydrophobic, and hydrophilic gas-liquid interface.

4.4 Molecular Dynamics Simulations

In order to probe the nature of "TD" equilibration (or lack thereof) with the surface, three different molecular projectiles have been explored: CO_2, CO, and DCl/HCl. Experimentally, all three molecules have been extensively characterized in gas-liquid scattering studies at low collision energies. As mentioned in the introduction, CO_2 and DCl/HCl thermalize with the gas-liquid surface at low E_{inc} while the present results clearly demonstrates that CO does not. By comparing the trajectory results from these three projectiles, a mechanism for why CO (vs. DCl/HCl, CO_2) does not equilibrate and thermally desorb from the surface can be developed. To these ends, two series of molecular dynamics studies have been explored. The first series focuses on the temperature dependence (T_S) of CO surface scattering, which provides access to a much wider range of temperatures as well as permits direct comparison to experimental data. A second series looks at differences in scattering dynamics between the three probe molecules (non-polar (CO) vs. strongly dipolar (DCl) vs. quadrupolar CO_2 projectiles) with scattering from a model perfluorinated liquid interface.

4.4.1 CO, DCl, and CO_2 + FSAMs Potential Energy Surface

Molecular dynamics calculations from our group in collaboration with the Hase group have been previously described. [37] In the interest of simplicity, we direct these efforts first toward scattering of molecules from a perfluorinated interface, building on previous successes for theoretical modeling of quantum state resolved scattering. The simulated surface is a fluorinated self-assembled monolayer (FSAM), which has been shown to be an accurate yet computationally feasible proxy for the liquid, PFPE.[38,39] As implemented previously, a sample surface is constructed from 48 fluorinated thiol radicals, $CF_3(CF_2)_7S$, chemisorbed onto a slab of Au(111) by a harmonic Au–S stretch potential. This slab of gold atoms is fixed in space and used to define the surface and its unit cell. Motions for the other atoms in the chain are governed by additional potentials that involve two-atom stretches, three-atom bends, and four-atom torsions. Atoms in the chains interact with each other through atom-atom non-bonding potentials that are constructed from the sum of an exponential repulsion and C/r^n attraction term, with published parameters for each of these expressions.[37]

The CO_2-PFPE potential energy surface (PES) has been generated by Hase and coworkers and utilized extensively by Perkins et al. New surfaces for the CO and H/DCl gas-SAM potentials have been developed for the present study according to the same principles. Briefly, *ab initio* radial 1D scans have been calculated for both CO and HCl approaching CF_4 from a series of Euler approach (ϕ, θ, χ) angles, with the CF_4 molecule serving as proxy for a CF head group at the gas-polyfluorinated liquid (PFPE) interface. For each intermolecular geometry, high level ab initio calculations are performed with explicitly correlated (f12) electron methods at the CCSD(T)-f12 level of theory (MOLPRO software platform)[40] with f12 correlation consistent Dunning basis sets (AVnZ-f12; n=2,3,4), counterpoise correction for basis set superposition error (BSSE), and extrapolation to the complete basis set limit (CBS).[41-46] This set of ab initio energy values is then fit to a two-body atom-atom expression utilizing Lennard-Jones type exponential repulsion/inverse power law attraction/repulsion terms:

$$V_j(r_j) = \sum_i A_i e^{-k_i r_j} + \sum_i B_i r_j^{-n_i} \qquad \text{Eq. 4}$$

where r_j is the two-body spacing for the j^{th} pair of atoms. Such a PES construction protocol has been used in the generation of the corresponding potential for CO_2-FSAMs scattering dynamics, which demonstrates remarkably quantitative agreement with experiment.[39]

We note that such gas-SAMs PES data have distinct repulsive/attractive regions on very different energy/length scales. Thus, any non-weighted least squares fit over a uniform grid spacing will yield results sensitive to the *ad hoc* choice of grid range sampled, typically oversampling the repulsive hard wall (high E) and underweighting both the van der Waals well region and long range attractive parts (low E) of the potential. This is especially relevant for scattering at low incident energies, for which the trajectories do not sample high up on the repulsive wall. To counterbalance these effects, we implement a weighted least-square fit which more democratically samples the three dynamically relevant regions (repulsive wall, van der Waals well, and attractive long range) of the potential. The empirical weighting function used is of the form:

$$W(E_{inc}) = \left(E_{inc} + E_{off}\right)^{-2} \quad \text{Eq. 5}$$

with the offset energy ($E_{off} > 0$) chosen to prevent divergence at low E_{inc} and regulate how quickly the weights decrease with increasing energy. For a given CF_4 – molecular projectile combination, E_{off} is chosen empirically such that the weight at the bottom of the van der Waals well is approximately 16-fold larger than at $E_{inc} = 0$. By way of example, Fig. 4.5 displays sample cuts of the calculated and least squares fitted PES for both CF_4-CO and CF_4-H/DCl potentials at $E_{inc} < 3$ kcal, as well as insets showing this good agreement extending to higher incident energies. The optimized least squares fitted coefficients (A_i, k_i, B_i, n_i) for both CO-CF_4 and H/DCl-CF_4 potential energy surfaces are summarized in Tables 4.1&4.2. Within the context of the Born Oppenheimer approximation, the potentials are identical for both CF_4-HCl and CF_4-DCl.

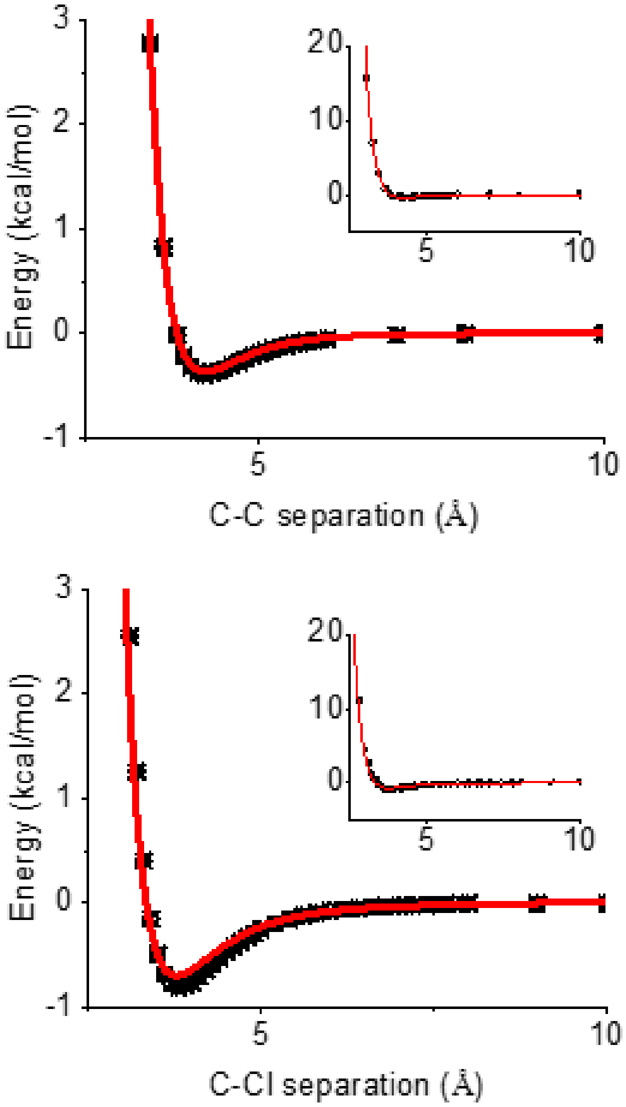

Fig. 4.5 Sample ab initio CCSD(T)-f12/AVnZ (n = 2,3,4 CBS) potential slices for OC-CF_4 (C-C distance, top) and DCl-CF_4 (C-Cl distance, bottom), with the analytic least squares atom-atom fit to the full potential energy surface (PES) shown in red. See text for details. The insets show the PES over a larger energy scale.

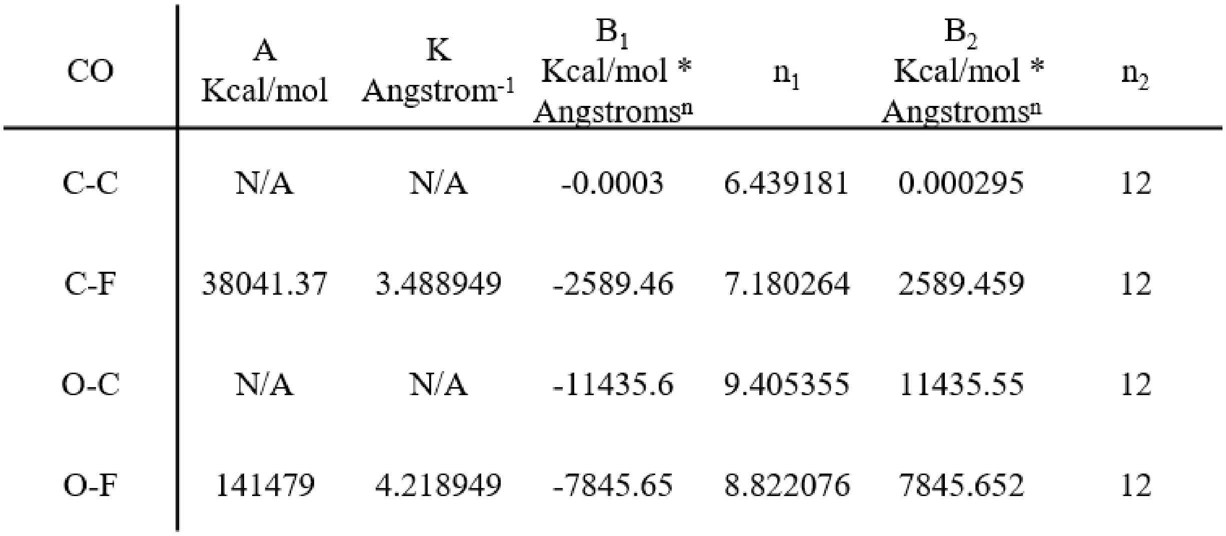

CO	A Kcal/mol	K Angstrom^{-1}	B_1 Kcal/mol * Angstroms^n	n_1	B_2 Kcal/mol * Angstroms^n	n_2
C-C	N/A	N/A	-0.0003	6.439181	0.000295	12
C-F	38041.37	3.488949	-2589.46	7.180264	2589.459	12
O-C	N/A	N/A	-11435.6	9.405355	11435.55	12
O-F	141479	4.218949	-7845.65	8.822076	7845.652	12

Table 4.1. Least squares fitted parameters for the CO-FSAMs atom-atom potential, as obtained from least squares fits to high level ab initio CCSD(T)-f12/AVnZ-f12 (n=2,3,4,CBS) calculations for a systematic series of CO approaches to CF_4. See text for details.

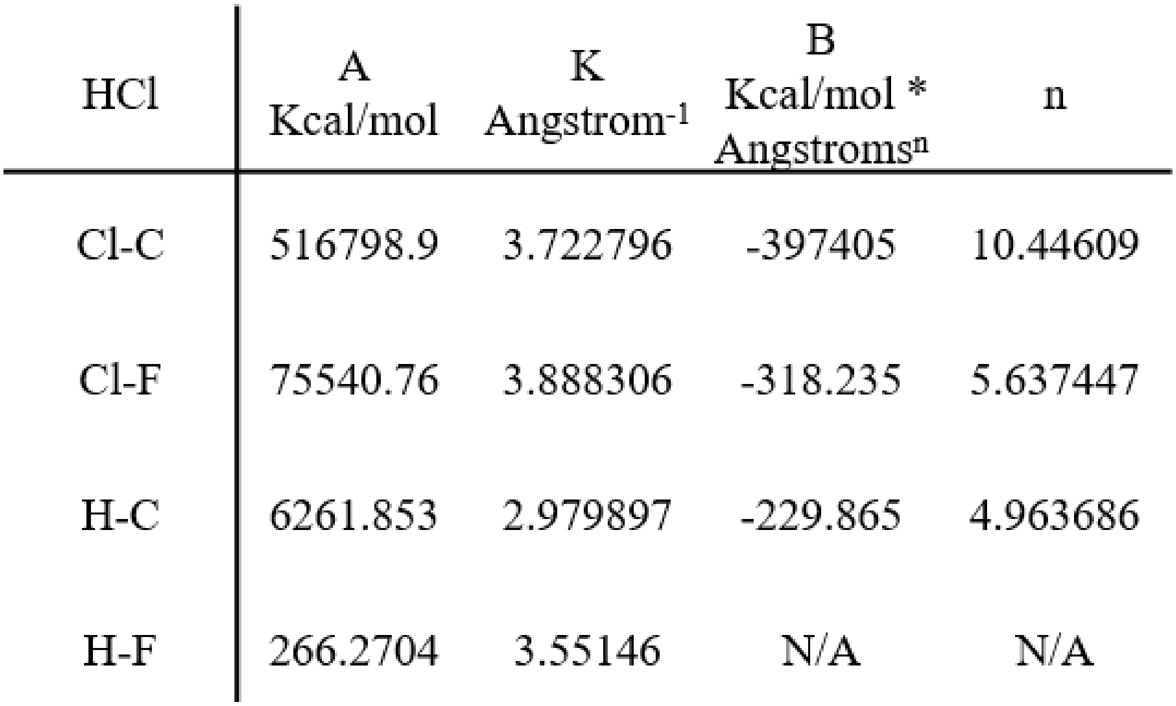

HCl	A Kcal/mol	K Angstrom^{-1}	B Kcal/mol * Angstroms^n	n
Cl-C	516798.9	3.722796	-397405	10.44609
Cl-F	75540.76	3.888306	-318.235	5.637447
H-C	6261.853	2.979897	-229.865	4.963686
H-F	266.2704	3.55146	N/A	N/A

Table 4.2. Least squares fitted parameters for the HCl-FSAMs atom-atom potential, as obtained from least squares fits to high level ab initio CCSD(T)-f12/AVnZ-f12 (n=2,3,4,CBS) basis set superposition error (BSSE) corrected calculations for a systematic series of HCl approaches to CF_4. See text for details.

The CO_2 Van der Waals complex has been discussed in great detail by Hase and coworkers. The lowest energy configuration for this complex is C_{2v} symmetry with the carbon from the CO_2 approaching between two of the fluorine's with a carbon-carbon distance of 3.76 angstroms and a well depth of -.82 kcal/mol. For H/DCl, the bound state has was not captured along the trajectories calculated. The lowest energy configuration calculated is with the chlorine centered between three of the CF_4's fluorines with the hydrogen pointing perpendicular to this axis eclipsing the a fluorine when looking down the symmetry axis, with a carbon-chlorine distance of 3.8 angstroms and a depth of -.83 kcals/mol. Naively, we thought the bound state would be of C3v symmetry with the hydrogen pointing towards the central carbon but due to the large polarizability of the chlorine and the large size of the fluorines, the hydrogen is pushed out of the way leading to a bound state of Cs symmetry. The final molecule, CO, is quite interesting since it has two near identical wells. The lower energy configuration is where the carbon of the CO is facing the carbon of the CF_4 with a carbon-carbon distance of 3.65 angstroms and a well depth of -.667 kcals/mol. The other bound well is with the oxygen of the CO facing the CF_4's central carbon. This has a carbon-carbon distance of 4.55 angstroms (with a carbon-oxygen distance of 3.42 angstroms) and a well depth of -.665 kcals/mol.

4.4.2 Trajectories: Low Energy Collisions of CO, DCl, CO_2 with FSAMs

Scattering trajectories are calculated using the package VENUS05 developed by Hase and coworkers,[47] propagated with sufficiently small timesteps ($\Delta t \approx 0.2$ fs) to ensure energy conservation ($\Delta E/E < 50 \times 10^{-9}$) over the time scale of a typical 10,000 fs trajectory. To permit temperature control of the gas-liquid interface, each trajectory is initiated with FSAM momenta sampled from a Boltzmann distribution at T_S. The FSAM simulation is then propagated for 2000 fs, with the atomic velocities uniformly rescaled after every 100 fs to equilibrate the atom ensemble to a well-defined temperature and average kinetic energy (i.e., $<E> = 3/2kT_S$). The CO, DCl, and CO_2 projectiles are prepared asymptotically (z_{init} = 30 Å from the surface) in an initial state corresponding to uniform 2D angular sampling of the molecular orientation and zero rotational energy (J = 0). The total incident linear momentum of the projectile is kept constant from trajectory to trajectory, with the first point of contact randomized by 2D translation over an area equivalent to a single FSAM unit cell. The trajectory is then propagated such that the projectile collides with and rebounds sufficiently far from the surface for any residual projectile-surface interaction to be negligible, either by final height ($z_{final} > z_{init} = 30$ Å) or total time interval ($T_{final} > 100,000$ fs). The final projectile velocity components and kinetic energies are taken directly from the last simulation point, for which the angular momentum J is sorted into bins of ħ width from the final simulation value of $<J^2> \approx J(J+1)\hbar^2$.

4.4.2 Theoretical Results and Analysis: CO with FSAMs

We are now in a position to analyze the molecular dynamics (MD) trajectories on the same footing as the original quantum state resolved experimental data. The first and simplest comparison to make is between experimental and theoretical "temperatures" for low energy (E_{inc} = 1.0(1) kcal/mol) scattering of CO molecules from liquid PFPE (experiment, Fig 4.4, red symbols)) and FSAMs (MD simulation, Fig. 4.6, black symbols). To extract a temperature (T_{rot}) from the rotational degree of freedom, we least squares fit the final CO(J) states to a single temperature Boltzmann distribution, a sample log plot of which for CO scattering from FSAMs is reported (T_S = 350 K) in the upper right panel of Fig. 4.6. Noteworthy is the remarkable agreement between the *experimental* T_{rot} values extracted from CO scattering data (as summarized in Fig. 4.4) with the

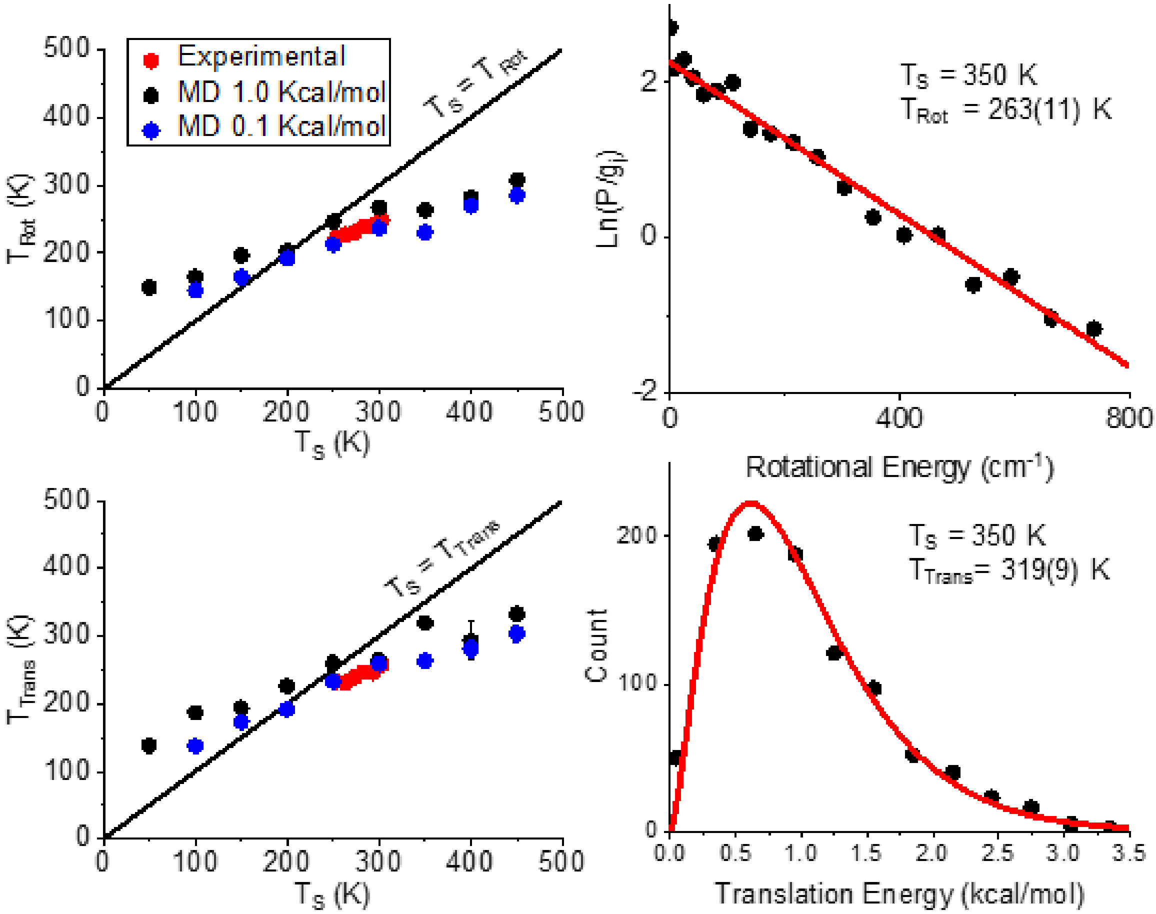

Fig. 4.6 Comparison of MD and experimental temperature dependence. The left panels show the rotational (top) and translational (bottom) temperature dependence. The right panels show example fits to the MD data at a surface temperature of 350 K. Both the black and the blue data points are simulated data while the red data points are experimental.

theoretical T_{rot} values in Fig. 4.6A obtained from analysis of the low energy MD trajectory data, although now accessible over a much broader dynamic range ($T_S \approx$ 50-450K vs. $T_S \approx$ 275-325K). Also worth noting is that such good agreement between experiment and theory is largely insensitive to incident energy, with MD trajectory data at an order of magnitude lower $E_{inc} \approx 0.1$ kcal/mol yielding only slightly cooler (blue symbols, Fig. 4.6A) but essentially indistinguishable results from the $E_{inc} \approx 1.0(1)$ kcal/mol scattering data (black symbols, Fig. 4.6A). Furthermore, the theoretical T_{rot} data exhibit the same *quasilinear incremental* dependence on FSAM temperature. Specifically, differential slopes ($m \approx dT_{rot}/dT_S \approx 0.42(3)$) from the MD simulations are in reasonable agreement with the values ($m \approx dT_{rot}/dT_S \approx 0.49(5)$) determined experimentally for CO + PFPE (see Fig. 4.4). Simply summarized, the CO(J) distributions for low energy collisions ($E_{inc} \approx 1.0$ kcal/mol) at the gas-PFPE liquid interface scatter with a rotational temperature *colder than* ($\Delta T \approx -53$K at $T_S = 300$K) and differential slopes ($m \approx 0.49(5)$) indicating sensitivity to the surface temperature (T_S). These trends are in close agreement with theoretical trajectory data for CO + FSAMs over a much wider temperature window (see Fig. 4.6A) than is experimentally accessible in the liquid phase.

In a similar fashion, we next analyze the trajectory calculations for *translational* distributions in the scattered CO flux at low incident energies. We find that fits to a normal flux weighted probability distribution ($F(v_x,v_y, v_z) \propto v_z \exp(-m(v_x^2+v_y^2+v_z^2)/2kT_{trans})$ and temperature (T_{trans}) already yield satisfactory agreement with the data. We thus report global fits to a single translational temperature (Fig. 4.6, lower left panel), which yield statistics with low scatter for the full set of N = 1000 trajectories (see Fig. 4.6B right panel for a sample speed distribution) than each degree of freedom fit independently. The MD scattering data for CO + FSAMs again yield translational temperatures varying linearly with T_S and in remarkably good agreement with the experimental CO + PFPE results. Analysis of the translational data provides additional experimental/theoretical support for CO scattering from a FSAMs surface in a temperature distribution that is both i) *colder* than ($\Delta T \approx -45(15)$K) and ii) differentially proportional to ($dT_{trans}/dT_S \approx m \approx 0.50(8)$) the liquid temperature over our experimentally accessible window of observation. The combined experimental and theoretical results for CO are in fundamental disagreement with a conventional picture of 100% trapping desorption (TD) dynamics dominating at low collision energies, which in the absence of transition state barrier would predict complete equilibration ($T_{rot} \approx T_{trans} \approx T_S$) with the liquid surface temperature at all values of T_S.

The trajectory data obtained over this more expanded temperature range in Fig 4.5 reveal additional insight into the scattering dynamics. Specifically, the theoretical plots for $E_{inc} \approx 1.0(1)$ kcal/mol intersect the $T = T_S$ line, and are therefore predicted to cross from a regime of *sub-thermal* scattering ($T < T_S$) at near room temperatures into a nominally "*hyperthermal*" scattering regime ($T > T_S$) at sufficiently low surface temperatures. Indeed, this stimulated a parallel set of trajectory studies at 10-fold lower collision energies ($E_{inc} = 0.1$ kcal/mol, see Fig. 4.5), which clearly reiterate the same sub-thermal to hyperthermal crossover near $T_S \approx 200$K. This non-physical result is inconsistent with full TD equilibrium predictions, for which one would expect T_{rot}, T_{trans} *to asymptotically approach but never cross* T_S. This provides first unambiguous evidence that the energy transfer dynamics are still far from the TD scattering regime even down at $E_{inc} = 0.1 – 1.0$ kcal/mol. Instead, with CO–FSAMs well depths of ≈ 0.5 kcal/mol, these collision dynamics sample an incident energy window competitive with long range interactions between the projectile and the liquid surface atoms. One final note on the MD simulations at .1 kcal/mol, the point at $T_s = 50$ K was run but none of the trajectories finished within the 100 ps window. This could be indicative that the sticking coefficient goes to 1 around this surface temperature and collision energy for CO.

4.4.4 Theoretical Results and Analysis: DCl and CO_2 with FSAMs

Although the MD results empirically match experimental observations quite well, they do not yet provide an answer why CO molecules desorb from the surface at temperatures below T_S.

To achieve a further insight, we have extended these MD simulations to all three projectiles (CO, DCl and CO_2) colliding with a FSAM model surface, each of which have been experimentally studied with PFPE liquid in quantum state resolved experiments. These three molecules are quite different in terms of their interactions with surface CF bonds, corresponding to van der Waals dipole induced dipole (CO-CF), dipole-dipole (D/HCl-CF)[48] vs dipole-quadrupole (OCO-CF)[49]. Since DCl and CO_2 have been shown to experimentally equilibrate with PFPE at low collision energies, we thus anticipate nearly full thermalization in the MD simulations to $T_S \approx 300K$.

The final quantum state populations from these additional molecular trajectories are analyzed in identical fashion to the previous CO + FSAM data in Sec. IVB, with $T_S = 300K$. As expected, CO_2 and DCl do scatter from FSAM with near thermal rotational temperatures, specifically $T_{rot} \approx 305(10)$ K and $T_{rot} \approx 287(12)$ K, respectively. Similarly, we also observe fully equilibrated results in the DCl and CO_2 translational degrees of freedom, with temperatures from least squares fits to out-of-plane velocity profiles of $T_{trans}(DCl) = 309(7)$ K and $T_{trans}(CO_2) = 304(7)$ K. This is in clear contrast with the CO trajectory behavior, which consistently scatters from an FSAM interface ($T_S = 300$) with *sub thermal* rotational ($T_{rot} = 266(9)$ K) and translational ($T_{trans} = 264(6)$ K) temperatures. In summary, the MD theoretical predictions for each of these three projectile + gas-liquid interfacial trajectory simulations match closely what has been experimentally observed from actual quantum state resolved scattering studies.

4.4.5 Interaction Time Analysis: CO, DCl, CO_2 with FSAMs

The excellent agreement between MD simulations and experimental results motivates a deeper statistical analysis into the trajectories themselves. One crucial observable is the interaction time (τ) of the molecule on the surface, which can be determined from durations over which the gas-surface forces exceed some threshold. This threshold is chosen to be 10x the root mean square force magnitude (f_{RMS}) over the first 3 ps of the simulation, during which the molecule is 30 angstroms away from and does not interact appreciably with the surface. This gives us the level of the machine precision noise (the noise floor), and when the force exceeds that, the molecule is detectably interacting with the surface. The level chosen is high enough to be clear of machine precision noise but is low enough that every molecule only crossed this level twice, once when it starts to interact with the surface and once when it leaves the surface. If the desorption were a 1st order kinetic process, we would expect the gas-liquid collisional durations to be exponentially distributed, with a slope reflecting the lifetime of the molecule-surface complex. The level chosen above is ~ 1 nm above the surface and thus there will be a contribution to this extracted value from the flight time of the leaving molecules. This, however, is ~1-3 picoseconds on average and thus does not appreciable change the extracted lifetimes.

Semilinear plots of the corresponding exponential decays are exhibited in Fig. 4.7, along with linear least squares fits to extract the corresponding projectile-surface residence lifetimes. As expected, the residence times on this surface are indeed well characterized by single exponential decay, with lifetimes on the 10-30 ps range. Interestingly, there is a clear 2-3 fold *increase* in surface residence lifetimes for the *more strongly* (τ_{CO2} = 28(1) ps and τ_{DCl} = 19(1) ps) vs. *less strongly* (τ_{CO} = 9(1) ps) interacting projectiles. Only a very small fraction of events are observed with lifetimes in excess of the maximum cutoff trajectory duration (t_{cutoff} = 100 ps), specifically, 0%, 1% and 5% for CO, DCl, and CO_2 respectively. As expected, this is in the same order as the

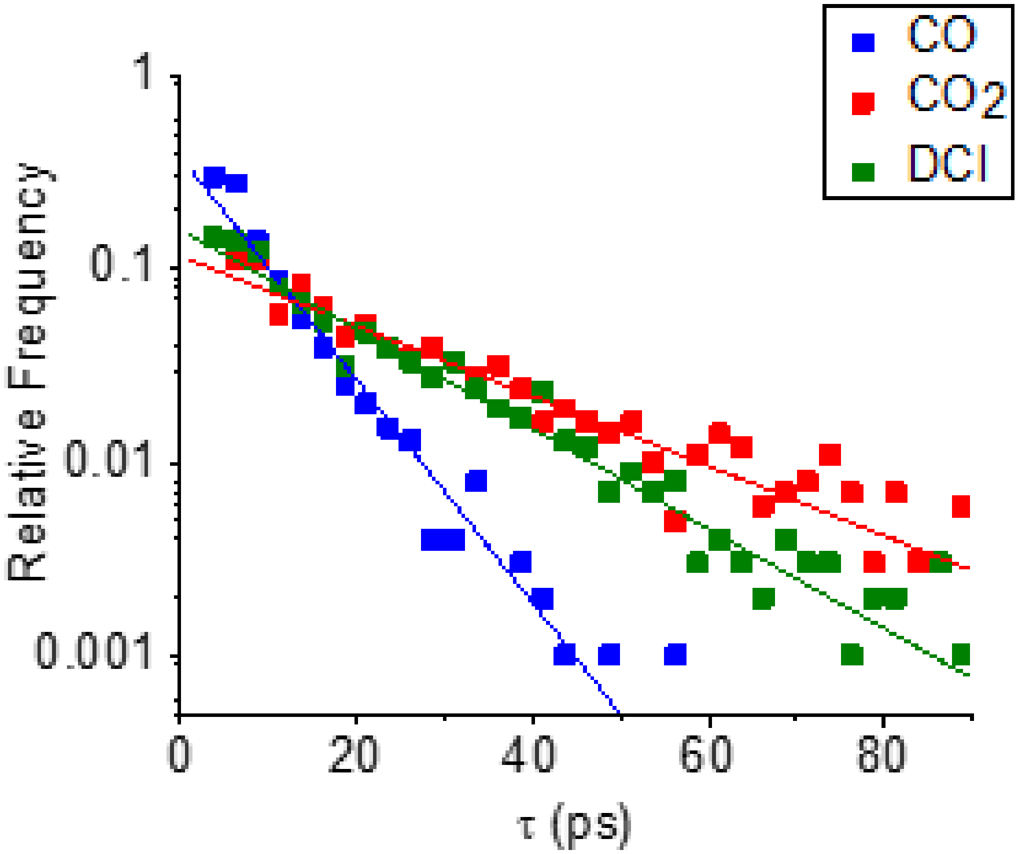

Fig. 4.7 Histograms of surface FSAM interaction times in MD simulations for low energy scattering with each of the three projectiles. The fractions of trajectories that do not result in escape from the surface after 100 ps trajectories for CO_2, DCl, and CO are 5%, 1% and 0%, respectively.

1/e lifetimes of collisional durations, and in reverse order with respect to potential well depths for the gas-liquid binding interactions (see Fig. 4.5). Similarly, instead of looking at the length of time the molecule interacts with the surface, we can look at the number of classical turning points the molecule undergoes during its trajectory. This reports on the number of times the normal momentum reverses and thus can be seen to be approximately twice the number of times the molecule attempts to leave the surface. For the three scatterers, we see a similar trend to the surface residence times. CO undergoes an average of ~6 classical turning points meaning that it on average takes only three attempts to leave the surface before it is successful. This is in contrast to the two other molecules with DCl undergoing ~19 classical turning points and CO_2 undergoing ~35. Thus, it can be seen that it requires many fewer attempts for CO to leave the surface than the other two molecules.

An even more insightful metric can be obtained from the distribution of gas-liquid surface heights P(z) over a full time dependent scattering trajectory. This is extracted by sampling the center of mass for each projectile (CO, DCl, CO_2) every 2 fs (10 time steps) and recording the height (z) above the gas-liquid interface. The three sets of data from all N = 1000 trajectories are then histogrammed ($\Delta z = 0.1$ Å bins), normalized to unit incident flux, and displayed on the same scale in Fig. 4.8. The surface height (z=0) was determined by looking at the distribution of the surface fluorines and finding their time averaged 50% density position above the Au surface, from

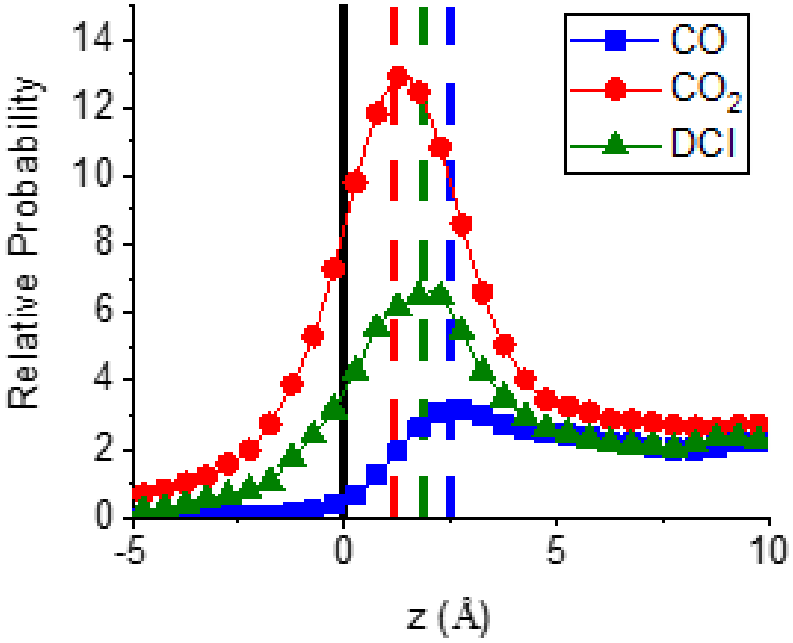

Fig. 4.8 The probability distribution of the three molecules probed as a function of height above the surface. The dotted lines show each of the peaks of the distributions in relation to the surface height at z = 0 (black line).

which the whole surface is anchored. The resulting plots exhibit a qualitatively similar topology for each projectile, with i) a flat asymptotic approach probability ($z > 5$ Å), ii) strong peaking in the adsorption well region (0 Å $< z < 5$ Å), and iii) rapid probability decay as the projectile penetrates into the FSAM surface. However, there are also important differences between the plots for CO vs. DCl/CO_2 projectiles, which in turn inform critical differences in the collision dynamics. For example, CO exhibits a much weaker statistical presence in the well region, with a maximum relative probability density ($P_{well} \sim 1.7$) two to three-fold smaller than for DCl ($P_{well} \sim 3.3$) or CO_2 ($P_{well} \sim 5.5$). As expected for a 1st order exponential process, these values are in excellent agreement with ratios of observed residence lifetimes (see Fig. 4.7). Furthermore, if we look more closely at the well region, the CO probability density peaks at $z_{max} \sim 2.50(10)$ Å from the surface while the maxima for DCl and CO_2 occur at ~2.00(10) and ~1.25(10) Å respectively. Simply summarized, histogram analysis of the trajectories indicates that CO is i) trapped substantially more shallowly than DCl or CO_2 and ii) spends more of its residence time further away from the FSAMs surface.

Finally, an even subtler but more quantitative tool with which to represent such statistical data is the potential of mean force (POMF), represented by

$$V_{POMF}(z) = -kT_B \ln[P(z)] \qquad \text{Eq. 6}$$

Under *equilibrium conditions*, V_{POMF} characterizes the relative probability for a projectile a distance z above the gas-liquid interface in terms of a distance dependent free energy, i.e., $\Delta G(z) \sim V_{POMF}(z)$. However, it provides an equally meaningful probability distribution *under non-equilibrium conditions*, as obtained from calculations of the force normal to the surface for each of the bin heights and integrating the reversible work from infinity back to the gas-liquid interface. The values of this *non-equilibrium potential of mean force* ($V_{POMF}(z)$) have been calculated from the trajectories (Fig. 4.8) and are plotted in Fig. 4.9. As noted previously for the surface height distributions (Fig 4.8), there are three characteristic domains labelled as i) asymptotic, ii) van der Waals well, and iii) repulsive wall regions, where we have chosen z = 0 as the point at which the average fluorine density has decayed to 50% of its bulk value. Of particular importance, both CO_2 and DCl projectiles exhibit minima penetrating into the liquid ($z < 0$), whereas the well for CO is more nearly centered on the gas-liquid interface itself. Profound differences can be seen in the V_{POMF} well depths for these three projectiles, with the CO POMF well depth (0.3 kcal/mol) *3-4 times shallower* than either DCl (0.8 kcal/mol) or CO_2 (1.1 kcal/mol). Additionally, V_{POMF} for CO in the repulsive region (left side of Fig.4.9) increases with a slope of $m \approx 0.6$ kcal/mol/Å, while

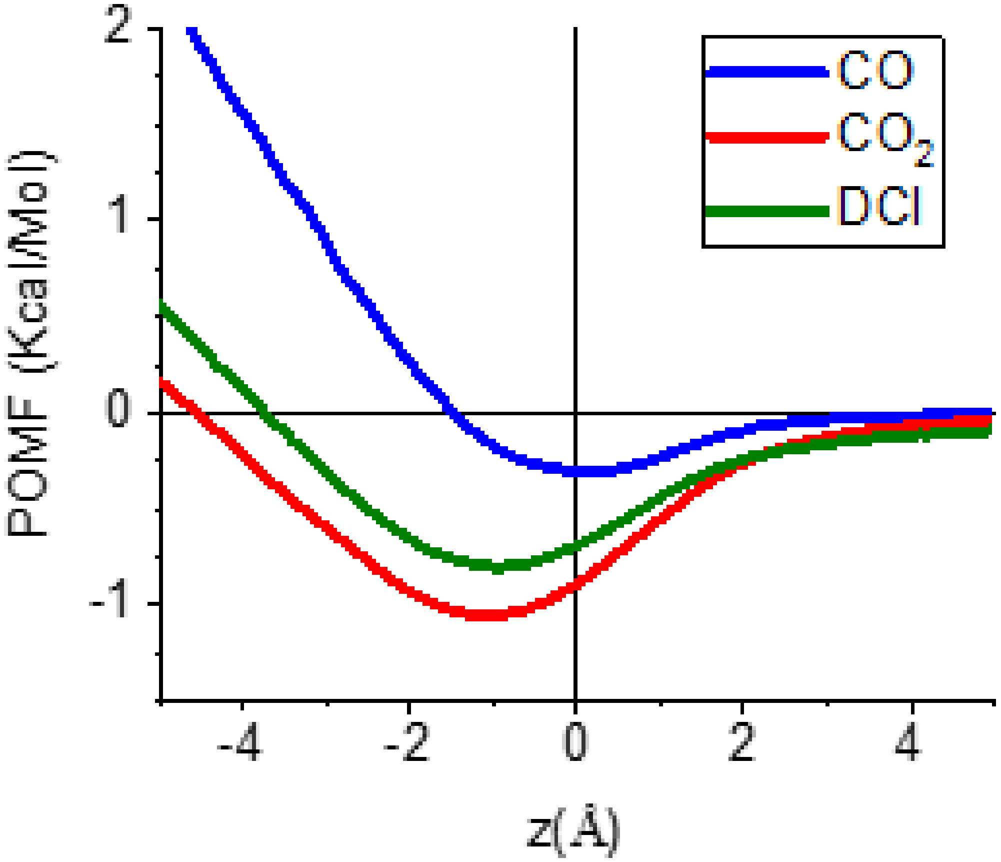

Fig. 4.9 Calculated potentials of mean force, $V_{POMF}(z)$, for CO, CO_2, and DCl projectiles with respect to distance from the FSAMs surface

both CO_2 and DCl exhibit notably shallower slopes of m ≈ 0.4 kcal/mol/Å. In summary, CO + PFPE thus clearly exhibits i) a weaker attractive well, ii) a $V_{POMF}(z)$ minimum shifted notably outward, and iii) more steeply repulsive interactions with the surface than experienced by either DCl or CO_2 projectiles, respectively.

4.5 Discussion

The combined experimental and theoretical results in this paper reveal anomalous behavior for supersonically cooled CO(J = 0) scattering at low energies (E_{inc} ≈ 0.1 – 1.0 kcal/mol) from the gas-liquid interface, specifically CO desorbing at rotational and translational temperatures i) out of equilibrium with and ii) colder than the surface (T_S). This is fundamentally at odds with conventional detailed balance considerations, for which trapping desorption (TD) events might be expected to dominate in the limit of low collision energies and unity sticking coefficients ($\alpha = 1$). A simple mechano-kinetic view of the TD process is summarized by three stages. 1) The projectile approaches the surface at sufficiently low energy for all incoming molecular states to become transiently bound in a physisorption well. 2) The molecule undergoes extended collisional interactions with the surface sufficient to thermalize with the liquid (T_S) and lose all residual memory of the incident collision. 3) The thermalized molecule eventually leaves the surface through a barrierless exit channel, which by detailed balance requires the asymptotic scattering state distributions to be accurately described by the surface liquid temperature, T_S. Experimental evidence in this work argues that CO does not leave the surface at T_S and thus clearly diverges from this putative TD pathway. The question of interest is where?

A first place to look would be final desorption from the liquid interface, for which the crucial assumption is that a molecule leaves along a monotonic and barrierless pathway. From atom-atom modeling of the gas-liquid potential, this assumption seems secure - the potential energy surface for all three projectiles rises monotonically from the bound well to infinite separation. This is true not only for the static atom-atom PES but also for the thermodynamically averaged potential of mean force (POMF). We can therefore be reasonably confident that the molecules do not experience transition state barriers and thus complex desorption dynamics (step 3) cannot explain why CO comes off the surface both translationally and rotationally colder than T_S.

We next consider the thermalization step 2, for which a TD event requires the projectile to undergo many interactions before leaving the surface. For a molecule trapped in a well and interacting with a thermal bath, the average residence time of the molecules should be described by Arrhenius behavior, with the first order rates decreasing (exponentially) with surface cooling. At sufficiently low temperatures, the slow rate constant for desorption is swamped by energy transfer to/from the surface, and thus the projectile has ample time to thermalize. But with increasing T_S, the Arrhenius desorption rate increases more rapidly than the molecule-surface equilibration rate. For initially jet cooled projectiles ($T_{rot} \approx 10K << T_S$) at low incident energies, as a result, one expects deviation in the desorption temperature *below* T_S (as observed), corresponding to a “roll off regime” as energy equilibration with the surface fails to compete with decreasing residence times. Experimentally, we see such suppression of equilibration dynamics (i.e., $T_{rot/trans} < T_S$) over the entire range of liquid temperatures accessible. Due to freezing points of the three (PFPE, squalane, and glycerol) liquids investigated, we are not able to reach lower temperatures experimentally, but the MD trajectory analysis empirically reveals that we are i) already in this roll off regime for CO scattering under near room temperature conditions and that these distributions become hyperthermal ($T_{rot} = T_{trans} > T_S$) at slightly lower temperatures. In summary, there is ample evidence in the MD simulations for non-thermalization and profound deviation from the TD dynamical paradigm. This is required for the scattered CO flux at low incident energies to exhibit a final translational/rotational quantum state distribution temperature lower than T_S, as experimentally observed.

As a parting comment, we note that step 2 may not be the only weak link in violation of the TD scattering paradigm. We consider the initial trapping event (step 1), which for a true TD event would rigorously require CO to become trapped in the well long enough to lose all memory of the incident collision conditions. Looking back at the MD simulations in Sec IV, one could argue equally strongly that CO never "traps" on the surface long enough to lose complete memory. Indeed, the key difference we see between (non-thermalizing) CO and the (thermalizing) DCl/CO_2 projectiles is that CO spends a 2-3 fold *shorter* time in the vicinity of the surface, clearly uncharacteristic with trapping desorption (TD) but rather an impulsive scattering (IS) pathway. Although unconventional to think of low energy inelastic gas-liquid scattering in this context, one simple physical interpretation could be that CO never interacts strongly enough with the liquid interface to either trap or equilibrate on the time scale of the collision event. Such novel collision dynamics might therefore best be characterized as a novel "sub-thermal impulsive scattering" (STIS) channel opening up at collision energies on the order of the well depth. Although further experimental and theoretical work will be required to support or refute such an interpretation, the existence of short lived, impulsive scattering at low energies serves to highlight the greater dynamical richness of collision pathways than previously considered in the early TD/IS models for quantum state resolved scattering dynamics at the gas-liquid interface.

4.6 Summary and Conclusion

Low energy scattering (E_{inc} = 1.0(1) kcal/mol) of CO has been studied from a systematic series of gas-liquid interfaces, exploiting high resolution infrared absorption methods to probe the final translational (out to plane $v_{Doppler}$) and rotational (J) quantum state distributions. The experimental studies reveal that CO scatters into a distribution characterized by distinctly *sub-thermal* (but nearly equivalent) rotational (T_{rot}) and Doppler translational (T_{trans}) temperatures ($T_{rot} \approx T_{trans} < T_S$). The results are fundamentally inconsistent with a traditional picture of complete accommodation (trapping-desorption, TD) at low incident energy of molecular scattering events from the gas-liquid surface.

To explore the physical origins of such phenomena, molecular dynamics simulations of CO, DCl, and CO_2 projectile scattering from a fluorinated self-assembled monolayer (FSAM) interface have been implemented, with atom-atom potentials modeled on high level ab initio MOLPRO calculations (CCSD(T)-f12/AVnZ-f12 (n=2,3,CBS)) as a function of CF_4 –projectile distance/approach angle and corrected for basis set superposition error (BSSE). These potential energy surfaces have then been implanted in the framework of the Venus molecular dynamics program to probe energy transfer and accommodation dynamics over an expanded range of collision energies and liquid temperatures, revealing remarkably quantitative agreement with experimental results. Detailed statistical analysis of the molecular dynamics permits comparison between CO_2, DCl and CO trajectories to elucidate mechanisms for projectile equilibration (or lack thereof) at the gas-liquid interface. Specifically, CO spends less time in the vicinity of the liquid interface and penetrate less deeply into the fluorinated surface compared to DCl and CO_2 projectiles. This difference in behavior has been statistically reiterated by potential of mean force ($V_{POMF}(z)$) calculations, which highlight a 2-3 fold *weaker well* depth and 2-3 times *steeper* *repulsive wall* for an CO-FSAM vs DCl-/CO_2-FSAMs potential energy surfaces. The experimental and theoretical quantum state resolved data reveal that CO does not trap long enough at low energies on the gas-liquid interface to result in complete energy equilibration with the liquid T_S. Instead, we argue that the experimental CO distributions violate the conventional paradigm of low energy scattering through complete equilibration with the liquid and are indeed more consistent with a novel “sub-thermal impulsive scattering” (STIS) pathway rather than a trapping-desorption (TD) event. The data provide mounting evidence for a greater richness of collision pathways than considered in the early TD/IS models for quantum state resolved scattering dynamics at the gas-liquid interface.

Chapter 4 References

1. Perkins, B. G.; Haber, T.; Nesbitt, D. J., Quantum State-Resolved Energy Transfer Dynamics at Gas-Liquid Interfaces: IR Laser Studies of CO_2 Scattering from Perfluorinated Liquids, *J. Phys. Chem. B* **2005**, *109*, 16396-16405.
2. Hurlbut, F. C.; Beck, D. E. “U.C. Eng. Proj. Report He-150-166”, 1959.
3. Cohen, S. R.; Naaman, R.; Balintkurti, G. G., Energy-Distribution between Spin-Orbit States in NO Scattered from Organized Amphiphilic Monolayers, *Chem. Phys. Lett.* **1988**, *152*, 269-273.
4. Cohen, S. R.; Naaman, R.; Balintkurti, G. G., Investigation of NO Scattering from Organic Monolayers - Spin-Orbit State and Vibrational-State Population-Distributions, *Chem. Phys.* **1989**, *134*, 119-126.
5. Perkins, B. G.; Nesbitt, D. J., Quantum-State-Resolved CO_2 Scattering Dynamics at the Gas-Liquid Interface: Incident Collision Energy and Liquid Dependence, *J. Phys. Chem. B* **2006**, *110*, 17126-17137.
6. Saecker, M. E.; Nathanson, G. M., Collisions of Protic and Aprotic Gases with Hydrogen-Bonding and Hydrocarbon Liquids, *J. Chem. Phys.* **1993**, *99*, 7056-7075.
7. Van Willigen, W., Angular Distribution of Hydrogen Molecules Desorbed from Metal Surfaces, *Phys. Lett. A* **1968**, *28*, 80-81.
8. Tully, J. C., Dynamics of Gas Surface Interactions - Thermal-Desorption of Ar and Xe from Platinum, *Surf. Sci.* **1981**, *111*, 461-478.
9. Brown, L. S.; Sibener, S. J., A Molecular-Beam Scattering Investigation of the Oxidation of CO on Rh(111) .2. Angular and Velocity Distributions of the CO_2 Product, *J. Chem. Phys.* **1989**, *90*, 2807-2815.
10. Yan, T. Y.; Hase, W. L., Origin of the Boltzmann Translational Energy Distribution in the Scattering of Hyperthermal Ne Atoms Off a Self-Assembled Monolayer, *Phys. Chem. Chem. Phys.* **2000**, *2*, 901-910.
11. Perkins, B. G.; Nesbitt, D. J., Quantum-State-Resolved CO_2 Scattering Dynamics at the Gas-Liquid Interface: Dependence on Incident Angle, *J. Phys. Chem. A* **2007**, *111*, 7420-7430.
12. Nathanson, G. M., Molecular Beam Studies of Gas-Liquid Interfaces, *Annu. Rev. Phys. Chem.* **2004**, *55*, 231-255.
13. Wu, B. H.; Zhang, J. M.; Minton, T. K.; McKendrick, K. G.; Slattery, J. M.; Yockel, S.; Schatz, G. C., Scattering Dynamics of Hyperthermal Oxygen Atoms on Ionic Liquid Surfaces: [Emim][Tf_2n] and [C_{12}mim][Tf_2n], *J. Phys. Chem. C* **2010**, *114*, 4015-4027.
14. Tesa-Serrate, M. A.; Smoll, E. J.; Minton, T. K.; McKendrick, K. G., Atomic and Molecular Collisions at Liquid Surfaces, *Annual Review of Physical Chemistry, Vol 67* **2016**, *67*, 515-540.
15. Tully, J. C., Washboard Model of Gas Surface Scattering, *J. Chem. Phys.* **1990**, *92*, 680-686.
16. Zhang, J. M.; Upadhyaya, H. P.; Brunsvold, A. L.; Minton, T. K., Hyperthermal Reactions of O and O_2 with a Hydrocarbon Surface: Direct C-C Bond Breakage by O and H-Atom Abstraction by O_2, *J. Phys. Chem. B* **2006**, *110*, 12500-12511.
17. Livingston Large, T. A.; Nesbitt, D. J., Quantum State and Doppler-Resolved Scattering of Thermal/Hyperthermal DCl at the Gas–Liquid Interface: Support for a Simple “Lever Arm” Model of the Energy-Transfer Dynamics, *J. Phys. Chem. C* **2019**, *123*, 3449-3460.

18. Lednovich, S. L.; Fenn, J. B., Absolute Evaporation Rates for Some Polar and Nonpolar Liquids, *AIChE Journal* **1977**, *23*, 454-459.
19. Perkins, B. G.; Nesbitt, D. J., Quantum State-Resolved CO_2 Collisions at the Gas-Liquid Interface: Surface Temperature-Dependent Scattering Dynamics, *J. Phys. Chem. B* **2008**, *112*, 507-519.
20. Ringeisen, B. R.; Muenter, A. H.; Nathanson, G. M., Collisions of HCl, DCl, and HBr with Liquid Glycerol: Gas Uptake, D -> H Exchange, and Solution Thermodynamics, *J. Phys. Chem. B* **2002**, *106*, 4988-4998.
21. Ringeisen, B. R.; Muenter, A. H.; Nathanson, G. M., Collisions of DCl with Liquid Glycerol: Evidence for Rapid, near-Interfacial D -> H Exchange and Desorption, *J. Phys. Chem. B* **2002**, *106*, 4999-5010.
22. Chorny, I.; Benjamin, I.; Nathanson, G. M., Scattering, Trapping, and Ionization of HCl at the Surface of Liquid Glycerol, *J. Phys. Chem. B* **2004**, *108*, 995-1002.
23. Hoffman, C. H.; Nesbitt, D. J., Quantum State Resolved 3D Velocity Map Imaging of Surface Scattered Molecules: Incident Energy Effects in HCl Plus Self-Assembled Monolayer Collisions, *J. Phys. Chem. C* **2016**, *120*, 16687-16698.
24. Bagot, P. A. J.; Waring, C.; Costen, M. L.; McKendrick, K. G., Dynamics of Inelastic Scattering of Oh Radicals from Reactive and Inert Liquid Surfaces, *J. Phys. Chem. C* **2008**, *112*, 10868-10877.
25. Ziemkiewicz, M. P.; Zutz, A.; Nesbitt, D. J., Inelastic Scattering of Radicals at the Gas-Ionic Liquid Interface: Probing Surface Dynamics of Bmim-Cl, Bmim-BF_4, and Bmim-Tf_2n by Rovibronic Scattering of NO ($^2\Pi_{1/2}(0.5)$), *J. Phys. Chem. C* **2012**, *116*, 14284-14294.
26. Zutz, A.; Nesbitt, D. J., Nonadiabatic Spin-Orbit Excitation Dynamics in Quantum-State-Resolved NO($^2\Pi_{1/2}$) Scattering at the Gas-Room Temperature Ionic Liquid Interface, *J. Phys. Chem. C* **2015**, *119*, 8596-8607.
27. Zutz, A.; Nesbitt, D. J., Quantum State-Resolved Molecular Scattering of NO ($^2\Pi_{1/2}$) at the Gas-[$C_n$mim][Tf_2n] Room Temperature Ionic Liquid Interface: Dependence on Alkyl Chain Length, Collision Energy, and Temperature, *AIP Adv.* **2016**, *6*, 105207.
28. Kubiak, G. D.; Hurst, J. E.; Rennagel, H. G.; Mcclelland, G. M.; Zare, R. N., Direct Inelastic-Scattering of Nitric-Oxide from Clean Ag(111) - Rotational and Fine-Structure Distributions, *J. Chem. Phys.* **1983**, *79*, 5163-5178.
29. Cavanagh, R. R.; King, D. S., Rotational-State and Spin-State Distributions - NO Thermally Desorbed from Ru(001), *Phys. Rev. Lett.* **1981**, *47*, 1829-1832.
30. McClelland, G. M.; Kubiak, G. D.; Rennagel, H. G.; Zare, R. N., Determination of Internal-State Distributions of Surface Scattered Molecules - Incomplete Rotational Accommodation of NO on Ag(111), *Phys. Rev. Lett.* **1981**, *46*, 831-834.
31. Hepburn, J. W.; Northrup, F. J.; Ogram, G. L.; Polanyi, J. C.; Williamson, J. M., Rotationally Inelastic-Scattering from Surfaces - CO + LiF(001), *Chem. Phys. Lett.* **1982**, *85*, 127-130.
32. Gisler, A. W.; Nesbitt, D. J., On Probing Ions at the Gas-Liquid Interface by Quantum State-Resolved Molecular Beam Scattering: The Curious Incident of the Cation in the Night Time, *Faraday Discuss.* **2012**, *157*, 297-305.
33. Oh-e, M.; Yokoyama, H.; Baldelli, S., Structure of the Glycerol Liquid/Vapor Interface Studied by Sum-Frequency Vibrational Spectroscopy, *Appl Phys Lett* **2004**, *84*, 4965-4967.
34. Proch, D.; Trickl, T., A High-Intensity Multi-Purpose Piezoelectric Pulsed Molecular-Beam Source, *Rev. Sci. Instrum.* **1989**, *60*, 713-716.

35. Nizkorodov, S. A.; Harper, W. W.; Chapman, W. B.; Blackmon, B. W.; Nesbitt, D. J., Energy-Dependent Cross Sections and Nonadiabatic Reaction Dynamics in F($^2P_{3/2}$, $^2P_{1/2}$) + nH_2 -> HF(v,J) + H, *J. Chem. Phys.* **1999**, *111*, 8404-8416.
36. Weida, M. J.; Caffey, D.; Rowlette, J. A.; Arnone, D. F.; Day, T., Utilizing Broad Gain Bandwidth in Quantum Cascade Devices, *Opt. Eng.* **2010**, *49*, 111120.
37. Martinez-Nunez, E.; Rahaman, A.; Hase, W. L., Chemical Dynamics Simulations of CO_2 Scattering Off a Fluorinated Self-Assembled Monolayer Surface, *J. Phys. Chem. C* **2007**, *111*, 354-364.
38. Perkins, B. G.; Nesbitt, D. J., Toward Three-Dimensional Quantum State-Resolved Collision Dynamics at the Gas-Liquid Interface: Theoretical Investigation of Incident Angle, *J. Phys. Chem. A* **2009**, *113*, 4613-4625.
39. Nogueira, J. J.; Vazquez, S. A.; Mazyar, O. A.; Hase, W. L.; Perkins, B. G.; Nesbitt, D. J.; Martinez-Nunez, E., Dynamics of CO_2 Scattering Off a Perfluorinated Self-Assembled Monolayer. Influence of the Incident Collision Energy, Mass Effects, and Use of Different Surface Models, *J. Phys. Chem. A* **2009**, *113*, 3850-3865.
40. H.-J. Werner; P. J. Knowles; R. Lindh; F. R. Manby; M. Schütz; P. Celani; T. Korona; A. Mitrushenkov; G. Rauhut; T. B. Adler; R. D. Amos; A. Bernhardsson; A. Berning; D. L. Cooper; M. J. O. Deegan; A. J. Dobbyn; F. Eckert; E. Goll; C. Hampel; G. Hetzer; T. Hrenar; G. Knizia; C. Köppl; Y. Liu; A. W. Lloyd; R. A. Mata; A. J. May; S. J. McNicholas; W. Meyer; M. E. Mura; A. Nicklaß; P. Palmieri; K. Pflüger; R. Pitzer; M. Reiher; U. Schumann; H. Stoll; A. J. Stone; R. Tarroni; T. Thorsteinsson; M. Wang; Wolf, A. Molpro, Version 2009.1, a Package of *Ab Initio* Programs, See Http://Www.Molpro.Net, 2009.
41. Peterson, K. A. Correlation Consistent Basis Sets. In *Peterson Group Website* http://tyr0.chem.wsu.edu/~kipeters/basis.html, 2019.
42. Hill, J. G.; Peterson, K. A.; Knizia, G.; Werner, H. J., Extrapolating MP2 and CCSD Explicitly Correlated Correlation Energies to the Complete Basis Set Limit with First and Second Row Correlation Consistent Basis Sets, *J. Chem. Phys.* **2009**, *131*, 194105.
43. Vanduijneveldt, F. B.; Vanduijneveldtvanderijdt, J.; Vanlenthe, J. H., State-of-the-Art in Counterpoise Theory, *Chem. Rev.* **1994**, *94*, 1873-1885.
44. Chalasinski, G.; Szczesniak, M. M., State of the Art and Challenges of the Ab Initio Theory of Intermolecular Interactions, *Chem. Rev.* **2000**, *100*, 4227-4252.
45. Grimme, S., Accurate Description of Van Der Waals Complexes by Density Functional Theory Including Empirical Corrections, *J. Comput. Chem.* **2004**, *25*, 1463-1473.
46. Peterson, K. A.; Dunning, T. H., Accurate Correlation Consistent Basis Sets for Molecular Core-Valence Correlation Effects: The Second Row Atoms Al-Ar, and the First Row Atoms B-Ne Revisited, *J. Chem. Phys.* **2002**, *117*, 10548-10560.
47. Hase, W. L.; Duchovic, R.; Hu, X.; Komornicki, A.; Lim, K. F.; Lu, D.-H.; Peslherbe, G.; Swamy, K.; Vande Linde, S.; Varandas, A.; Wang, H. L.; Wolf, R. Venus96: A General Chemical Dynamics Computer Program Texas Tech University, Lubbock, TX, 2005.
48. Nelson, R. D.; Lide, D. R.; Maryott, A. A. *Selected Values of Electric Dipole Moments for Molecules in the Gas Phase*; U.S. National Bureau of Standards: Washington, 1967.
49. Graham, C.; Imrie, D. A.; Raab, R. E., Measurement of the Electric Quadrupole Moments of CO_2, CO, N_2, Cl_2 and BF_3, *Mol. Phys.* **1998**, *93*, 49-56.

Chapter 5

Low Energy OCS Scattering:

A study of Vibrational Energy Transfer at the Gas-Liquid Interface

5.1 Introduction

A detailed understanding of chemical dynamics at the gas-liquid interface requires a equally detailed understanding of collisional molecular energy transfer, in principle, into each of the electronic, vibrational, rotational, and translational degrees of freedom. Through a multitude of elegant molecular beam techniques, including direct absorption laser spectroscopy[1-2], time of flight mass spectroscopy[3-5] and REMPI+VMI[6], collisional energy transfer between the scattering projectile and the surface has been explored extensively in translational and rotational degrees of freedom. In striking contrast to the potential complexity of such systems, it has been empirically found that these scattering pathways appear to "bifurcate" into two rather remarkably simpler channels. The first of the two is referred to as thermal desorption (TD), whereby an incident molecule traps transiently on the surface, achieves complete thermalization, and then desorbs from the surface from initial conditions sampling a near thermal equilibrium distribution. In colloquial language, such a subset of trajectories has "lost all memory" of the incident scattering conditions, and are found to occur on a > 10-100 ps time scale. We note that this does not require the final state distributions to remain in thermal equilibrium with the liquid, as there can still be dynamical barriers to successful desorption that are favored/disfavored by some fractional subset of the internal quantum and/or translational energy states.

The second pathway is denoted as impulsive scattering (IS), which corresponds to molecular scattering from the interface while still maintaining some residual "memory" of its initial scattering condition. In essence, this channel comprises all molecular flux that does not represent trapping desorption (TD), though unambiguous separation into one of these two channels is meaningful only statistically and rarely possible by inspection for a given trajectory. In general, contributions to this IS channel occur on a much faster time scale (< 1-10 ps) and contain all non-equilibrium dynamical information on the gas-liquid scattering event. In our molecular beam studies for non-orthogonal angles of incidence, this channel often appears as a lobular forward scattering peak with a hot yet remarkably "temperature-like" internal rotational quantum state distribution[2, 7-8]. It is worth noting that the existence of such "hyperthermal" rotational distributions in the IS channel is far from obvious and indeed quite surprising, though simple models based on smoothing of rainbow features by thermal roughening at the gas-liquid interface have been proposed that begin to capture this behavior for rotational degrees of freedom. Rather remarkably, however, there have been no studies reported of any such effects in IS scattering that include vibrational degrees of freedom, specifically vibrational excitation, deexcitation, and/or equilibration in molecular collisions at the gas-liquid interface. It is this inclusion of vibrational degrees of freedom in the gas-liquid scattering dynamics that represents the major focus of this work.

Vibrational energy transfer via collisions in the gas phase has been extensively studied. One essential trend observed is that vibrational energy transfer does not result from low energy collisions but rather from a smaller number of very large energy transfer collisions.[9] These general trends are well captured in Landau-Teller theory[10], which predicts that the vibrational energy transfer to be relatively inefficient and occurs only when the time dependent force f(t) between oscillator and the collider/perturber contains Fourier components that resonantly match the vibration frequency of interest.

A similar trend in the predissociation dynamics[11] of Van der Waals cluster was noted by Ewing and coworker, where large changes in vibrational quanta during the dissociation event are exponentially inhibited. For V → T transfer, this “exponential gap” penalty arises from a Franck-Condon type perspective through the vanishingly small overlap between the van der Waals repulsive wall potential and a rapidly oscillating translational wavefunction in the exit channel. In general, the kinetic acceleration of vibrational excitation or relaxation arises from the presence/absence of near resonant vibrational modes into which excess energy can be transferred from or into.

Investigation of vibrational energy transfer at the gas-condensed phase interface is a particularly challenging process. Of special note are the early pioneering studies by Wodtke and coworkers probing deexcitation of vibrationally prepared molecules on single crystal interfaces[12-15], which reveal two classic paradigms. If there is strong interaction/coupling with a single crystal metallic surface, for example with significant anionic character due to electron transfer from the metal to the molecule, the vibrational lifetimes are short and multiquantum ($\Delta v >>1$) vibrational energy transfer quite efficient[16]. For insulating single crystal materials, on the other hand, vibrational energy transfer efficiencies are found to decrease by several orders of magnitude, revealing only perturbative, harmonic oscillator like changes ($\Delta v \leq 1$) in the molecular vibrational quantum state. However, it is not simply a matter of conductive versus insulating materials, as there are single crystal metal-absorbate systems (Au + CO(v=1)) where molecular vibrations have been shown to survive for 100’s of picoseconds.[17] The vibrational metastability in such systems have been attributed to anomalously weak adsorbate-surface interactions, due to minimal electron transfer to/from the metal and leaving the molecule only weakly physiabsorbed. How these simple gas-surface intuitions might transfer from the long-range order of a single crystal to the far more disordered environment of a liquid remains largely unexplored and represents the major focus of this work.

This study takes special advantage of polyatomic molecules as projectiles for study of vibrational energy transfer dynamics at the gas-liquid interface. Carbonyl sulfide (OCS) is a particularly suitable molecular probe for such energy transfer dynamics, as a linear triatomic molecule with the right balance between small rotational constant (B = 0.203 cm^{-1}) and a strong infrared fundamental (590 km/mol) in the CO stretch region (2050 cm^{-1}) accessible to our quantum cascade laser. This combination allows for a large number of final scattered rotational states to be detected within the signal to noise of our experiment, with some 70 rotational J states below 1000 cm^{-1} and readily generated in collisions at the gas-liquid interface . Most importantly, polyatomic OCS also has two low lying vibrational modes below 1000 cm^{-1}, specifically the OCS bend at 520 cm^{-1} and the predominantly CS stretch at 860 cm^{-1}. As a result, both the OCS bend (01^10) and CS stretch (00^01) excited states are therefore already populated in the incident beam and can be sensitively observed via CO stretch “hot bands” (e.g., ($11^10 \leftarrow 01^10$) and (10^01) $\leftarrow$ (00^01)) in our laser spectrometer. Consequently, this offers the novel opportunity to study energy transfer i) from vibrationally excited OCS into the liquid as well as ii) excitation of these same polyatomic modes by thermal vs. hyperthermal collisions at the gas-liquid interface. Under the low energy conditions of the present studies, we find remarkably inefficient collisional energy transfer and equilibration dynamics, which

The organization of this chapter is as follows. A brief overview of the experimental spectrometer apparatus is described in section 5.2, with particular emphasis on the modifications to the laser frequency diagnostics and scattering apparatus required for working with such small rotational constant and polyatomic species. In Section 5.3, results are reported which explore vibrational, rotational, and transverse translational collisional energy transfer in OCS with several prototypical liquids under low energy beam conditions. The data highlight rapid equilibration dynamics in rotational/translational degrees of freedom, which stands in stark contrast with the extreme inefficiency and highly adiabatic nature of vibrational excitation/deexcitation dynamics. Section 5.4 explores these results in the context of simple dynamical theories and high level ab initio potentials for the collision events, with conclusions and directions for future study summarized in Section 5.5.

5.2 Experimental

The gas liquid scattering apparatus can be broken down into two major pieces, i) the mid-infrared shot-noise limited direct absorption spectrometer and ii) the scattering vacuum chamber. Many details of this experimental apparatus have been described elsewhere and can be briefly

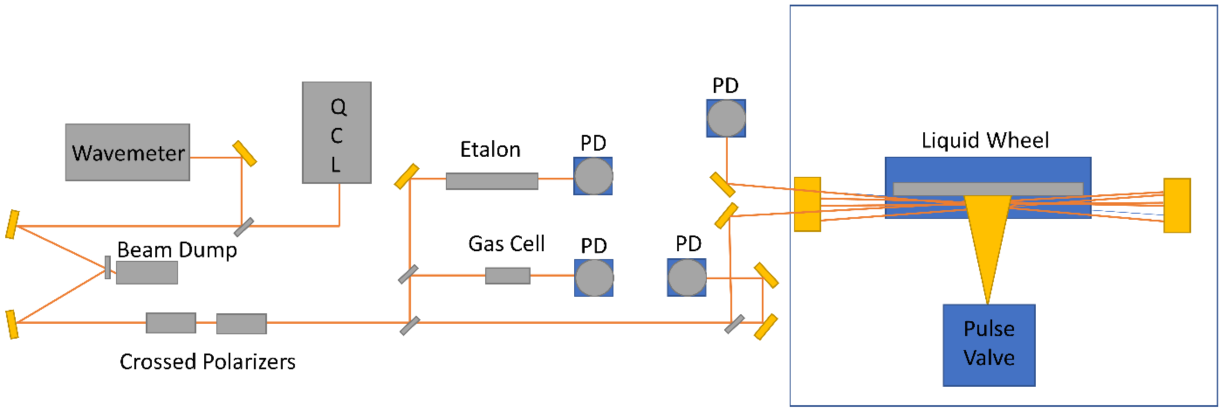

Figure 5.1: Layout of experiment

summarized, to which we include greater focus on specific apparatus modifications relevant to the present experiments[18-23].

A schematic diagram of the laser optical system is shown in Fig. 5.1. The light source is an external cavity single mode quantum cascade laser (Daylight Solutions), which generates as much as ~300 mW of single mode infrared light from ~2000-2200 cm^{-1} with a linewidth of ~10 MHz. This is far more than can be used for linear detection; thus the IR power is first reduced 50x by weak reflection from a BaF window and then adjustably trimmed to the desired level by a pair of crossed Rochon polarizers. After transmission through the rest of the optical system and vacuum scattering chamber, this results in ~10-30 uW on each of two LN_2 cooled InSb photodetectors. Our frequency diagnostics offer three stages of dynamic range. First we use a Michelson wavemeter (Bristol wavemeter 621b) to obtain an initial estimate (0.1 cm-1) of the spectral scan start frequency. Secondly, transmission signals from a room temperature gas cell (500 mT OCS, 1-5 cm path length) are also recorded, which in conjunction with the wavemeter reading permits unambiguous determination of the absolute frequencies from an OCS atlas. Thirdly, in order to provide a linear scan axis, we monitor the transmission fringes through an off-axis Fabry-Perot (bowtie) etalon with a moderate finesse of ~20-30 and 250 MHz FSR. Sample spectral diagnostics through the transmission cell and Fabry-Perot etalon are represented in Fig. 5.3, which indicate the presence of a strongly optically saturated absorption line on the CO stretch fundamental ($(10^00) \leftarrow (00^00)$, R(17)), with additional much weaker lines corresponding to hot band transitions out of the doubly degenerate OCS bend ($(11^10) \leftarrow (01^10)$, R(Y)), split into a e/f parity doublets by l-doubling in the $\nu_1 = 0$ and 1 lower/upper level.

Finally, the reduced IR light is split into signal and reference beams, with the distribution of final OCS rovibrational quantum states in the vacuum chamber probed by transient absorption of the quantum cascade laser signal light in a 16 pass Herriot cell, with the multipass axis oriented perpendicular to the scattering plane and at 65° from normal and 1 cm away from the point on the liquid surface struck by the skimmed molecular beam. The transmitted IR light is measured on our shot-noise limited spectrometer. This is achieved via a balanced detection scheme with one of the two arms contains the multipass cell in our vacuum chamber. This setup achieves absorbance sensitivities of around $1x10^{-5}$ in the bandwidth of the experiment.

The gas liquid scattering events occur in a 60 L Al vacuum chamber, evacuated by a 6-inch diffusion/roughing pump combination. In the presence of the molecular beam gas pulse, the chamber pressure is maintained $< 10^{-4}$ Torr, which ensures minimum mean free path lengths several times the dimensions of the vacuum chamber. The scattering system is made up of a molecular beam source, the scattering target and the multipass cell. The beam source is of Proch and Trickl design[24], with a mixture of 5% OCS/95% argon expanded through a 0.508 mm orifice at a stagnation pressure of P_{stag} ~ 80 torr, where the choice of low stagnation pressure achieves reasonably low rotational temperatures yet prevents clustering of OCS into dimers, trimers, etc., as verified by linear curves of growth vs. pressure for OCS transitions observed in the incident beam. The average speed in the molecular beam pulse is measured to be 550(50) m/sec, as measured by a simple time of flight setup as a function of microphone displacement. This translates into an incident OCS energy of 2.2(4) kcal/mol for collisions with the liquid surface, with the molecular beam entering from below and oriented 65^{o} from the liquid surface normal.

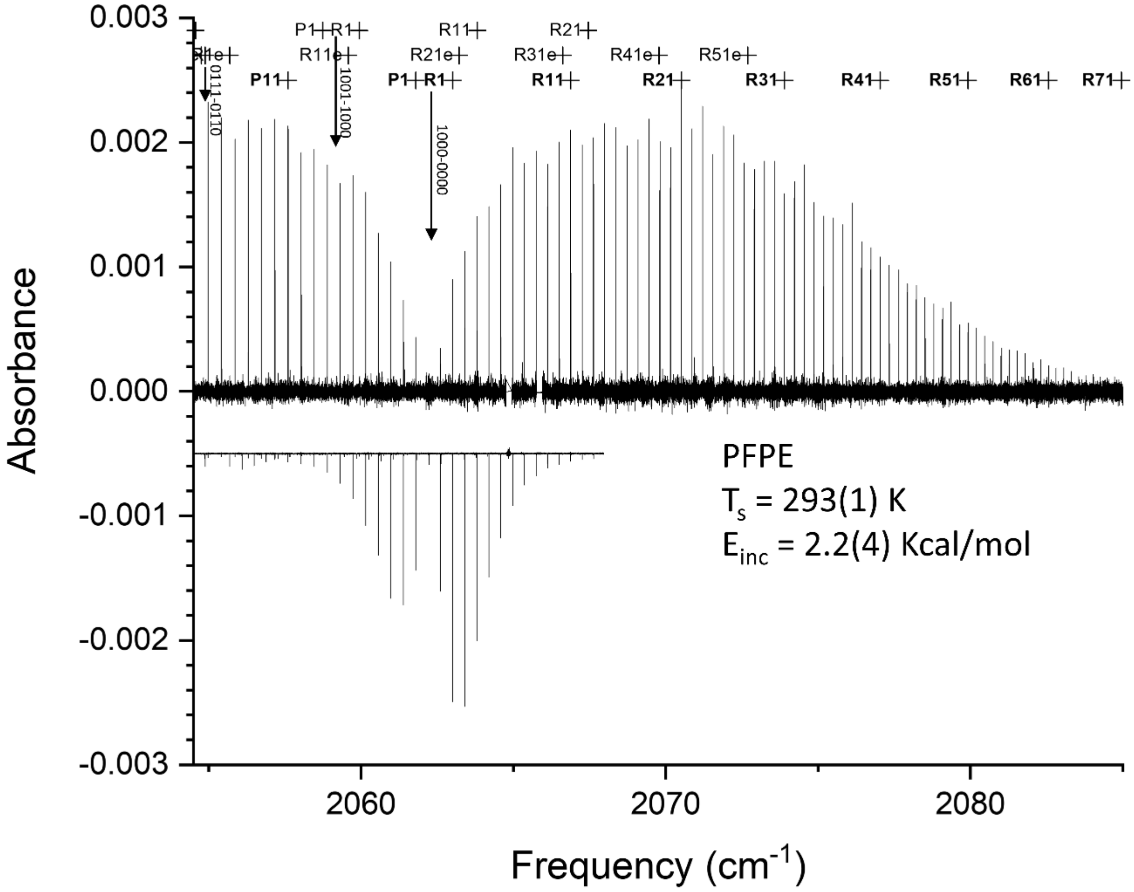

Figure 5.2: This is an example of a complete scan of OCS scattering from PFPE at low collision energies. The downward spectrum is of the incident molecular beam

By way of assessment of OCS rotational/vibrational cooling in the supersonic expansion, we monitor the CO stretch spectrum of the incident molecular beam. As shown in Fig. 5.2, there are clearly contributions from the ground (00^00) as well as both the low-lying OCS bend (01^10) and CS stretch (00^01) excited states. From Boltzmann analysis of rotational populations in each of the lower vibrational states, we obtain a rotational temperature of 10K. However, an equivalent Boltzmann analysis of populations in each manifold (summed over all J states) yields a vibrational temperature of T_{vib} = 240(5) K, which is clearly much hotter than the T_{rot} = 10K rotational temperatures in the supersonic expansion. Such highly non-equilibrium behavior between rotation and vibration arises from the much larger number of collisions required to cool vibrations in a supersonic pinhole expansion, essentially due to the much larger vibrational (10^2-10^3 cm-1) vs rotational (10^0-10^1 cm-1) energy spacings to be collisionally removed. Indeed, this provides another indication of "frustrated" vibrational energy transfer dynamics already in the throat of a pinhole supersonic expansion, which provides a crucially important baseline for interpreting the subsequent collision dynamics at the gas-liquid interface.

The liquid target for these scattering studies is based on a temperature dependent rotating wheel setup described in reference[18]. The liquid scattering surface is prepared according to the method of Lednovich and Fenn[25], using a rotating (~ 0.2 Hz) bead blasted stainless steel wheel (12.7 cm diameter) half-submerged in the copper liquid reservoir and scraped with a stationary razor blade to present a thin (~500 um), freshly prepared gas-liquid surface to the impinging molecular beam. The liquid reservoir and gas-liquid surface are thermally isolated from the rest of the vacuum chamber by Teflon spacers, with the liquid surface temperatures stabilized by a two-stage servo loop cooling apparatus. The majority of the thermal cooling/heating is achieved by means of an ethanol recirculating chiller, which incrementally cools/heats the backplate a thermoelectric element that servo loop stabilizes the temperature of a thermistor epoxied to the front of the copper trough.

This study investigates three different classes of liquids that sample different scattering dynamical regimes: 1) perfluorinated polyether, (PFPE, Krytox 1506, $F\text{-}[CF(CF_3)CF_2O)]_{14(avg)}\text{-}CF_2CF_3$), as a prototype for a rough but chemically inert liquid surface, 2) squalane (2,6,10,15,19,23-hexamethyltetracosane, $C_{30}H_{62}$), as a prototype for fully aliphatic, strongly hydrophobic surface, and 3) glycerol (1,2,3-propanetriol, $C_3H_8O_3$), as a prototype for a much more hydrophilic surface due to multiple protruding OH groups. Each liquid is degassed under ~1 mTorr vacuum at room temperature for several hours to remove dissolved atmospheric gases, or at slightly elevated temperatures (~ 350 K) for the glycerol liquid samples to allow for complete degassing within a reasonable (overnight) time frame.

Our quantum-state and Doppler-resolved scattered OCS signals are measured in a 16 pass concentric Herriot cell with a single pass cell length of ~40 cm. As can be seen in Fig. 5.1, this multiple beam path lies along the plane of liquid surface and perpendicular to the molecular beam. This means that the Doppler broadening reports on the velocity perpendicular to the scattering plane made by the liquid surface normal and the molecular beam. A crucial addition to the scattering setup is a LN_2 cooled cold plate at the top of the vacuum chamber, which helps us achieve surface liquid operating temperatures of 90 K when cooled and implemented to reduce the background OCS in the vacuum chamber. Since the FWHM of a room temperature OCS transition is typically ~100 MHz and the QC laser linewidth is ~10 MHz, this results in virtually no appreciable frequency noise contribution from the scattered signal. However, since frequency noise on the background gas in our chamber is not common mode on both the signal and reference detectors, it passes straight through our subtraction circuit and appears as extra noise. This noise can be effectively removed by cryopumping to reduce the background OCS signal by ~10-100-fold, which in turn reduces frequency noise by an equivalent amount.

The experiment consists of computer controlled recording time domain traces (2 ms) of the scattered OCS gas pulse at each laser frequency (step $\Delta\nu$ = 3 to 7 MHz) over the 2054.5 to ~2090 cm^{-1} frequency window. This scan range is broken into smaller computer controlled "continuous" step scans of ~0.8 cm^{-1}, with approximately 0.1 cm^{-1} overlap between each scan to eliminate any gaps in the spectrum. The time traces at each laser frequency step are converted into absorbance

Figure 5.3: Experimental diagnostics: the etalon trace and the thermal OCS reference gas cell allow for precise frequency alignment (* marked lines are isotope OCS lines)

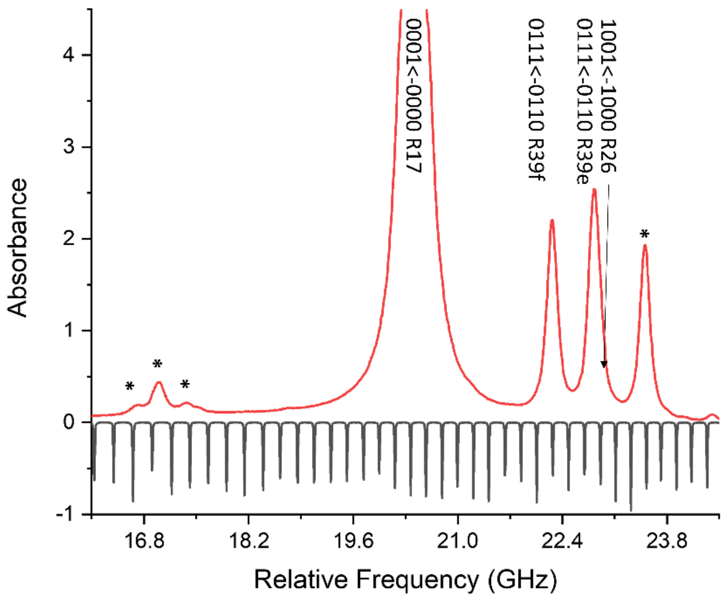

A(ν) by integrating over the rising edge (300 μs) of the gas pulse, subtracting an equivalent integrated baseline (300 μs window before the gas pulse), scaling the transmitted signal by incident light level, and expressing as a base e logarithm. The relative frequency axis for each scan is calculated by linear interpolation between etalon peaks, with zeroth order absolute frequency estimates from the Bristol wavemeter. Such wavemeter readings contain small systematic offsets but are sufficiently precise to unambiguously match to our reference cell OCS spectrum, which therefore provides absolute frequencies by comparison with a high precision Hitran database.[26] An example of the reference cell and etalon traces are displayed in Fig. 5.3 The net result is an information dense spectral scan with 150,000 – 350,000 elements covering the entire R branch

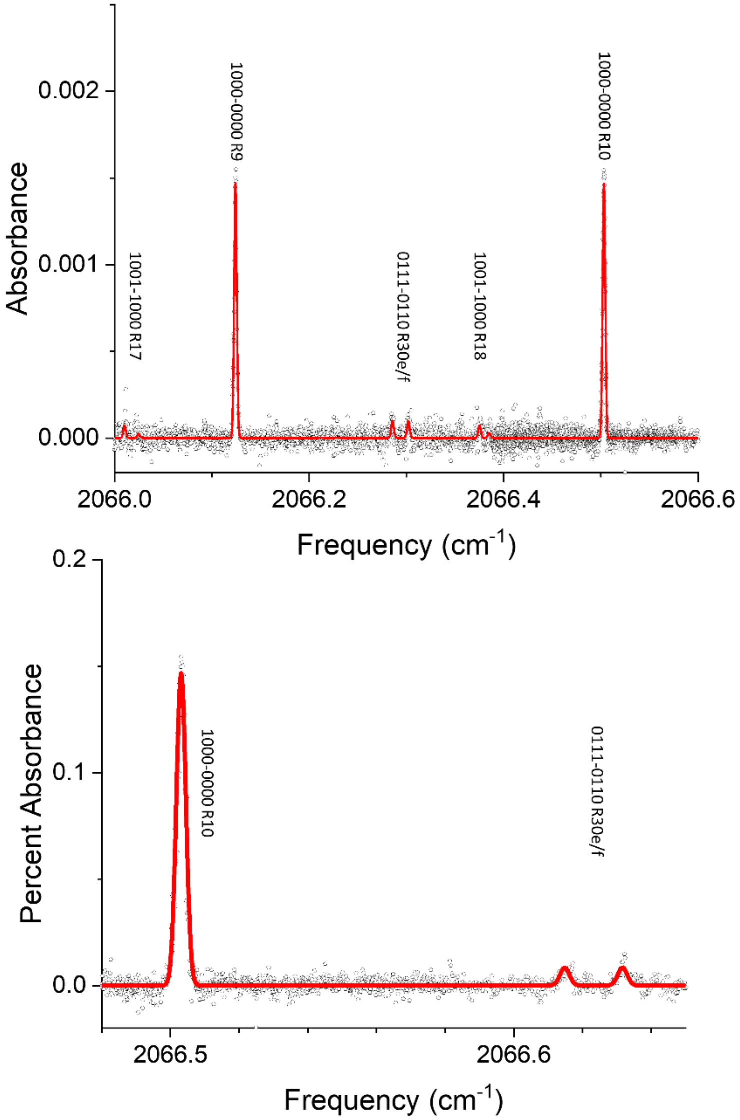

Figure 5.4: These are blowups of spectrum of Fig 5.2 compared with the fit model spectrum.

region (and much of the P branch region) for the fundamental $((10^00) \leftarrow (00^00))$ and hot bands $((11^10) \leftarrow (01^10), (10^01) \leftarrow (00^01))$ out of the ground (00^00) and lowest two vibrationally excited states $((01^10), (00^01))$.

5.3 Results and Analysis

Extraction of the quantum state resolved column integrated molecular densities is obtained by global fit of the high resolution scattering spectra,[27] with a sample fit region displayed in Fig. 5.4. The analysis is based on least squares adjusting a population model based on Hitran transition frequencies to fit the entire spectrum, which includes MHz level of the reference etalon FSR to account for long term drift (~10 ppm day to day variation). The spectral model is based on several reasonable assumptions. First, each upper state of the spectroscopic transition is completely unpopulated, with the probing vibrational transition ~2000 cm^{-1} above the ground state and inaccessible at the collision energies explored. Secondly, the high resolution lineshapes for each transition are Doppler limited and arise from a common Gaussian distribution of velocities. This experimental spectrum can be expressed as the following linear model:

$$A(f_j) = \sum_i S_i(f_j) * P_i \qquad \text{Eq. 1}$$

where P_i are the quantum state populations and $S_i(f_j)$ is the calculated spectrum from state i at frequency point f_j. The list of integrated cross-sections are obtained from the Hitran library, where only transitions from the common isotopomers $^{16}O^{12}C^{32}S$ (94%) and $^{16}O^{12}C^{34}S$ (4%) are considered. From fitting this model spectrum ($A(f_j)$) to the experimentally collected spectrum, the column integrated molecular densities (P_i) can be extracted in a linear least squares fit. The high quality of spectral alignment is evident in both Fig, 5.3 and 5.4, with the quality of line shape modelling seen in the spectral blowup in Fig. 5.4.

The extracted populations from such a linear least squares model for scattering of OCS at E_{inc} = 2.2(4) kcal/mol from PFPE at T_S = 293 K are summarized in Fig. 5.5. In addition to extensive collisional energy transfer into a large number of rotational levels (up to J = 67 at E_{rot} = 1095 cm^{-1}), the data clearly also signal significant populations in both the ground and the two lowest

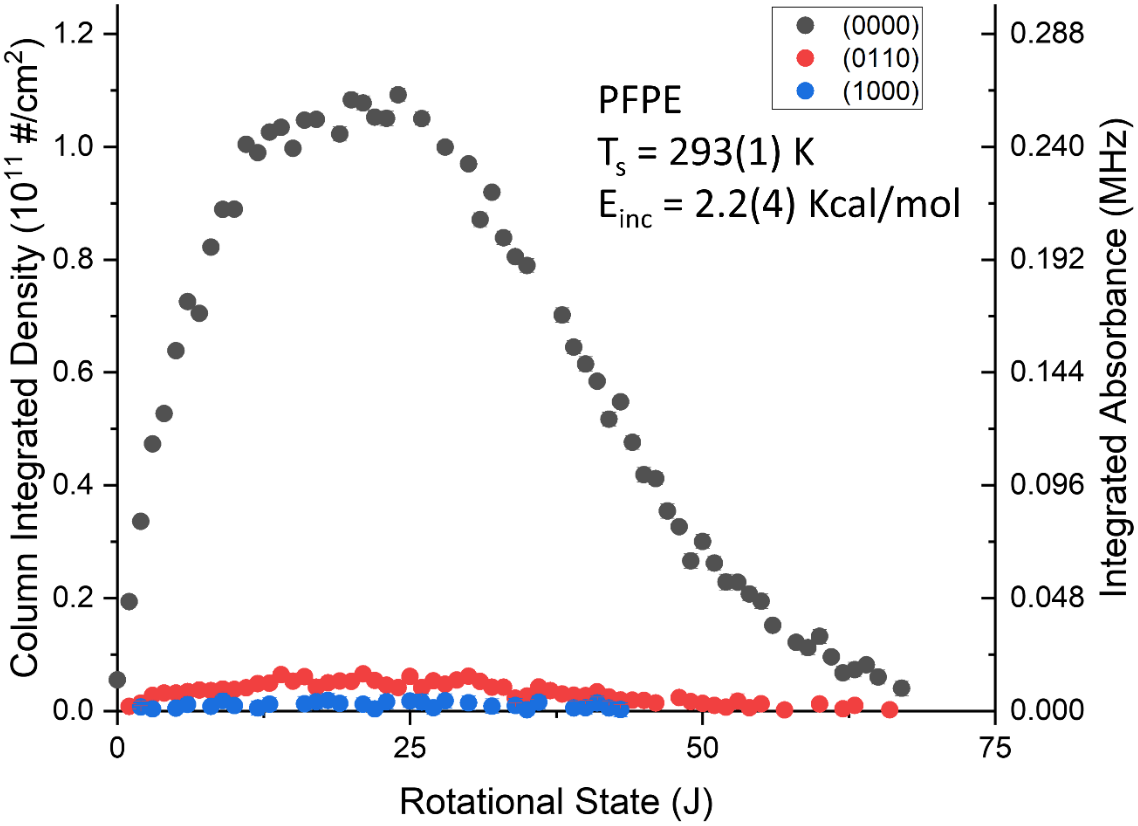

Figure 5.5: Extracted populations from the model fit.

vibrational manifolds. In the construction of these linear population fits, we have restricted the rotational states to >100 cm^{-1} due to residual incident beam contamination along the laser absorption path.

Closer inspection of the rotational distributions (Fig. 5.6) reveals that each of the vibrational manifolds looks “temperature-like” and can be well fit with a simple rotational Boltzmann distribution. Indeed, each manifold of states exhibits rotational temperatures within experimental error, with slopes corresponding to $T_{R,gnd\ state}$ =290(7) K $T_{R,\ OCS\ bend}$ = 297(20) K and $T_{R,\ CS\ stretch}$ = 310(100) K for the ground, OCS bend, and CS stretch excited modes, respectively. These three distributions are experimentally indistinguishable, which from an Occam’s razor

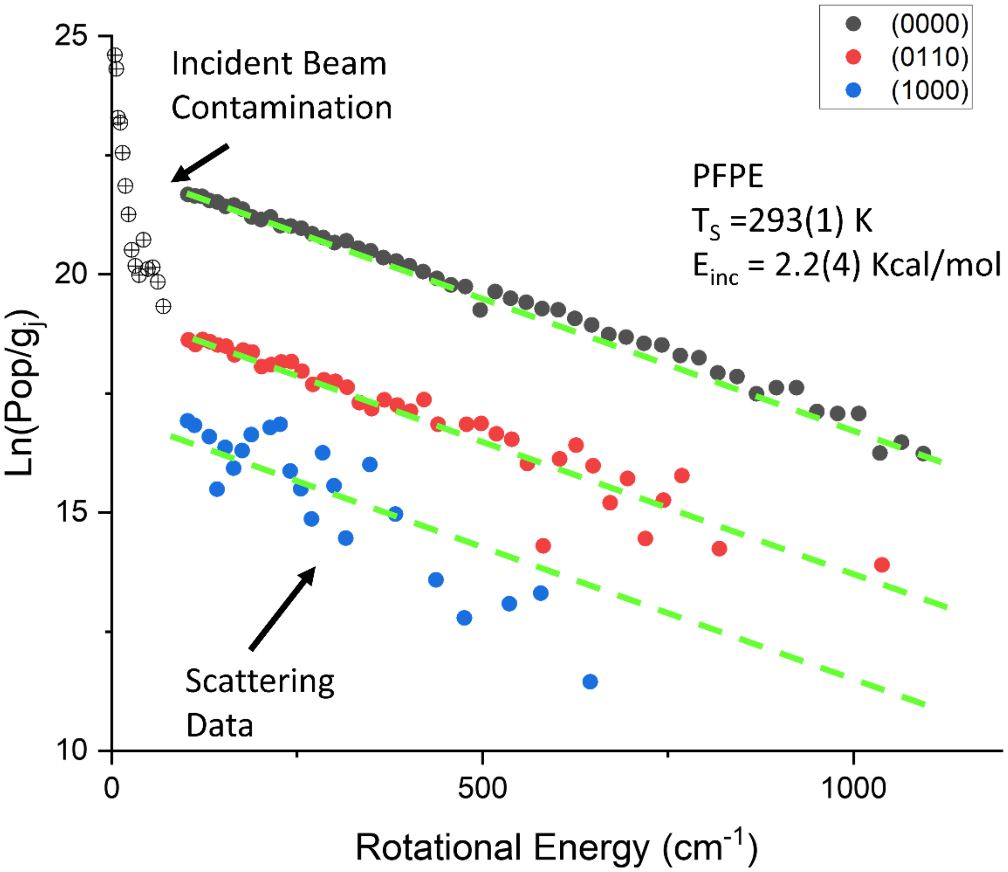

Figure 5.6: Rotational Boltzmann plot

perspective motivates analysis as a single equilibrated manifold. By way of additional support, $T_{rot} = 298(5)$ K results from a fit to a common rotational temperature, matching well with the liquid surface temperature of $T_S = 294(1)$ K. Simply stated, the data in each of the three vibrational manifolds suggest complete rotational thermalization with the surface, at least at the molecular beam collision energies (E_{inc} = 2.2(4) kcal/mol) explored herein. From detailed balance considerations, such behavior would be consistent with unity sticking coefficients into a longer lived trapping-desorption (TD) channel from any rotational states populated in the incident beam, as indeed has been confirmed previously in a number of gas-liquid molecular projectile scattering systems.

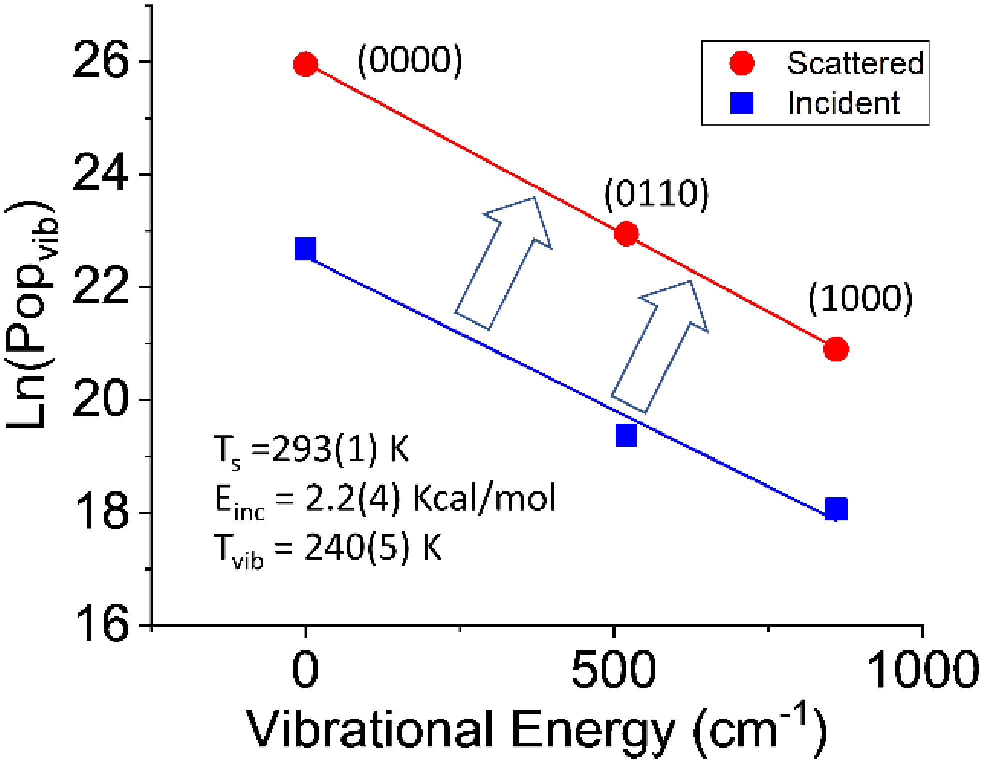

Figure 5.7: Vibrational Boltzmann plot of both the incident beam and the scattered molecules

Of particular dynamical interest and explicit focus of the present work is a first glimpse at the distribution of final vibrational states in the scattered polyatomic projectile. Specifically, we can sum over all rotational states and look at total populations in each of the vibrational manifolds. Despite a limited number of data points, these vibrational populations (in red) fall quite nicely on a linear Boltzmann plot and are consistent with a vibrational temperature of T_{vib} = 240(5) K. However, particularly noteworthy in Fig. 5.7 is the comparison plot (in blue) for relative vibrational populations in the incident molecular beam, which is remarkably parallel to the corresponding Boltzmann plot for the scattered populations (in red). This striking degree of parallelism makes clear that there is little if any change in the OCS vibrational populations, before and after a collision with the gas-liquid interface. Therefore, the highly non-equilibrium rovibrational cooling dynamics in the supersonic expansion (i.e., $T_{rot} \approx 10K << T_{vib} \approx 240(5)K$) is recapitulated in the scattered flux, but now with i) the rotations *warming rapidly up to* and ii) vibrations in our polyatomic OCS projectile remaining substantially *colder than* the liquid surface temperature, TS (i.e., $T_{rot} \approx 298(5)K > T_{vib} \approx 250(5)K$). Simply stated, the vibrational degrees of freedom in the OCS projectile remain weakly coupled with the liquid interface, which speaks to a high degree of vibrational adiabaticity in the gas-liquid collision dynamics. Though such a propensity for vibrational adiabaticity is well appreciated for gas phase collisions, the corresponding trend for collisions at the gas-liquid interface is far less evident, with the present data on OCS scattering representing, to the best of our knowledge, the first such direct evidence for weak vibrational state inelastic collision dynamics.

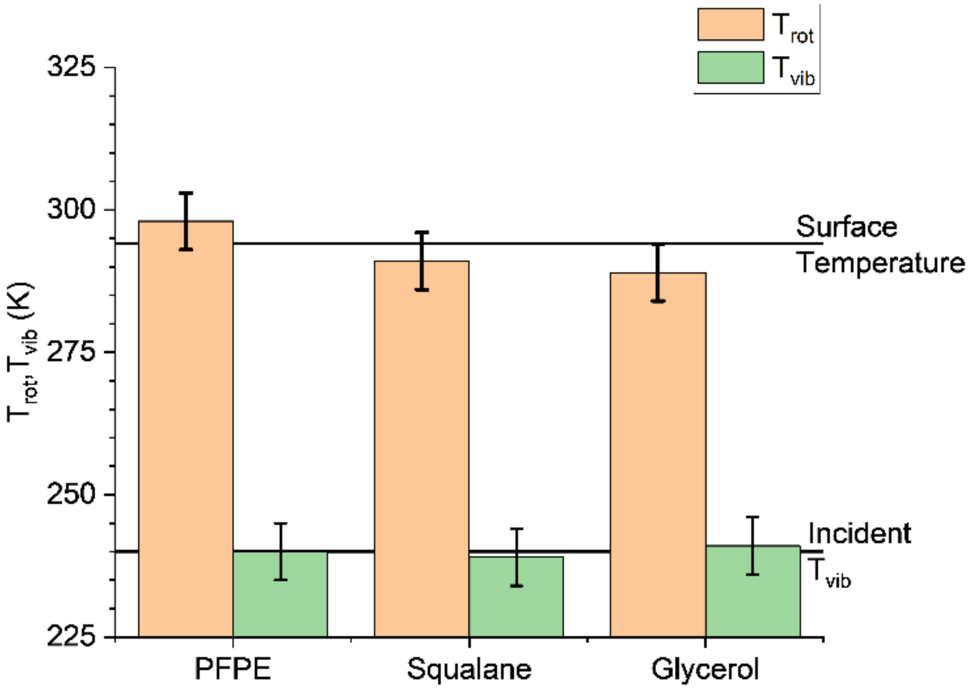

Figure 5.8: Summary of scattering parameters of multiple liquids

One could reasonably argue that this behavior depends sensitively on the nature of the molecule-liquid intermolecular potential. In the interest of completeness, we have supplemented our current data with OCS scattering (E_{inc} = 2.2(4) Kcal/mol) on the surfaces of two other low pressure liquids commonly studied in the gas-liquid scattering literature, specifically squalane and glycerol. Spectral fits and population analysis for these additional liquids proceeds identically to that of PFPE scattering, yielding fully thermalized rotations and yet highly non-equilibrium vibrational distributions. The fitted temperature results of these studies for all three liquids are summarized in Fig. 5.8. Within experimental uncertainty, all three liquid systems show qualitatively identical behavior with respect to rotational thermalization (T_{rot}) to the surface temperature (T_S). Of greater relevance to the current study, however, there is no change in the vibrational temperature (T_{vib}) of the scattered OCS with respect to the incident beam.

This striking nonequilibration of OCS vibrations at the gas-liquid interface despite clear evidence for full equilibration of rotational and translational degrees of freedom deserves to be further tested. As an ancillary set of experiments, low energy scattering studies have been repeated for OCS scattering from PFPE liquid under a wide variety of liquid interfacial temperature conditions. Specifically, OCS rotational populations in each of the three vibrational manifolds ((0000), (0110), (1000)) have been subjected to Boltzmann analysis to yield T_{rot}, with the total populations summed in each manifold to yield vibrational distributions and fitted to yield values of T_{vib}. The resulting dependence of T_{vib} and T_{rot} on liquid PFPE temperature (T_S = 263.15-303.15 K) is summarized in Fig 5.9.

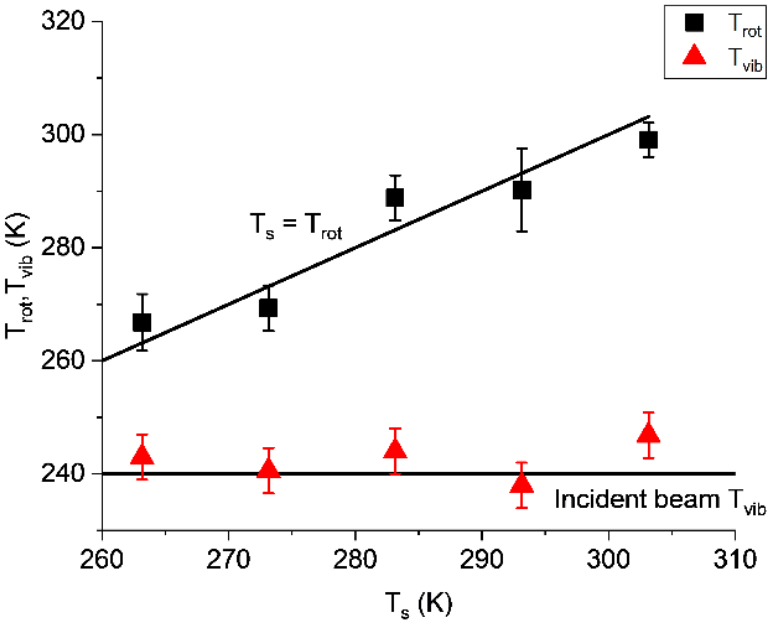

Figure 5.9: Surface temperature dependence of the rotational and vibrational degrees of freedom

There are several things that are immediately noticeable. 1.OCS clearly rotationally thermalizes with the surface and 2. Vibrationally, OCS does not seem to undergo any interaction at all, leaving the vibrational degrees of freedom as spectators in this scattering event. By the current understanding of the TD channel, this rotational thermalization is a characteristic of the TD pathway. However, the vibrations undergo this same dynamical pathway and show different behavior, thus, it is clear that vibrations must be considered separately from the other degrees of freedom.

5.4 Discussion

The current study presents first results for vibrationally quantum state resolved scattering of a polyatomic molecule (OCS) at the gas-liquid interface, which has permitted probing of thermal accommodation dynamics with both i) rotational and ii) multiple vibrational degrees of freedom. The essential results at E_{inc} = 2.2(4) kcal/mol are readily summarized. 1) Rotational degrees of freedom in the OCS/Ar molecular beam are strongly cooled by virtue of the supersonic expansion ($T_{rot} \approx 10K$) and yet rapidly thermalize ($T_{rot} \approx T_S$) in single low energy collisional interactions with each of three gas-liquid interfaces. 2) By way of clear contrast, distributions in the lowest three thermally populated vibrational states (00^00, 10^00, 01^10) are only very weakly cooled in the supersonic expansion ($T_{vib} \approx 230K$) and yet continue to remain completely unequilibrated in subsequent collisions with the corresponding three liquid surfaces. In order to explore the dynamics of such non-equilibrium effects, we consider predictions from simple analytic models of collisional energy transfer.

We first note that such behavior can be qualitatively rationalized by simple expectations from collisional perturbation theory. In the framework of such perturbation theories, the collisional mixing between asymptotic rovibrational quantum states Ψ_I and Ψ_j is proportional to the square of the off diagonal matrix element of the interaction Hamiltonian scaled to energy difference between the states, i.e.,

$$\Gamma = |<\Psi_i|V_{int}|\Psi_j>|^2/\Delta E_{ij}. \qquad \text{Eq. 2}$$

For the case of pure *rotational transfer* where energy differences are relatively small ($\Delta E_{ij} = B_{OCS} J(J+1) << E_{inc}$), it takes only weak collisional interactions to mix these states, therefore correctly predicting facile thermal equilibration at the gas-liquid interface, as indeed experimentally observed.

This is fundamentally different from the dynamical behavior anticipated for *vibrational* degrees of freedom in OCS, which exhibit 2-3 orders of magnitude larger spacings, e.g., $\Delta\nu_{OCS\ bend}$

= 520 $\mathrm{cm^{-1}}$, $\Delta\nu_{\mathrm{CS\ stretch}}$ 860 $\mathrm{cm^{-1}}$, which therefore requires a much stronger collisional coupling interaction to excite/deexcite or thermalize the vibrational state distribution. In particular, since these vibrational spacings are only comparable to the incident collision energy (E_{inc} = 2.2(4) kcal/mol), this would rationalize quite inefficient energy transfer into/out of the polyatomic vibrational degrees of freedom. Indeed, due to the finite number of collisions (perhaps 100-300) in a supersonic jet (P_{stag} = 100 Torr, N_{coll} = 100-200), this simple model motivates both i) poor vibrational cooling down from T_{stag} in the pinhole supersonic expansion, as well as ii) a highly constrained thermal equilibration of these high frequency polyatomic vibrational modes in subsequent collisions with the gas-liquid interface.

We can put these non-equilibrium predictions on a more quantitative footing by calculating the ab initio interaction potential for OCS collisions with the PFPE surface. To keep things simple, we have obtained 1D potential energy curves for each of seven different approach geometries for OCS colliding with a carbon-tetrafluoride molecule (CF_4). For each intermolecular geometry and distance, high level ab initio calculations have been performed (MOLPRO platform), using explicitly correlated (f12) electron methods at the CCSD(T)-f12 level with f12 correlation consistent Dunning basis sets (AVnZ-f12; n=2,3,4). Additionally, we perform standard counterpoise corrections for basis set superposition error (BSSE) and perform an extrapolation to the complete basis set limit (CBS). The seven 1D geometries are chosen corresponding to strongest possible interactions between our effective liquid surface and scatterer, with sample results from two such 1D approach geometries (top panel, OCS coplanar with the FCF moiety; bottom panel, OCS colinear with the CF bond) captured in Fig. 5.10. Least squares fits of these 1D potentials to a simple Morse potential function predict well depths that vary from 0-1 kcal/mol, with characteristic exponential repulsive wall parameters of roughly $\alpha = 2/\text{Å}$.

A near analytical quantum model for vibrational energy transfer was developed by Landau and Teller, whereby a structureless atom collisionally interacts with a collinear diatomic via an exponentially repulsive potential $V_{1D}(x) = V_0 \exp(-\alpha x)$. The three key model assumptions are i) harmonic vibrations, ii) linearized coupling in differential displacement of the proximate atom, and iii) collisional time scales much longer than the vibrational period. Based on these

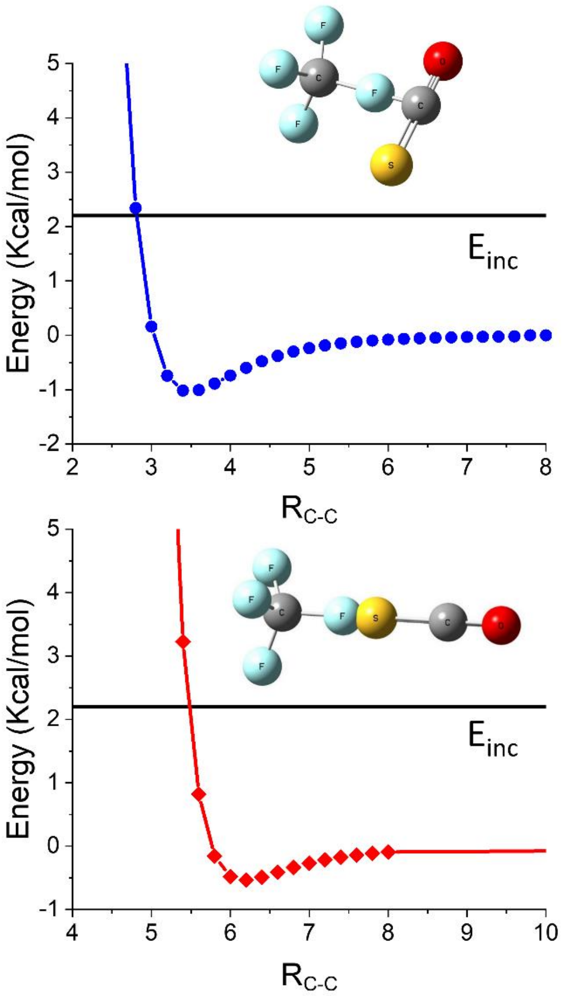

Figure 5.10: Examples of calculated approaches. The top is an example an approach for the OCS bend and the bottom is an example an approach for the CS stretch

assumptions, Landau and Teller were able to derive perturbative collision excitation probabilities from v = 0 → 1 of the form:[28]

$$P_{0\to 1} \sim exp\left(-\frac{2\pi\omega}{\alpha v_0}\right) \qquad \text{Eq. 3}$$

where ω is the angular frequency (radians/sec) of the vibration under study, α the exponential repulsion potential parameter, and v_0 the asymptotic approach velocity. While the prefactor in Eq X proves difficult to calculate quantum mechanically, one can estimate it from a closely related semiclassical derivation by Rapp for collinear A+ BC(v”) → A + BC(v’) collisional excitation.[29] Specifically, the v = 0 → 1 semiclassical transition probability can be analytically written as:

$$P_{0\to 1} = 8\,\pi^2\,\frac{\omega}{\hbar\,\alpha^2}\,\frac{\mu_{A,BC}^2}{\mu_{BC}}\,\frac{M_C^2}{(M_B+M_C)^2}\,e^{-\frac{2\pi\omega}{v_0\alpha}} \qquad \text{Eq. 4}$$

for which $\mu_{A,BC}$ and μ_{BC} represent the reduced masses of A + BC and BC, and m_B, m_c as the near and far diatomic atoms, respectively. To apply such a simple diatomic model to our more complex polyatomic OCS projectile requires additional modification of Eq (4) to take into account i) effective normal mode mass and ii) overlap of the proximate atom B displacement onto the vibration coordinate of interest. For our present purposes, it suffices to treat the ν_3 mode as a “local” CS stretch with effective diatomic masses $M_B = M_S$ (32 amu) and $M_C = M_C + M_O$ (28 amu) and similar considerations for the “local” ν_2 bending mode dominated by motion of the central C atom resulting in M_B = 12 amu and M_C = 48 amu. Furthermore, we can expand the Morse potential as locally linear in atom B displacement and replace the exponential repulsion parameter by the logarithmic derivative $\alpha = \partial \ln\{V_{Morse}\}/\partial r$, evaluated at the classical turning point of closest approach, i.e., $V_{Morse}(r) = E_{inc}$. From Morse potential fits to both of the approach geometries shown in Fig. 5.10, one finds $\alpha \approx 6(1)/\text{Å}$ at $E_{inc} \approx 2.2(4)$ kcal/mol.

The resulting theoretical predictions for the $P_{0\rightarrow1}$ inelastic collision probability vs. the dimensionless exponent $2\pi\omega/\alpha v_0$ are plotted in Fig. Z for both (v_1) CS stretch and (v_2) OCS bend excitation. Although not immediately interpretable in terms of a rate constant for thermal accommodation at the gas-liquid interface, the reciprocal probability ($1/ P_{0\rightarrow1} = Z$) does represent a plausible estimate for the number of such low energy collisional interactions Z required to achieve significant equilibration of a given vibrational degree of freedom in OCS with T_S. For $E_{inc} \approx 2.2(4)$ kcal/mol, these predictions are of order $Z = 10^{12}$ and 10^{23} for the v_2 (01^10) OCS bend and v_1 (10^00) CS stretch, respectively. Though such simple predictions from inelastic Landau Teller theory plus semiclassical extensions by Rapp are likely to fail quantitatively at these longer interaction times, the above calculations in Fig. 5.11 certainly drive home the self consistent message that i) even relatively low energy vibrations in polyatomic projectiles remain largely in

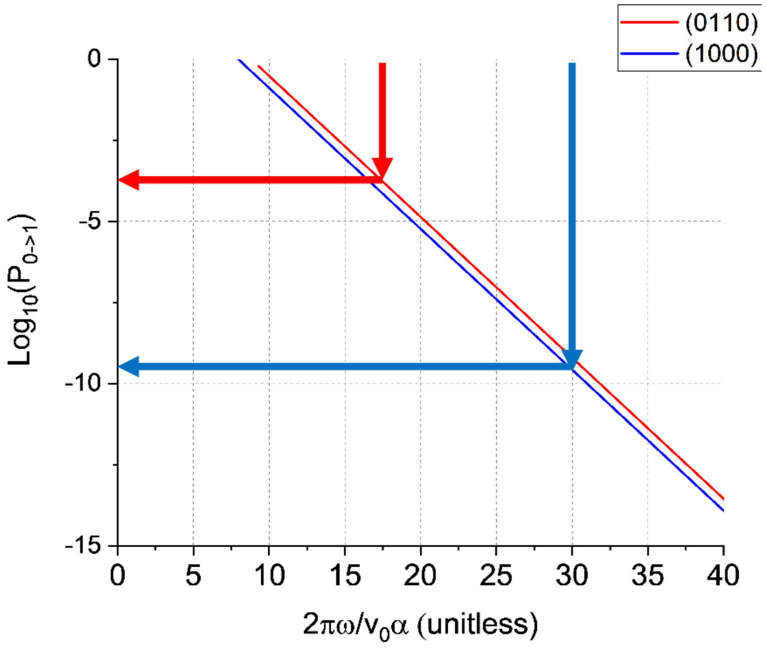

Figure 5.11: Examples of Landow-Teller probabilities vs. the velocity dependent exponent term.

the adiabatic limit and do not equilibrate with the surface temperature and ii) there can be easily 6 orders of magnitude difference between excitation probabilities for two low lying vibrations in the polyatomic.

5.5 Summary and Conclusion

In this paper, quantum state resolved collisional energy transfer of carbonyl sulfide (OCS) at the gas-liquid interface has been studied via molecular beam scattering and high resolution IR spectroscopy, which has permitted identification of rotational, vibrational and transverse Doppler excitation/accommodation of the projectile under low incident energy (E_{inc} = 2.2(4) kcal/mol) collision conditions. The results are found to be consistent with complete rotational and translational equilibration of the jet cooled OCS (T_{rot} = 10K) with the liquid surface over a variety of liquids (PFPE, squalene, and glycerol) and liquid temperatures (T_S = 263 K – 303K). By way of dramatic contrast, however, vibrational populations in the ground (00^00), v2 OCS bend (01^10) and v1 CS stretch (1000) modes for the scattered OCS species remain far out of equilibrium with the liquid surface, indeed remaining within experimental uncertainty at the exact same relative populations and vibrational temperatures observed in the incident OCS molecular beam. Clearly, the spectator nature of the vibrations requires that they be treated separately from the other degrees of freedom scatter along the TD pathway. This dynamically observed variation on the TD channel matches the expectations generated from simple physical intuition and the well known Landau-Teller vibrational energy transfer model. To understand this further, more work must be done exploring the vibrational dynamic at the gas liquid surface.

Chapter 5 References

1. Perkins, B. G.; Nesbitt, D. J., Quantum State-Resolved CO_2 Collisions at the Gas-Liquid Interface: Surface Temperature-Dependent Scattering Dynamics. *J. Phys. Chem. B* **2008**, *112*, 507-519.
2. Perkins, B. G.; Nesbitt, D. J., Stereodynamics at the Gas-Liquid Interface: Orientation and Alignment of CO2 Scattered from Perfluorinated Liquid Surfaces. *J. Phys. Chem. A* **2010**, *114*, 1398-1410.
3. Faust, J. A.; Nathanson, G. M., Microjets and Coated Wheels: Versatile Tools for Exploring Collisions and Reactions at Gas-Liquid Interfaces. *Chem. Soc. Rev.* **2016**, *45*, 3609-3620.
4. Tesa-Serrate, M. A.; Smoll, E. J.; Minton, T. K.; McKendrick, K. G., Atomic and Molecular Collisions at Liquid Surfaces. *Annu. Rev. Phys. Chem.* **2016**, *67*, 515-540.
5. Waring, C.; King, K. L.; Bagot, P. A. J.; Costen, M. L.; McKendrick, K. G., Collision Dynamics and Reactive Uptake of OH Radicals at Liquid Surfaces of Atmospheric Interest. *Phys. Chem. Chem. Phys.* **2011**, *13*, 8457-8469.
6. Hoffman, C. H.; Nesbitt, D. J., Quantum State Resolved 3D Velocity Map Imaging of Surface Scattered Molecules: Incident Energy Effects in HCl Plus Self-Assembled Monolayer Collisions. *J. Phys. Chem. C* **2016**, *120*, 16687-16698.
7. Perkins, B. G.; Nesbitt, D. J., High Resolution Dopplerimetry of Correlated Angular and Quantum State-Resolved CO_2 Scattering Dynamics at the Gas-Liquid Interface. *Phys. Chem. Chem. Phys.* **2010**, *12*, 14294-14308.
8. Perkins, B. G.; Nesbitt, D. J., Toward Three-Dimensional Quantum State-Resolved Collision Dynamics at the Gas-Liquid Interface: Theoretical Investigation of Incident Angle. *J. Phys. Chem. A* **2009**, *113*, 4613-4625.
9. Flynn, G. W.; Parmenter, C. S.; Wodtke, A. M., Vibrational Energy Transfer. *J. Phys. Chem.* **1996**, *100*, 12817-12838.
10. Nikitin, E. E.; Troe, J., 70 Years of Landau-Teller Theory for Collisional Energy Transfer. Semiclassical Three-Dimensional Generalizations of the Classical Collinear Model. *Phys. Chem. Chem. Phys.* **2008**, *10*, 1483-1501.
11. Ewing, G. E., Selection-Rules for Vibrational-Energy Transfer - Vibrational Predissociation of Vanderwaals Molecules. *J. Phys. Chem.* **1987**, *91*, 4662-4671.
12. Lau, J. A.; Schonemann, A. M.; Schwarzer, D.; Wodtke, A. M., The Coverage Dependence of the Infrared Absorption of Co Adsorbed to NaCl(100). *J. Chem. Phys.* **2020**, *153*.
13. Steinsiek, C.; Shirhattii, P. R.; Geweke, J.; Lau, J. A.; Altschaffel, J.; Kandratsenka, A.; Bartels, C.; Wodtke, A. M., Translational Inelasticity of NO and CO in Scattering from Ultrathin Metallic Films of Ag/Au(111). *J. Phys. Chem. C* **2018**, *122*, 18942-18948.
14. Wagner, R. J. V.; Henning, N.; Kruger, B. C.; Park, G. B.; Altschaffel, J.; Kandratsenka, A.; Wodtke, A. M.; Schafer, T., Vibrational Relaxation of Highly Vibrationally Excited Co Scattered from Au(111): Evidence for CO^- Formation. *J. Phys. Chem. Lett.* **2017**, *8*, 4887-4892.
15. Kruger, B. C.; Meyer, S.; Kandratsenka, A.; Wodtke, A. M.; Schafer, T., Vibrational Inelasticity of Highly Vibrationally Excited NO on Ag(111). *J. Phys. Chem. Lett.* **2016**, *7*, 441-446.
16. Golibrzuch, K.; Shirhatti, P. R.; Altschaffel, J.; Rahinov, I.; Auerbach, D. J.; Wodtke, A. M.; Bartels, C., State-to-State Time-of-Flight Measurements of NO Scattering from Au(111):

Direct Observation of Translation-to-Vibration Coupling in Electronically Nonadiabatic Energy Transfer. *J. Phys. Chem. A* **2013**, *117*, 8750-8760.

17. Shirhatti, P. R.; Rahinov, I.; Golibrzuch, K.; Werdecker, J.; Geweke, J.; Altschaffel, J.; Kumar, S.; Auerbach, D. J.; Bartels, C.; Wodtke, A. M., Observation of the Adsorption and Desorption of Vibrationally Excited Molecules on a Metal Surface. *Nat. Chem.* **2018**, *10*, 592-598.
18. Livingston Large, T. A.; Nesbitt, D. J., Low-Energy Co Scattering at the Gas-Liquid Interface: Experimental/Theoretical Evidence for a Novel Subthermal Impulsive Scattering (STIS) Channel. *J. Phys. Chem. C* **2020**, *124*, 28006-28017.
19. Livingston Large, T. A.; Nesbitt, D. J., Quantum State and Doppler-Resolved Scattering of Thermal/Hyperthermal Dci at the Gas-Liquid Interface: Support for a Simple "Lever Arm" Model of the Energy-Transfer Dynamics (Vol 123, Pg 3449, 2019). *J. Phys. Chem. C* **2019**, *123*, 14104-14104.
20. Perkins, B. G.; Nesbitt, D. J., Correlated Angular and Quantum State-Resolved CO2 Scattering Dynamics at the Gas-Liquid Interface. *J. Phys. Chem. A* **2008**, *112*, 9324-9335.
21. Perkins, B. G.; Nesbitt, D. J., Quantum-State-Resolved CO_2 Scattering Dynamics at the Gas-Liquid Interface: Incident Collision Energy and Liquid Dependence. *J. Phys. Chem. B* **2006**, *110*, 17126-17137.
22. Perkins, B. G.; Haber, T.; Nesbitt, D. J., Quantum State-Resolved Energy Transfer Dynamics at Gas-Liquid Interfaces: IR Laser Studies of CO_2 Scattering from Perfluorinated Liquids. *J. Phys. Chem. B* **2005**, *109*, 16396-16405.
23. Gisler, A. W.; Nesbitt, D. J., On Probing Ions at the Gas-Liquid Interface by Quantum State-Resolved Molecular Beam Scattering: The Curious Incident of the Cation in the Night Time. *Faraday Discuss.* **2012**, *157*, 297-305.
24. Proch, D.; Trickl, T., A High-Intensity Multi-Purpose Piezoelectric Pulsed Molecular-Beam Source. *Rev. Sci. Instrum.* **1989**, *60*, 713-716.
25. Lednovich, S. L.; Fenn, J. B., Absolute Evaporation Rates for Some Polar and Nonpolar Liquids. *AIChE. J.* **1977**, *23*, 454-459.
26. Rothman, L. S., et al., The Hitran Database - 1986 Edition. *Appl. Optics.* **1987**, *26*, 4058-4097.
27. Ryazanov, M.; Nesbitt, D. J., Quantum-State-Resolved Studies of Aqueous Evaporation Dynamics: NO Ejection from a Liquid Water Microjet. *J. Chem. Phys.* **2019**, *150*.
28. Landau, L.; Teller, E., Theory of Sound Dispersion. *Phys. Z. Sowjetunio* **1936**, *10*, 34-43.
29. Rapp, D., Complete Classical Theory of Vibrational Energy Exchange. *J. Chem. Phys.* **1960**, *32*, 735-737.

Chapter 6

Quantum State Resolved Scattering of Polyatomics at the Gas-Liquid Interface:

Hyperthermal vs. Thermal Vibrational Equilibrium Dynamics

6.1 Introduction

Due to high number densities, strong intermolecular interactions, and the rapid decay of short-range spatial order, the chemical physics of liquids remains extremely challenging, indeed arguably representing the most complex and least well understood of the three conventional phases of matter. As yet an even higher level of challenge and complexity has been the gas-liquid interface, which comprises a nanoscopically thin (a few Å) region between the liquid and the surrounding gas or vacuum. Though only a vanishingly small fraction of total molecules in any macroscopic liquid sample, this exceedingly thin interfacial region plays a crucial "gatekeeper" role, from thermal accommodation of gaseous projectiles colliding with the interface, to the fundamental physics of molecular solvation and subsequent chemical reaction in the bulk. It is against this massive level of dynamical complexity that the powerful laser spectroscopy and molecular beams tools of chemical physics can hope to push, in order to obtain hard-won new insights into (and ultimately molecular control over) the interfacial dynamics.

The past several decades have witnessed enormous experimental and theoretical progress in these directions. In particular, simple scattering of supersonic molecule beams at the gas-liquid interface and probing translational energies and angular distributions in the recoiling atoms/molecules by time-of flight (TOF) methods have proven extremely informative, as originally pioneered by Fenn and coworkers and elegantly exploited by the Nathanson, Morris, and Minton groups. Though such measurements are sensitive to the 3D translational degrees of freedom in the scattered molecular species, these studies revealed a remarkable and unexpected simplicity in the collision dynamics. Specifically, TOF distributions for projectiles scattered at the liquid interface exhibit what appear to be a clear bifurcation into two simple dynamical pathways.[1-5] One such pathway (trapping desorption, TD) is where the incident molecules/atoms are transiently trapped and thermally accommodate with the gas-liquid interface. By way of anthropomorphic analogy, the TD scattered projectile "loses all memory" of its initial conditions, such as internal quantum states (rotation, vibration, electronic, nuclear…), scalar translational energy E_{inc}, and vector velocity $\mathbf{v_{inc}}$. This TD pathway comprises molecules that eventually desorb back into the gas phase in a Boltzmann distribution, typically maintaining perfect *translational equilibrium* with bulk liquid temperature (T_S).

By way of contrast, these studies also clearly reveal a second component in the TOF distributions that comprise all *non-equilibrium* collision dynamics, often referred to as impulsive scattering (IS). In general, this represents a complementary pathway whereby molecules scatter from the gas-liquid interface while still maintaining some "memory" of its initial scattering conditions. Though simple enough to describe in words, this pathway can be operationally hard to define *a priori*, and therefore becomes measurable only in the context of a certain set of dynamical assumptions. In TOF studies, for example, the IS channel is characterized as the difference between i) experimentally observed fluxes and ii) the flux predicted for velocity distributions moving away from the interface and fully equilibrated to the liquid temperature (T_S), i.e.

$$I_{IS} = I_{exp} - I_{TS}. \qquad \text{Eq. 1}$$

Alternatively, in angle resolved studies with oblique angles of incidence, an azimuthally symmetric TD component can potentially be deconvolved from IS scattering distributions which might be more strongly forward peaked. To the extent that there is clean separation ("orthogonality") between such TD and IS components in the TOF distributions, this deconstruction is well-defined.

The fundamental challenge in studying gas-liquid interfacial dynamics with molecules is that diatomic and polyatomic scattering exhibits a much greater dynamical richness beyond that observed via simple translational TOF spectroscopy, specifically with additional opportunities for energy deposition/redistribution into quantum state resolved rotational, vibrational, and electronic degrees of freedom. Such experiments require probing with internal quantum state resolution, as offered by high resolution IR direct absorption spectroscopy, laser induced fluorescence, and/or resonance enhanced multiphoton ionization spectroscopy.

However, nature appears to have again offered another remarkable and unsuspected simplification. Specifically, measurements of rotational distributions for molecules scattered from a liquid interface at hyperthermal energies reveal a similar bifurcation into two dynamical pathways, i) the usual TD channel corresponding to linear Boltzmann plots and complete *equilibration* with the surface ($T_{TD} = T_S$), particularly at low collision energies and ii) a second channel (IS) associated with *non-equilibrium* rotational excitation dynamics. Both TD and IS pathways from hyperthermal scattering experiments have been successfully studied by a multitude of different techniques including direct absorption spectroscopy[2-3, 6-12], time of flight mass spectroscopy[4, 13-14] and REMPI+VMI[15], with studies mostly focused on the translational and rotational energy transfer with the surface. The existence of such a TD rotational channel can be additionally confirmed by temperature dependent studies of T_{TD} for a number of liquids, which often exhibit continuous equilibration between T_{TD} and T_S.

Interestingly, there is quite often (though until more systems have been studied, one can not claim this to be universal) an additional dynamical simplification, specifically that the IS rotations appear as hot but nevertheless thermal “Boltzmannesque” distributions at a hyperthermal temperature ($T_{IS} >> T_S$). Furthermore, for liquid-like self-assembled monolayer (SAMs) surfaces and molecular projectiles (HCl/DCl) amendable to REMPI detection via velocity map imaging (VMI) methods, there is also compelling agreement between temperatures measured via rotational and velocity distributions (perpendicular to the scattering plane) in each of the TD and IS channels. Indeed, the studies thus far would seem to suggest an even simpler physical picture of i) a collisional bifurcation into short-lived impulsive scattering (IS) and longer-lived trapping-desorption (TD) pathways, with ii) nearly complete equilibration in each of the TD/IS channels between rotation and translation degrees of freedom perpendicular to the scattering plane.

Although these results represent an extremely attractive characterization of collision dynamics at the gas-liquid interface, one should be indeed expect such simple pictures to break down under sufficiently detailed experimental scrutiny. We have seen, for example, that low energy scattering (E_{inc} = 2 kcal/mol) of very weakly interacting molecules such as CO or NO with liquids can exhibit interaction times too short to achieve full “rotational warming” up to T_S, a channel which might therefore be better described as “sub-thermal IS” rather than conventional equilibrium TD dynamics. We also have presented simple theoretical models that the hot yet Boltzmann-like IS rotational distributions of CO or NO observed at higher incident energies (E_{inc} = 20 kcal/mol) may reflect residual rainbow scattering dynamics that have been blurred due to averaging over, e.g., thermal roughness at the gas-liquid interface. These examples and exceptions obviously indicate the crucial need for testing such models for gas-liquid scattering into new and different dynamical regimes.

One such area which has remained relatively unexplored has been the dynamics of polyatomic vibrational energy transfer in collisions at the gas-liquid interface. Pioneering work on vibrational energy transfer of diatomics with surfaces has been achieved by the Wodke group[16-17], for which they report drastically different behavior between NO(v) and CO(v) projectiles on conducting vs. insulating surfaces. In particular, NO(v) is found to deposit multiple quanta of vibrational energy into Au(111) metal surfaces quite readily ($\Delta v > 10$), with only perturbative changes ($\Delta v = 0, 1$) observed for collisions from single crystal insulators such as NaCl. By way of contrast, vibrational energy transfer from CO(v) is found to be dramatically weaker for both metals and insulating materials ($\Delta v << 1$). Such disparities in vibrational energy transfer for NO(v) with metals vs. insulators have been rationalized by fundamental differences in chemical coupling with electrons inside the bulk metal. Specifically, by electron transfer from the metal, NO collisions can access a bound anionic state ($^3\Sigma^+$, NO^-), stabilized by Coulomb attraction to an (+) image charge in the metal surface, a pathway not available for either insulating single crystal surfaces or CO molecular projectiles. An alternate description proposed by Tully and coworkers is that vibrational spacings in the projectile can be perfectly resonant with a continuum of thermal electron hold pair excitations present in the metal. Conversely, this continuum of electron-hole pair excitations are not present in collisions with insulating species, thus greatly diminishing the efficiency of vibrational energy transfer. Thus it can be inferred from these studies that only molecules that interact strongly with the surface will undergo vibrational energy transfer.

Of particular relevance to the present study, work by the authors has shown that OCS interacting with the liquid surface at low collision energies does not undergo vibrational energy transfer. The vibrations act as spectators in the dynamics of the collision. This paper extends these previous studies into a high (~20 Kcal/mol) collision energy regime.

The remainder of this chapter is organized as follows. Sec. 6.2 provides some background experimental details on the polyatomic molecular beam spectrometer, with Sec. 6.3 presenting results and analysis for jet cooled OCS scattering from PFPE liquid at high incident energies (E_{inc} = 20(1) kcal/mol) and as a function of liquid temperature. Most importantly, the high energy results indicate strong vibrational adiabaticity in the collision dynamics, similar to what is seen at low collision energies, but now with an unexpected sensitivity to the temperature of the liquid. This is followed in Sec. 6.4 by discussion of the underlying vibrational collision dynamics as well as preliminary efforts to reproduce the observed experimental trends with molecular dynamics trajectory calculations based on high level ab initio scattering potentials. Sec. 6.5 completes the paper with a summary of the key results and identifies possible directions for further investigation.

6.2 Experimental

The gas-liquid scattering laser spectrometer apparatus used in this work for quantum state resolved scattering has been described elsewhere.[1, 18-19] It therefore suffices to offer a brief overview summary, with major focus on changes relevant to the present study. Our light source is an external cavity quantum cascade laser (Daylight Solutions), which can generate ~300 mW of single mode infrared light scanned under computer control over the 2000-2200 cm^{-1} spectral window with a linewidth of ~10 MHz. The studies take advantage of a cascading series of frequency measurements for spectral calibration, from a fizeau wavemeter (Bristol) for rough calibration, with signals transmitted through both an off-axis confocal Fabry Perot etalon (FSR = 250 MHz, finesse ~20-30) and a gas cell (0.5 Torr OCS, 5 cm path length) to measure relative frequency tuning during a scan as well as the absolute frequency from absorption lines in the reference gas cell. The internal quantum state (rovibrational) and translational Doppler profiles of the incident and scattered OCS are measured by shot-noise limited absorption methods, achieved via differential signal and reference beams on matched InSb detectors and with the signal beam executing a 16-fold multipass in the Harriot cell in the scattering vacuum chamber. By virtue of carefully balanced subtraction with fast analog electronics, the spectrometer achieves minimum absorbance sensitivities of order 1 x 10^{-5} in the bandwidth of the experiment for ~20 μW laser power on each detector, which is near the quantum limit.

The scattering system is made up of the molecular beam source, the scattering target and the multipass cell. Our beam source is of Proch and Trickl design[20]. A 5% OCS in a balance of hydrogen is expanded through a .508 mm orifice at a stagnation pressure of ~70 torr. Using a simple time of flight microphone setup, the average speed of the molecular beam pulse is measured to be 1700(70) m/sec. This gives the OCS an incident energy in the collision with the surface of 21(2) kcal/mol. Our molecular beam is oriented 65 degrees from the liquid surface normal. The rotational temperature of the beam is 10 K, and the vibrational temperature is 220(5) K fit from the ratio of the ground state to the two vibrational states.

Our scattering target is the temperature dependence setup described in reference. The liquid surface is prepared according to the method of Lednovich and Fenn[21], using a rotating (~ 0.2 Hz) bead blasted stainless steel wheel (12.7 cm diameter) half-submerged in the copper liquid reservoir and scraped with a stationary razor blade to present a thin (~500 um), freshly prepared gas-liquid surface to the impinging molecular beam. It is thermally isolated from the rest of the system using Teflon spacers. Its temperature is stabilized by a two-stage cooling apparatus. The bulk of the cooling/heating is done by an ethanol recirculating chiller. This backs a thermoelectric cooler that stabilizes the temperature of a thermistor epoxied to the front of the copper trough.

This study involve three different classes of liquids that sample different scattering dynamical regimes: 1) perfluorinated polyether, (PFPE, Krytox 1506, $F\text{-}[CF(CF_3)CF_2O)]_{14(avg)}\text{-}CF_2CF_3$), as prototype for a rough but chemically inert liquid surface, 2) squalane (2,6,10,15,19,23-hexamethyltetracosane, $C_{30}H_{62}$), as prototype for strongly hydrophobic surface, and 3) glycerol (1,2,3-propanetriol, $C_3H_8O_3$), as prototype for a highly hydrophilic surface due to multiple protruding OH groups. Each liquid is degassed under ~1 mTorr vacuum at room temperature for several hours to remove dissolved atmospheric gases, or at slightly elevated temperatures (~ 350 K) for the glycerol liquid samples to allow for more complete degassing within a reasonable time frame.

Each experiment consists of recording a 2 ms timetrace of the scattered gas pulse for each frequency step (3-7 MHz) over the appropriate frequency range for OCS of 2054.5 to ~2090 cm^{-1} where the scan is stopped when the signal drops below detectable limits. This scan range is broken up into smaller "continuous" step scans which are ~0.8 cm^{-1}. Each scan start is 0.7 cm^{-1} apart, leaving approximately .1 cm^{-1} overlap between each scan preventing gaps in the spectrum. Each time trace is turned into an absorbance by integrating over the rising edge of the gas pulse (300 us) and then subtracting the integrated baseline (300 us long taken 400 us before the start of the signal integration). The relative frequency axis of each scan is calculated from interpolating between the etalon peak maxima. This relative frequency is roughly calibrated by estimating the start frequency from measurements from the Bristol wavemeter. This absolute frequency is enhanced in precision by shifting the offset frequency to match our recorded reference thermal OCS spectrum to a thermal spectrum calculated from the Hitran database.[22]

6.3 Results and Analysis

To align each individual scan and to extract the quantum state resolved column integrated molecular densities, a global fit to all the scattering spectra is performed following a similar method to reference 23[23]. An example of this alignment can be seen in Fig 6.1. This fit has two key components, 1) a final adjustment of the frequency axis and 2) a model fit to the entire spectrum. The final adjustment to the frequency axis is a simple linear transformation where a global slope is varied to adjust for minute day to day changes is the etalon FSR (~10 ppb day to

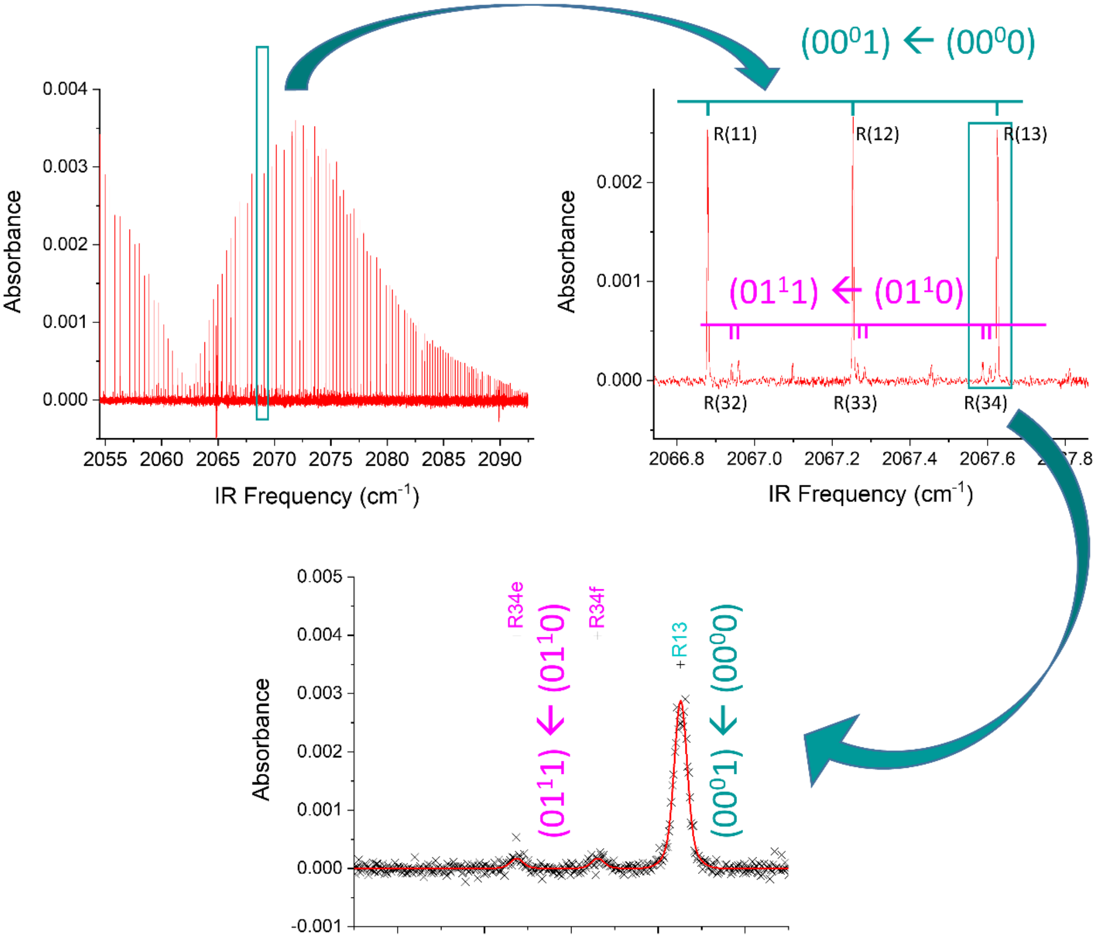

Figure 6.1 A full spectrum figure of OCS off PFPE at 20(1) kcal/mol with blowups showing more of the detailed spectrum. The largest blowup shows the spectral fit of the entire spectrum.

day variation). Each individual scan is also given a linear term to adjust for inaccuracies in the earlier rough calibrations.

The spectrum model assumes several things. First, each upper state of the spectroscopic transition is empty. This is a quite good approximation since the probing vibrational transition is ~2000 cm^{-1} above the ground state, which is inaccessible at the energies used in gas-liquid scattering. Secondly, the transition lineshape comes from a common gaussian velocity distribution. This model can be expressed as the following:

$$A(f_j) = \sum_i S_i(f_j) * P_i \qquad \text{Eq. 2}$$

Where $S_i(f_j)$ is the calculated spectrum from state i at frequency point f_j. The list of transitions and integrated cross-sections were obtained from the Hitran library. Only transitions

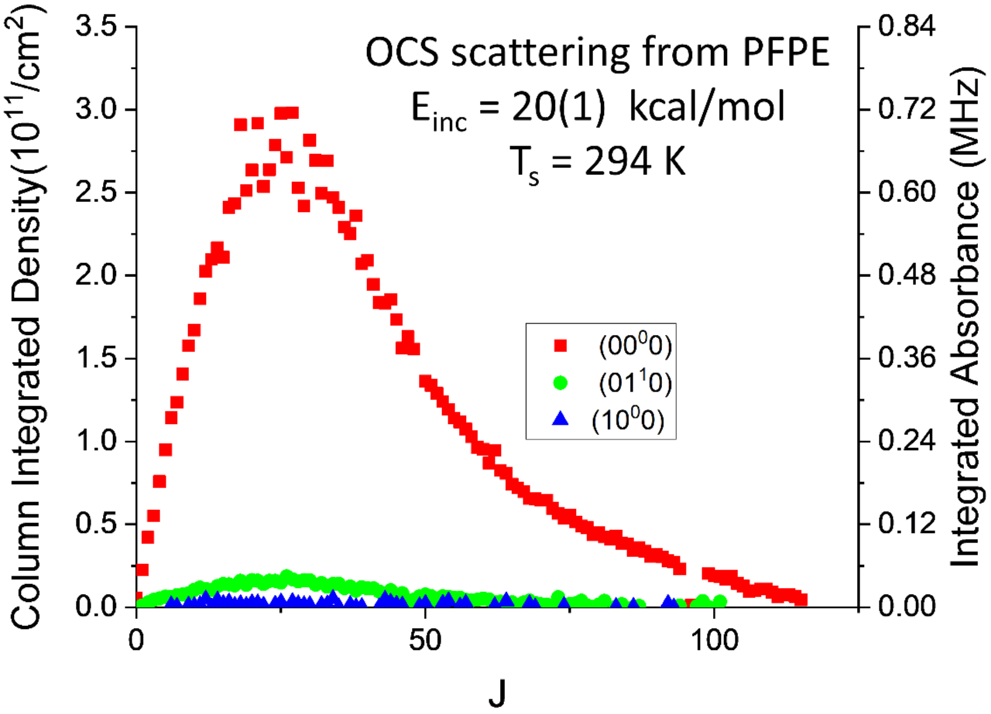

Figure 6.2 OCS population plot

from $^{16}O^{12}C^{32}S$ (94%) and 16O12C34S (4%) are considered. From fitting this model spectrum ($A(f_j)$) to the experimentally collected spectrum, the column integrated molecular densities (P_i) can be extracted. An example population distribution is seen in Fig 6.2. It is clear to see that we have a two temperature rotational distribution that has become expected from these type experiments. However, before we delve too deeply into these populations, we must acknowledge that these populations are only approximate since we fit a single width gaussian to a Doppler distribution made up of two different gaussian velocity distributions that have a varying weights across the spectrum, with the narrower distribution being concentrated at low rotational energies while a wider width dominates at higher rotational energies. Thus to truly understand this spectrum, we must generate a model of the scattering distributions and fit that to the entire spectrum. Our classic model used in several other gas-liquid scattering papers is as follows:

$$\frac{\mathrm{A(j,f,v)}}{\mathrm{S_{j,v}(2j+1)N}} = \alpha\, \mathrm{P_{rot}}(\mathrm{j}, \mathrm{T_{td}}_{rot})\mathrm{P_{trans}}(\mathrm{f}, \mathrm{T_{td}}_{vel}) + (1-\alpha)\mathrm{P_{rot}}(\mathrm{j}, \mathrm{T_{isrot}})\mathrm{P_{trans}}(\mathrm{f}, \mathrm{T_{is}}_{vel}) \text{ Eq. 3}$$

Where P_{rot} and P_{trans} are respectively a Boltzmann distribution for the rotational degrees of freedom and P_{trans} is a Maxwell-Boltzmann distribution describing the out of scatter plane speed distribution. This, however, does not cover the vibrational degrees of freedom. To understand this degree of freedom, let us look to Fig 6.3. In this figure, we see that the crossing point between the TD and IS components changes for each of the vibrational states (though this is mostly only visible for the difference between the ground state and the bend excited state). This is indicative of a different effective alpha for each vibrational state. Another way to view this is that instead of an

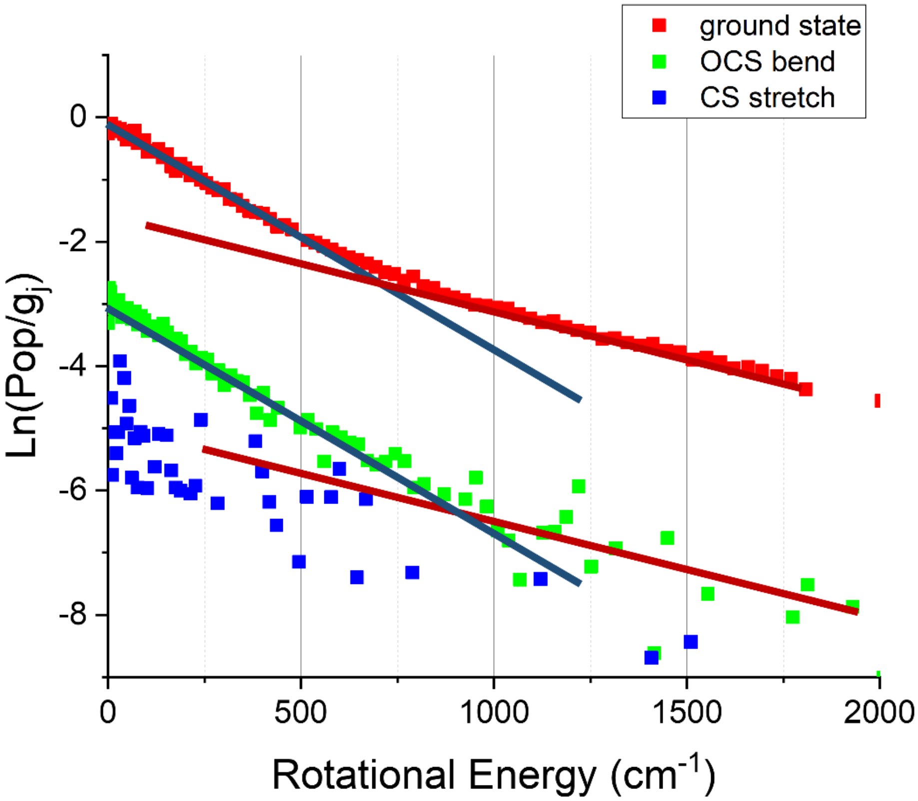

Figure 6.3 Rotational energy Boltzmann plot. The TD and IS lines intersect at different energies implying that there is an effective branching ratio difference in each vibrational state

individual alpha for each vibrational states, there is only one global branching ratio and that the TD and IS components have their own vibrational temperature. This is model is displayed below:

$$\frac{\mathrm{A(j,f,v)}}{\mathrm{S_{j,v}(2j+1)N}} = \alpha \mathrm{P_{rot}}(\mathrm{j}, \mathrm{T}_{\mathrm{td}rot})\mathrm{P_{trans}}(\mathrm{f}, \mathrm{T}_{\mathrm{td}vel})\mathrm{P}_{vib}(\mathrm{v}, \mathrm{T}_{tdvib}) \; +$$

$$(1-\alpha)\mathrm{P_{rot}}(\mathrm{j}, \mathrm{T_{isrot}})\mathrm{P_{trans}}(\mathrm{f}, \mathrm{T}_{isvel})\mathrm{P}_{vib}(\mathrm{v}, \mathrm{T}_{isvib}) \qquad \text{Eq. 4}$$

To use this model to extract information on the scattering, a fit is performed on the registered spectrum generated from the previous fitting method. This model can be fit to the spectrum floating all 8 parameter, but this leads to parameter correlation between alpha and the rotational and translation temperatures. In our previously published paper on low energy OCS scattering, it was seen that OCS rotationally accommodates with the surface. Thus to reduce parameter correlation, we fix the TD rotational and translational temperatures to the temperature of the surface. This does not change the fit vibrational temperatures by any statistical margin. A spectrum fit to this mode can be seen in Fig 6.1. The blowup highlights both the two temperature doppler profile but also the relative differences in signal to noise of the differing vibrational states.

To explore OCS's scattering dynamics, three difference liquids were used as scattering targets, PFPE, squalene, and glycerol. These scattering results are displayed in Fig 6.4. Ignoring the vibrational data, the scattering data agree with what has been seen before. Both the translations and rotations in the IS channel are much hotter than the surface temperature, with the translations scattering hotter than the rotational degrees of freedom. This is the same trend that has been seen with CO, H/DCl and CO_2 and to be expected for a molecular beam with translational energies ~30 times larger than kT.

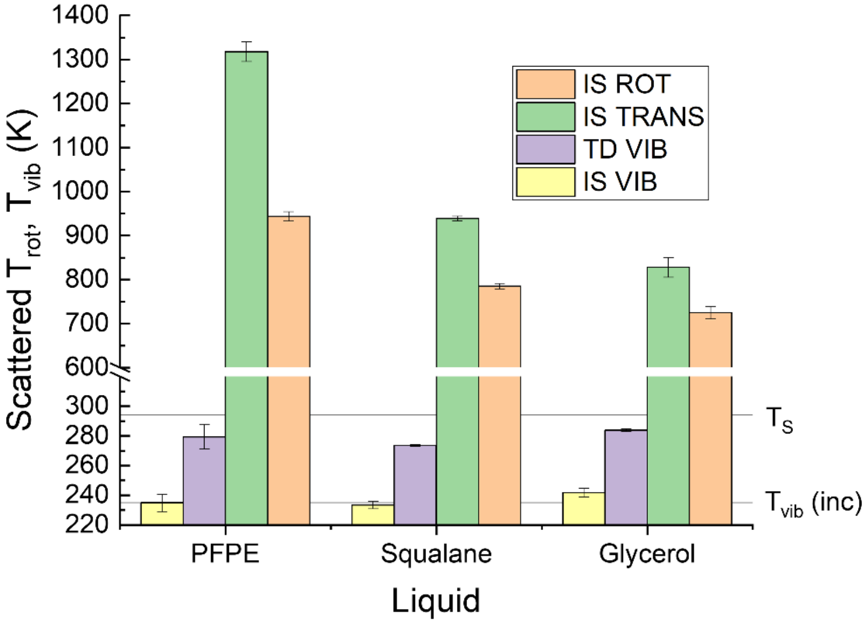

Figure 6.4 Summary of full spectrum fit parameters.

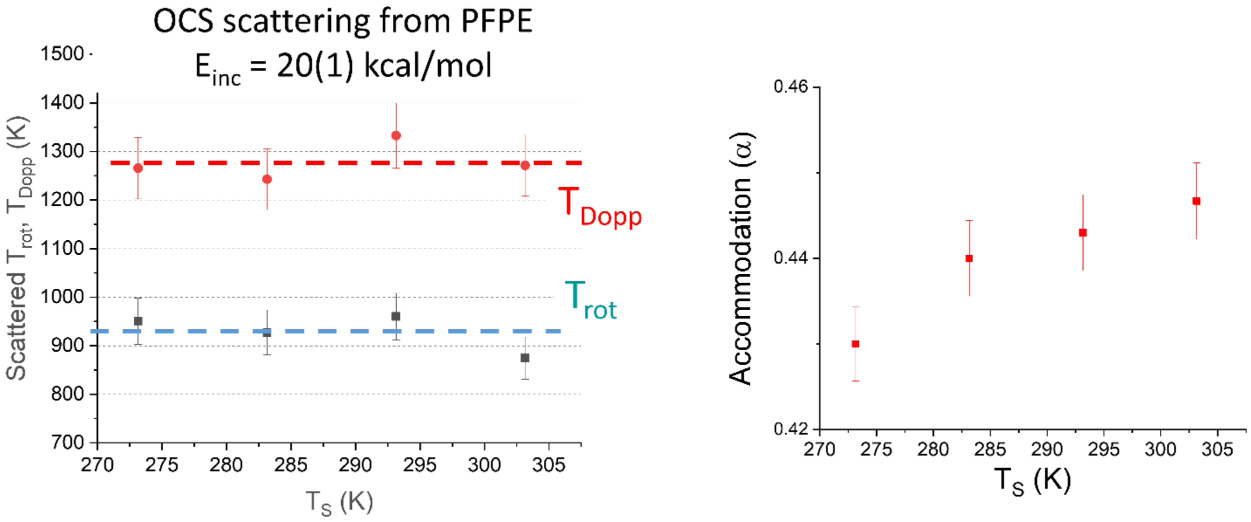

Figure 6.5 Scattering parameters as a function of surface temperature.

The most interesting part of this data is the vibrational temperatures. For the IS channel, we see what we have seen previously at the low collision energies. The vibrational temperature does not change from the incident conditions, showing us that no vibrational energy is transfered during the IS channel collisions. This is in stark contrast to what we see in the TD channel. We see the vibrational temperature rises from the much colder incident beam temperature to close to the surface temperature.

To explore this unexpected effect in greater detail, scattering data from pfpe was collected at a variety of surface temperatures. Fig 6.5a plots the temperature dependence of rotational and translational IS temperatures and the temperature dependence of the branching ratio. We can see from this figure that IS scattering temperature is quite insensitive to the surface temperature. This physically makes sense the total center of mass energy in the collision does not change by much while changing the surface temperature thus the outgoing average energy (i.e. the scattered “temperature”) does not change by much. Another observation that can be made for Fig 6.5b is that the branching ratio grows as the surface temperature increases. This has been seen previously with CO_2 and has been attributed to the increase in roughness of the surface as the temperature increases causing molecules to become trapped on the surface more easily.

The most remarkable piece of information from these temperature dependence studies is the dependence of the vibration scattered temperature on the surface temperature. Both the TD and IS vibrational temperatures are plotted in Fig 6.6. From this figure, we can see that the TD and IS components of the vibrational temperature behave very differently. We can see that the TD temperature rises from the incident beam temperature to near the temperature of the surface while tracking with the changes in the surface temperature. The IS component behaves as we saw in the energy scattering; it does not warm from the incident beams vibrational temperature. This is at first glance a surprising result. With high energy collisions, the impulsively scattered molecules

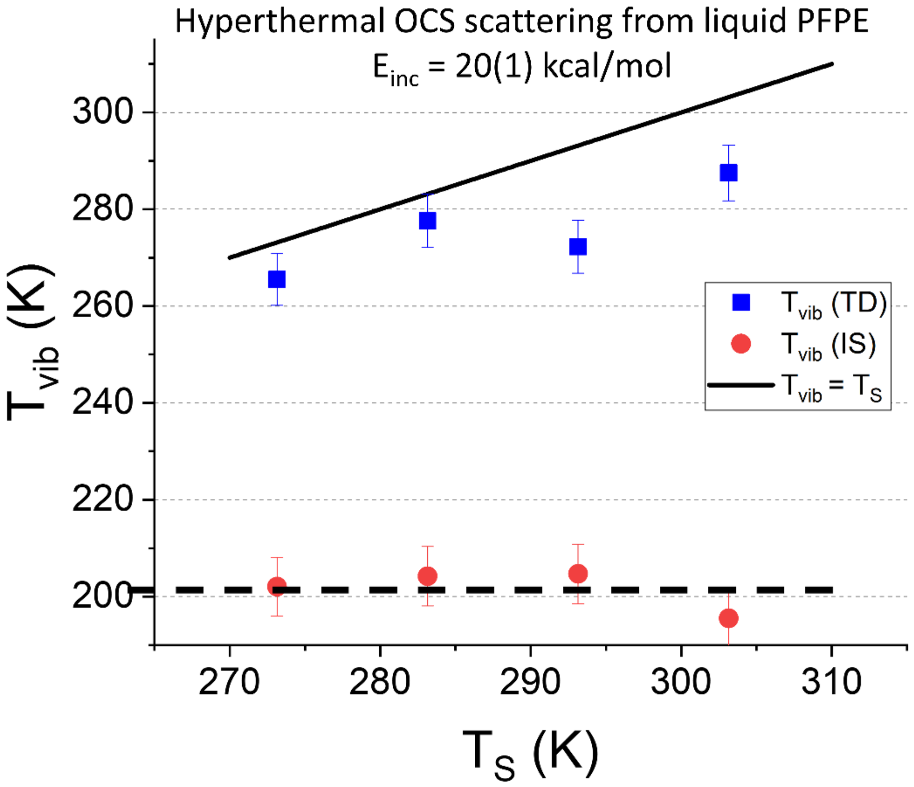

Figure 6.6 Vibrational temperatures of the TD and IS channels as a function of surface temperature.

behave more similarly to the low energy scattered TD channel, thus leaving the high energy scattered TD channel as the only channel that allows the possibility of vibrational energy transfer.

6.4 Discussion

One of the assumptions that has been made about the TD channel can be said colloquially as "molecules lose all memory of their initial conditions" when scattering via the TD channel. This has held true for many of the molecules studied especially for the translational and rotational degrees of freedom. For the vibrational degrees of freedom, this does not apply to scattering by OCS. As the beam energy changes, so too does the vibrational accommodation with the surface. Thus casting the TD channel into a static scattering channel underestimates the dynamics that go on and can clearly effect the scattering outcome.

To try and understand this, let us think about this physically. The only difference between the molecules that vibrational thermalize in the TD channel is the collision energy and thus the change in thermalization must be directly or indirectly resulting from this change. The general simplified mechanism of TD can be view as a three step mechanism of trap, thermalize and then desorb. Generally, by the time the molecules are trapped in the well and are thermalizing, there should be very little memory of the initial conditions of the molecule. Thus it must be that the change occurs as the molecule traps. This is not an outlandish idea. The difference in dissipating a kcal/mol or two of translational energy into the surface to trap the molecule is quite different from dissipating 20 kcal/mol into the surface. Arguably, this would lead to closer approaches to the molecules of the surface with the possibility of an increased chance of penetration into the surface. This would allow for very many secondary interactions with molecules that would not appear in the averaged interaction. All of these changes in the collision would increase the strength of the interaction and thus allowing for the OCS molecules to exchange vibrational energy with the surface.

Because we do not see vibrational energy transfer in the IS channel, we can be confident that it is not just the collision at these high energies that cause the vibrational energy transfer. Collisions at these energies still need to hit the system with specific “impact parameters” to allow these vibrations to exchange quanta. This highlights the discrete nature of the TD channel. Yet again we see this distinct two channel scattering with no continuum in between. A molecule either scatters from the surface impulsively, leaving the surface translationally and rotationally hot while no vibrational energy transfer occurs, or it can undergo a strong collision with the surface, dissipating enough of its translational energy to trap in the local van der Waals bound well and then thermalize with the surface (including the vibrational degrees of freedom).

To get to the bottom of this problem, more theory is necessary. Analysis similar to our previous work done with CO, except as a function of collision energy instead of surface temperature, should give deeper answers to what is occurring. However, that is for future work and not covered here.

6.5 Summary and Conclusions

In this paper, we have explored OCS scattering off liquids at energies many times kT. In this, both the rotational and translation degrees of freedom followed the empirical two temperature model. However, the vibrational degrees of freedom do not follow this behavior. It was seen that unlike the low energy studies, the TD channel of the scattering allowed the vibrations to approach thermalization while the hard hitting IS channel showed no vibrational energy transfer at all. This implies that the TD channel is not memoryless like previously thought but actually does have some dependence on the collision energy. This means that the in the future, one must also consider not just the thermal behavior of the TD channel, but also the possible dynamics for the degrees of freedom that do not so readily exchange energy with the surface.

Chapter 6 References

1. Livingston Large, T. A.; Nesbitt, D. J., Quantum State and Doppler-Resolved Scattering of Thermal/Hyperthermal Dcl at the Gas–Liquid Interface: Support for a Simple “Lever Arm” Model of the Energy-Transfer Dynamics. *J. Phys. Chem. C* **2019**, *123*, 3449-3460.
2. Perkins, B. G.; Nesbitt, D. J., High Resolution Dopplerimetry of Correlated Angular and Quantum State-Resolved CO_2 Scattering Dynamics at the Gas-Liquid Interface. *Phys. Chem. Chem. Phys.* **2010**, *12*, 14294-14308.
3. Perkins, B. G.; Nesbitt, D. J., Correlated Angular and Quantum State-Resolved CO_2 Scattering Dynamics at the Gas-Liquid Interface. *J. Phys. Chem. A* **2008**, *112*, 9324-9335.
4. Faust, J. A.; Nathanson, G. M., Microjets and Coated Wheels: Versatile Tools for Exploring Collisions and Reactions at Gas-Liquid Interfaces. *Chem. Soc. Rev.* **2016**, *45*, 3609-3620.
5. Tesa-Serrate, M. A.; Smoll, E. J.; Minton, T. K.; McKendrick, K. G., Atomic and Molecular Collisions at Liquid Surfaces. *Annu. Rev. Phys. Chem.* **2016**, *67*, 515-540.
6. Perkins, B. G.; Nesbitt, D. J., Quantum State-Resolved CO_2 Collisions at the Gas-Liquid Interface: Surface Temperature-Dependent Scattering Dynamics. *J. Phys. Chem. B* **2008**, *112*, 507-519.
7. Perkins, B. G.; Nesbitt, D. J., Stereodynamics at the Gas-Liquid Interface: Orientation and Alignment of CO_2 Scattered from Perfluorinated Liquid Surfaces. *J. Phys. Chem. A* **2010**, *114*, 1398-1410.
8. Zutz, A.; Nesbitt, D. J., Quantum State-Resolved Molecular Scattering of NO ($^2\Pi_{1/2}$) at the Gas-[$C_n$mim][Tf_2n] Room Temperature Ionic Liquid Interface: Dependence on Alkyl Chain Length, Collision Energy, and Temperature. *Aip. Adv.* **2016**, *6*.
9. Zutz, A.; Nesbitt, D. J., Nonadiabatic Spin-Orbit Excitation Dynamics in Quantum-State-Resolved NO($^2\Pi_{1/2}$) Scattering at the Gas-Room Temperature Ionic Liquid Interface. *J. Phys. Chem. C* **2015**, *119*, 8596-8607.
10. Ziemkiewich, M. P.; Zutz, A.; Nesbitt, D. J., Inelastic Scattering of Radicals at the Gas-Ionic Liquid Interface: Probing Surface Dynamics of Bmim-Cl, Bmim-BF_4, and Bmim-Tf_2n by Rovibronic Scattering of NO [$^2\Pi_{1/2}$ (0.5)]. *J. Phys. Chem. C* **2012**, *116*, 14284-14294.
11. Perkins, B. G.; Nesbitt, D. J., Quantum-State-Resolved CO_2 Scattering Dynamics at the Gas-Liquid Interface: Dependence on Incident Angle. *J. Phys. Chem. A* **2007**, *111*, 7420-7430.
12. Perkins, B. G.; Nesbitt, D. J., Quantum-State-Resolved CO_2 Scattering Dynamics at the Gas-Liquid Interface: Incident Collision Energy and Liquid Dependence. *J. Phys. Chem. B* **2006**, *110*, 17126-17137.
13. Muenter, A. H.; DeZwaan, J. L.; Nathanson, G. M., Collisions of Dcl with Pure and Salty Glycerol: Enhancement of Interfacial D -> H Exchange by Dissolved NaI. *J. Phys. Chem. B* **2006**, *110*, 4881-4891.
14. Nathanson, G. M., Molecular Beam Studies of Gas-Liquid Interfaces. *Annu. Rev. Phys. Chem.* **2004**, *55*, 231-255.
15. Hoffman, C. H.; Nesbitt, D. J., Quantum State Resolved 3D Velocity Map Imaging of Surface Scattered Molecules: Incident Energy Effects in HCl Plus Self-Assembled Monolayer Collisions. *J. Phys. Chem. C* **2016**, *120*, 16687-16698.
16. Wagner, R. J. V.; Kruger, B. C.; Park, G. B.; Wallrabe, M.; Wodtke, A. M.; Schafer, T., Electron Transfer Mediates Vibrational Relaxation of CO in Collisions with Ag(111). *Phys. Chem. Chem. Phys.* **2019**, *21*, 1650-1655.

17. Steinsiek, C.; Shirhattii, P. R.; Geweke, J.; Lau, J. A.; Altschaffel, J.; Kandratsenka, A.; Bartels, C.; Wodtke, A. M., Translational Inelasticity of NO and CO in Scattering from Ultrathin Metallic Films of Ag/Au(111). *J. Phys. Chem. C* **2018**, *122*, 18942-18948.
18. Livingston Large, T. A..; Nesbitt, D. J., Low-Energy CO Scattering at the Gas-Liquid Interface: Experimental/Theoretical Evidence for a Novel Subthermal Impulsive Scattering (STIS) Channel. *J. Phys. Chem. C* **2020**, *124*, 28006-28017.
19. Gisler, A. W.; Nesbitt, D. J., On Probing Ions at the Gas-Liquid Interface by Quantum State-Resolved Molecular Beam Scattering: The Curious Incident of the Cation in the Night Time. *Faraday Discuss.* **2012**, *157*, 297-305.
20. Proch, D.; Trickl, T., A High-Intensity Multi-Purpose Piezoelectric Pulsed Molecular-Beam Source. *Rev. Sci. Instrum.* **1989**, *60*, 713-716.
21. Lednovich, S. L.; Fenn, J. B., Absolute Evaporation Rates for Some Polar and Nonpolar Liquids. *AIChE. J.* **1977**, *23*, 454-459.
22. Rothman, L. S., et al., The Hitran Database - 1986 Edition. *Appl. Optics* **1987**, *26*, 4058-4097.
23. Ryazanov, M.; Nesbitt, D. J., Quantum-State-Resolved Studies of Aqueous Evaporation Dynamics: NO Ejection from a Liquid Water Microjet. *J. Chem. Phys.* **2019**, *150*.

Cumulative Bibliography

Adelman, S. A.; Doll, J. D., Generalized Langevin Equation Approach for Atom-Solid-Surface Scattering - General Formulation for Classical Scattering Off Harmonic Solids. *J. Chem. Phys.* **1976**, 64, 2375-2388.

Arthurs, A. M.; Dalgarno, A., The Theory of Scattering by a Rigid Rotator. P. Roy. Soc. *Lond. A MAT.* **1960**, 256, 540-551.

Arunan, E.; Setser, D. W.; Ogilvie, J. F., Vibration-Rotational Einstein Coefficients for HF DF and HCl DCl. *J. Chem. Phys.* **1992**, 97, 1734-1741.

Bagot, P. A. J.; Waring, C.; Costen, M. L.; McKendrick, K. G., Dynamics of Inelastic Scattering of OH Radicals from Reactive and Inert Liquid Surfaces. *J. Phys. Chem. C* **2008**, 112, 10868-10877.

Brastad, S. M.; Albert, D. R.; Huang, M. W.; Nathanson, G. M., Collisions of DCl with a Solution Covered with Hydrophobic and Hydrophilic Ions: Tetrahexylammonium Bromide in Glycerol. *J. Phys. Chem. A* **2009**, 113, 7422-7430.

Brastad, S. M.; Nathanson, G. M., Molecular Beam Studies of HCl Dissolution and Dissociation in Cold Salty Water. *Phys. Chem. Chem. Phys.* **2011**, 13, 8284-8295.

Brown, L. S.; Sibener, S. J., A Molecular-Beam Scattering Investigation of the Oxidation of CO on Rh(111) .2. Angular and Velocity Distributions of the CO_2 Product, *J. Chem. Phys.* **1989**, 90, 2807-2815.

Cavanagh, R. R.; King, D. S., Rotational-State and Spin-State Distributions - NO Thermally Desorbed from Ru(001), *Phys. Rev. Lett.* **1981**, 47, 1829-1832.

Chalasinski, G.; Szczesniak, M. M., State of the Art and Challenges of the Ab Initio Theory of Intermolecular Interactions, *Chem. Rev.* **2000**, 100, 4227-4252.

Chorny, I.; Benjamin, I.; Nathanson, G. M., Scattering, Trapping, and Ionization of HCl at the Surface of Liquid Glycerol. *J. Phys. Chem. B* **2004**, 108, 995-1002."

Cohen, S. R.; Naaman, R.; Balintkurti, G. G., Energy-Distribution between Spin-Orbit States in NO Scattered from Organized Amphiphilic Monolayers, *Chem. Phys. Lett.* **1988**, 152, 269-273.

Cohen, S. R.; Naaman, R.; Balintkurti, G. G., Investigation of NO Scattering from Organic Monolayers - Spin-Orbit State and Vibrational-State Population-Distributions, *Chem. Phys.* **1989**, 134, 119-126.

Coltrin, M. E.; Kay, B. D., Quasiclassical Trajectory Study of Rotational Energy-Transfer in the Scattering of NH3 from a Flat, Rigid Gold Surface. *J. Chem. Phys.* **1988**, 89, 551-561.

Curl, R. F.; Capasso, F.; Gmachl, C.; Kosterev, A. A.; McManus, B.; Lewicki, R.; Pusharsky, M.; Wysocki, G.; Tittel, F. K., Quantum Cascade Lasers in Chemical Physics. *Chem. Phys. Lett.* **2010**, 487, 1-18.

Davies, P. R.; Orville-Thomas, W. J., Infrared Band Intensities and Bond Polarities: Part I. Bond Moment Constants in CO_2, OCS, CS_2, CSe_2 and SCSe. *J. Mol. Struct.* **1969**, 4, 163-177.

Dempsey, L. P.; Brastad, S. M.; Nathanson, G. M., Interfacial Acid Dissociation and Proton Exchange Following Collisions of DCl with Salty Glycerol and Salty Water. *J. Phys. Chem. Lett.* **2011**, 2, 622-627.

Denner, F., Frequency Dispersion of Small-Amplitude Capillary Waves in Viscous Fluids. *Phys. Rev. E* **2016**, 94."

Denner, F.; Pare, G.; Zaleski, S., Dispersion and Viscous Attenuation of Capillary Waves with Finite Amplitude. Eur. Phys. *J.-Spec. Top.* **2017**, 226, 1229-1238.

DeZwaan, J. L.; Brastad, S. M.; Nathanson, G. M., Evidence for Interfacial $[FDCl]^-$ in Collisions between DCl and F^- in KF-Glycerol Solutions. *J. Phys. Chem. C* **2008**, 112, 15449-15457."

DeZwaan, J. L.; Brastad, S. M.; Nathanson, G. M., The Roles of Salt Concentration and Cation Charge in Collisions of Ar and DCl with Salty Glycerol Solutions of NaI and CaI_2. *J. Phys. Chem. C* **2008**, 112, 3008-3017."

Doll, J. D., Simple Classical Model for Scattering of Diatomic-Molecules from a Solid Surface. *J. Chem. Phys.* **1973**, 59, 1038-1042.

Ewing, G. E., Selection-Rules for Vibrational-Energy Transfer - Vibrational Predissociation of Vanderwaals Molecules. *J. Phys. Chem.* **1987**, 91, 4662-4671.

Faust, J. A.; Nathanson, G. M., Microjets and Coated Wheels: Versatile Tools for Exploring Collisions and Reactions at Gas-Liquid Interfaces. *Chem. Soc. Rev.* **2016**, 45, 3609-3620.

Faust, J. A.; Sobyra, T. B.; Nathanson, G. M., Gas-Microjet Reactive Scattering: Collisions of HCl and DCl with Cool Salty Water. *J. Phys. Chem. Lett.* **2016**, 7, 730-735.

Flynn, G. W., Collision-Induced Energy-Flow between Vibrational-Modes of Small Polyatomic-Molecules. *Accounts Chem. Res.* **1981**, 14, 334-341.

Flynn, G. W.; Parmenter, C. S.; Wodtke, A. M., Vibrational Energy Transfer. *J. Phys. Chem.* **1996**, 100, 12817-12838.

Gisler, A. W.; Nesbitt, D. J., On Probing Ions at the Gas-Liquid Interface by Quantum State-Resolved Molecular Beam Scattering: The Curious Incident of the Cation in the Night Time. *Faraday Discuss.* **2012**, 157, 297-305."

Golibrzuch, K.; Shirhatti, P. R.; Altschaffel, J.; Rahinov, I.; Auerbach, D. J.; Wodtke, A. M.; Bartels, C., State-to-State Time-of-Flight Measurements of NO Scattering from Au(111): Direct Observation of Translation-to-Vibration Coupling in Electronically Nonadiabatic Energy Transfer. *J. Phys. Chem. A* **2013**, 117, 8750-8760.

Graham, C.; Imrie, D. A.; Raab, R. E., Measurement of the Electric Quadrupole Moments of CO_2, CO, N_2, Cl_2 and BF_3, *Mol. Phys.* **1998**, 93, 49-56.

Grimme, S., Accurate Description of Van Der Waals Complexes by Density Functional Theory Including Empirical Corrections, *J. Comput. Chem.* **2004**, 25, 1463-1473.

H.-J. Werner; P. J. Knowles; R. Lindh; F. R. Manby; M. Sch?tz; P. Celani; T. Korona; A. Mitrushenkov; G. Rauhut; T. B. Adler; R. D. Amos; A. Bernhardsson; A. Berning; D. L. Cooper; M. J. O. Deegan; A. J. Dobbyn; F. Eckert; E. Goll; C. Hampel; G. Hetzer; T. Hrenar; G. Knizia; C. K÷ppl; Y. Liu; A. W. Lloyd; R. A. Mata; A. J. May; S. J. McNicholas; W. Meyer; M. E. Mura; A. Nickla; P. Palmieri; K. Pfl?ger; R. Pitzer; M. Reiher; U. Schumann; H. Stoll; A. J. Stone; R. Tarroni; T. Thorsteinsson; M. Wang; Wolf, A. Molpro, Version 2009.1, a Package of Ab Initio Programs, See Http://Www.Molpro.Net, 2009.

Hammerich, A. D.; Finlayson-Pitts, B. J.; Gerber, R. B., Mechanism for Formation of Atmospheric Cl Atom Precursors in the Reaction of Dinitrogen Oxides with HCl/Cl- on Aqueous Films. *Phys. Chem. Chem. Phys.* **2015**, 17, 19360-19370.

Hammerich, A. D.; Finlayson-Pitts, B. J.; Gerber, R. B., NOx Reactions on Aqueous Surfaces with Gaseous HCl: Formation of a Potential Precursor to Atmospheric Cl Atoms. *J. Phys. Chem. Lett.* **2012**, 3, 3405-3410.

Hase, W. L.; Duchovic, R.; Hu, X.; Komornicki, A.; Lim, K. F.; Lu, D.-H.; Peslherbe, G.; Swamy, K.; Vande Linde, S.; Varandas, A.; Wang, H. L.; Wolf, R. Venus96: A General Chemical Dynamics Computer Program Texas Tech University, Lubbock, TX, 2005.

Hepburn, J. W.; Northrup, F. J.; Ogram, G. L.; Polanyi, J. C.; Williamson, J. M., Rotationally Inelastic-Scattering from Surfaces - CO + LiF(001), *Chem. Phys. Lett.* **1982**, 85, 127-130.

Hill, J. G.; Peterson, K. A.; Knizia, G.; Werner, H. J., Extrapolating MP2 and CCSD Explicitly Correlated Correlation Energies to the Complete Basis Set Limit with First and Second Row Correlation Consistent Basis Sets, *J. Chem. Phys.* **2009**, 131, 194105.

Hoffman, C. H.; Nesbitt, D. J., Quantum State Resolved 3D Velocity Map Imaging of Surface Scattered Molecules: Incident Energy Effects in HCl Plus Self-Assembled Monolayer Collisions. *J. Phys. Chem. C* **2016**, 120, 16687-16698.

Huang, Y. H.; Rettner, C. T.; Auerbach, D. J.; Wodtke, A. M., Vibrational Promotion of Electron Transfer. *Science* **2000**, 290, 111-114.

Hurlbut, F. C.; Beck, D. E. ôU.C. *Eng. Proj. Report* He-150-166ö, 1959.

Iche, G.; Nozieres, P., Simple Stochastic Description of Desorption Rates. *J. Phys-Paris* **1976**, 37, 1313-1323.

Jungwirth, P.; Tobias, D. J., Ions at the Air/Water Interface. *J. Phys. Chem. B* **2002**, 106, 6361-6373.

King, M. E.; Fiehrer, K. M.; Nathanson, G. M.; Minton, T. K., Effects of Thermal Roughening on the Angular Distributions of Trapping and Scattering in Gas-Liquid Collisions. *J. Phys. Chem. A* **1997**, 101, 6556-6561.

King, M. E.; Nathanson, G. M.; Hanninglee, M. A.; Minton, T. K., Probing the Microscopic Corrugation of Liquid Surfaces with Gas-Liquid Collisions. *Phys. Rev. Lett.* **1993**, 70, 1026-1029.

Kleyn, A. W.; Luntz, A. C.; Auerbach, D. J., Rotational Energy-Transfer in Direct Inelastic Surface Scattering - NO on Ag(111). *Phys. Rev. Lett.* **1981**, 47, 1169-1172.

Knabe, K.; Williams, P. A.; Giorgetta, F. R.; Armacost, C. M.; Crivello, S.; Radunsky, M. B.; Newbury, N. R., Frequency Characterization of a Swept- and Fixed-Wavelength External-Cavity Quantum Cascade Laser by Use of a Frequency Comb. *Opt. Express* **2012**, 20, 12432-12442.

Kohler, S. P. K.; Reed, S. K.; Westacott, R. E.; McKendrick, K. G., Molecular Dynamics Study to Identify the Reactive Sites of a Liquid Squalane Surface. *J. Phys. Chem. B* **2006**, 110, 11717-11724.

Kolb, C. E., et al., An Overview of Current Issues in the Uptake of Atmospheric Trace Gases by Aerosols and Clouds. *Atmos. Chem. Phys.* **2010**, 10, 10561-10605.

Korsch, H. J.; Lewis, Z. V.; Poppe, D., On Classical Rotational Rainbow Structures for Initially Rotating Molecules. *Z. Phys. a-Hadron Nucl.* **1983**, 312, 277-284.

Korsch, H. J.; Richards, D., On Classical Rotational Rainbows. *J. Phys. B-at Mol. Opt.* **1981**, 14, 1973-1981.

Kroll, J. H.; Seinfeld, J. H., Chemistry of Secondary Organic Aerosol: Formation and Evolution of Low-Volatility Organics in the Atmosphere. *Atmos. Environ.* **2008**, 42, 3593-3624.

Kruger, B. C.; Meyer, S.; Kandratsenka, A.; Wodtke, A. M.; Schafer, T., Vibrational Inelasticity of Highly Vibrationally Excited NO on Ag(111). *J. Phys. Chem. Lett.* **2016**, 7, 441-446.

Kubiak, G. D.; Hurst, J. E.; Rennagel, H. G.; Mcclelland, G. M.; Zare, R. N., Direct Inelastic-Scattering of Nitric-Oxide from Clean Ag(111) - Rotational and Fine-Structure Distributions, *J. Chem. Phys.* **1983**, 79, 5163-5178.

Landau, L.; Teller, E., Theory of Sound Dispersion. *Phys. Z. Sowjetunio* **1936**, 10, 34-43.

Lau, J. A.; Schonemann, A. M.; Schwarzer, D.; Wodtke, A. M., The Coverage Dependence of the Infrared Absorption of Co Adsorbed to NaCl(100). *J. Chem. Phys.* **2020**, 153.

Lednovich, S. L.; Fenn, J. B., Absolute Evaporation Rates for Some Polar and Nonpolar Liquids. *AIChE. J.* **1977**, 23, 454-459.

Livingston Large, T. A.; Nesbitt, D. J., Low-Energy Co Scattering at the Gas-Liquid Interface: Experimental/Theoretical Evidence for a Novel Subthermal Impulsive Scattering (STIS) Channel. *J. Phys. Chem. C* **2020**, 124, 28006-28017.

Livingston Large, T. A.; Nesbitt, D. J., Quantum State and Doppler-Resolved Scattering of Thermal/Hyperthermal Dci at the Gas-Liquid Interface: Support for a Simple ""Lever Arm"" Model of the Energy-Transfer Dynamics (Vol 123, Pg 3449, 2019). *J. Phys. Chem. C* **2019**, 123, 14104-14104.

Lohr, J. R.; Day, B. S.; Morris, J. R., Scattering, Accommodation, and Trapping of HCl in Collisions with a Hydroxylated Self-Assembled Monolayer. *J. Phys. Chem. B* **2005**, 109, 15469-15475.

Martinez-Nunez, E.; Rahaman, A.; Hase, W. L., Chemical Dynamics Simulations of CO2 Scattering Off a Fluorinated Self-Assembled Monolayer Surface, *J. Phys. Chem. C* **2007**, 111, 354-364.

McClelland, G. M.; Kubiak, G. D.; Rennagel, H. G.; Zare, R. N., Determination of Internal-State Distributions of Surface Scattered Molecules - Incomplete Rotational Accommodation of NO on Ag(111), *Phys. Rev. Lett*. **1981**, 46, 831-834.

Miller, W. H., Coupled Equations and Minimum Principle for Collisions of an Atom and a Diatomic Molecule Including Rearrangements. *J. Chem. Phys.* **1969**, 50, 407.

Moore, C. B., Vibration-Rotation Energy Transfer. *J. Chem. Phys.* **1965**, 43, 2979.

Muenter, A. H.; DeZwaan, J. L.; Nathanson, G. M., Collisions of Dcl with Pure and Salty Glycerol: Enhancement of Interfacial D -> H Exchange by Dissolved NaI. *J. Phys. Chem. B* **2006**, 110, 4881-4891.

Nathanson, G. M., Molecular Beam Studies of Gas-Liquid Interfaces. *Annu. Rev. Phys. Chem.* **2004**, 55, 231-255.

Nelson, R. D.; Lide, D. R.; Maryott, A. A. Selected Values of Electric Dipole Moments for Molecules in the Gas Phase; U.S. National Bureau of Standards: Washington, 1967.

Neumark, D. M.; Wodtke, A. M.; Robinson, G. N.; Hayden, C. C.; Lee, Y. T., Molecular-Beam Studies of the $F+H_2$ Reaction. *J. Chem. Phys.* **1985**, 82, 3045-3066.

Nichols, W. L.; Weare, J. H., Homonuclear Diatomic Scattering from Solid-Surfaces - Hardcube Model. *J. Chem. Phys.* **1975**, 62, 3754-3762.

Nichols, W. L.; Weare, J. H., Rotational Energy-Distributions for Homonuclear Diatomic Beams Scattered from Solid-Surfaces - Hard-Cube Model. *J. Chem. Phys.* **1977**, 66, 1075-1078.

Nikitin, E. E.; Troe, J., 70 Years of Landau-Teller Theory for Collisional Energy Transfer. Semiclassical Three-Dimensional Generalizations of the Classical Collinear Model. *Phys. Chem. Chem. Phys.* **2008**, 10, 1483-1501.

Nizkorodov, S. A.; Harper, W. W.; Chapman, W. B.; Blackmon, B. W.; Nesbitt, D. J., Energy-Dependent Cross Sections and Nonadiabatic Reaction Dynamics in F($^2P_{3/2}$, $^2P_{1/2}$)+n-H_2 -> HF(v,J)+H. *J. Chem. Phys.* **1999**, 111, 8404-8416.

Nogueira, J. J.; Vazquez, S. A.; Mazyar, O. A.; Hase, W. L.; Perkins, B. G.; Nesbitt, D. J.; Martinez-Nunez, E., Dynamics of CO2 Scattering Off a Perfluorinated Self-Assembled Monolayer. Influence of the Incident Collision Energy, Mass Effects, and Use of Different Surface Models. *J. Phys. Chem. A* **2009**, 113, 3850-3865.

Oh-e, M.; Yokoyama, H.; Baldelli, S., Structure of the Glycerol Liquid/Vapor Interface Studied by Sum-Frequency Vibrational Spectroscopy, *Appl Phys Lett* **2004**, 84, 4965-4967.

Pack, R. T., Space-Fixed Vs Body-Fixed Axes in Atom-Diatomic Molecule Scattering - Sudden Approximations. *J Chem Phys* **1974**, 60, 633-639.

Park, G. B.; Kruger, B. C.; Meyer, S.; Kandratsenka, A.; Wodtke, A. M.; Schafer, T., An Axis-Specific Rotational Rainbow in the Direct Scatter of Formaldehyde from Au(111) and Its Influence on Trapping Probability. *Phys. Chem. Chem. Phys.* **2017**, 19, 19904-19915.

Perkins, B. G., Jr. Quantum State-Resolved Energy Transfer Dynamics at the Gas -Liquid Interface. Ph.D., University of Colorado at Boulder, Boulder, 2009.

Perkins, B. G.; Haber, T.; Nesbitt, D. J., Quantum State-Resolved Energy Transfer Dynamics at Gas-Liquid Interfaces: IR Laser Studies of CO_2 Scattering from Perfluorinated Liquids. *J. Phys. Chem. B* **2005**, 109, 16396-16405.

Perkins, B. G.; Nesbitt, D. J., Correlated Angular and Quantum State-Resolved CO_2 Scattering Dynamics at the Gas-Liquid Interface. *J. Phys. Chem. A* **2008**, 112, 9324-9335.

Perkins, B. G.; Nesbitt, D. J., High Resolution Dopplerimetry of Correlated Angular and Quantum State-Resolved CO_2 Scattering Dynamics at the Gas-Liquid Interface. *Phys. Chem. Chem. Phys.* **2010**, 12, 14294-14308.

Perkins, B. G.; Nesbitt, D. J., Quantum State-Resolved CO_2 Collisions at the Gas-Liquid Interface: Surface Temperature-Dependent Scattering Dynamics. *J. Phys. Chem. B* **2008**, 112, 507-519.

Perkins, B. G.; Nesbitt, D. J., Quantum-State-Resolved CO_2 Scattering Dynamics at the Gas-Liquid Interface: Dependence on Incident Angle, *J. Phys. Chem. A* **2007**, 111, 7420-7430.

Perkins, B. G.; Nesbitt, D. J., Quantum-State-Resolved CO_2 Scattering Dynamics at the Gas-Liquid Interface: Incident Collision Energy and Liquid Dependence, *J. Phys. Chem. B* **2006**, 110, 17126-17137.

Perkins, B. G.; Nesbitt, D. J., Quantum-State-Resolved CO_2 Scattering Dynamics at the Gas-Liquid Interface: Incident Collision Energy and Liquid Dependence. *J. Phys. Chem. B* **2006**, 110, 17126-17137.

Perkins, B. G.; Nesbitt, D. J., Stereodynamics at the Gas-Liquid Interface: Orientation and Alignment of CO_2 Scattered from Perfluorinated Liquid Surfaces. *J. Phys. Chem. A* **2010**, 114, 1398-1410.

Perkins, B. G.; Nesbitt, D. J., Stereodynamics in State-Resolved Scattering at the Gas-Liquid Interface. *P. Natl. Acad. Sci. USA* **2008**, 105, 12684-12689.

Perkins, B. G.; Nesbitt, D. J., Toward Three-Dimensional Quantum State-Resolved Collision Dynamics at the Gas-Liquid Interface: Theoretical Investigation of Incident Angle. *J. Phys. Chem. A* **2009**, 113, 4613-4625.

Peterson, K. A. Correlation Consistent Basis Sets. In Peterson Group Website http://tyr0.chem.wsu.edu/~kipeters/basis.html, 2019.

Peterson, K. A.; Dunning, T. H., Accurate Correlation Consistent Basis Sets for Molecular Core-Valence Correlation Effects: The Second Row Atoms Al-Ar, and the First Row Atoms B-Ne Revisited, *J. Chem. Phys.* **2002**, 117, 10548-10560.

Phillips, L. F., Velocity and Angular Distributions of Molecules Emitted from a Liquid Surface. *Chem. Phys. Lett*. **1997**, 266, 161-168.

Proch, D.; Trickl, T., A High-Intensity Multi-Purpose Piezoelectric Pulsed Molecular-Beam Source, *Rev. Sci. Instrum.* **1989**, 60, 713-716.

Rapp, D., Complete Classical Theory of Vibrational Energy Exchange. *J. Chem. Phys.* **1960**, 32, 735-737.

Rendulic, K. D., Sticking and Desorption - a Review. *Surf. Sci.* **1992**, 272, 34-44.

Rettner, C. T.; Auerbach, D. J.; Tully, J. C.; Kleyn, A. W., Chemical Dynamics at the Gas-Surface Interface. *J. Phys. Chem.* **1996**, 100, 13021-13033.

Rettner, C. T.; Schweizer, E. K.; Mullins, C. B., Desorption and Trapping of Argon at a 2H-W(100) Surface and a Test of the Applicability of Detailed Balance to a Nonequilibrium System. *J. Chem. Phys.* **1989**, 90, 3800-3813.

Ringeisen, B. R.; Muenter, A. H.; Nathanson, G. M., Collisions of DCl with Liquid Glycerol: Evidence for Rapid, near-Interfacial D -> H Exchange and Desorption, J. *Phys. Chem. B* **2002**, 106, 4999-5010.

Ringeisen, B. R.; Muenter, A. H.; Nathanson, G. M., Collisions of HCl, DCl, and HBr with Liquid Glycerol: Gas Uptake, D -> H Exchange, and Solution Thermodynamics, *J. Phys. Chem. B* **2002**, 106, 4988-4998.

Rothman, L. S., et al., The Hitran Database - 1986 Edition. *Appl. Optics* **1987**, 26, 4058-4097.

Ryazanov, M.; Nesbitt, D. J., Quantum-State-Resolved Studies of Aqueous Evaporation Dynamics: NO Ejection from a Liquid Water Microjet. *J. Chem. Phys.* **2019**, 150.

Saecker, M. E.; Nathanson, G. M., Bouncing Gases Off Liquids - Collisions of Protic and Aprotic Solutes with Hydrocarbon and Hydrogen-Bonding Solvents. *Abstr. Pap. Am. Chem. S.* **1992**, 203, 237-Phys.

Saecker, M. E.; Nathanson, G. M., Collisions of Protic and Aprotic Gases with a Perfluorinated Liquid. *J. Chem. Phys.* **1994**, 100, 3999-4005.

Saecker, M. E.; Nathanson, G. M., Collisions of Protic and Aprotic Gases with Hydrogen-Bonding and Hydrocarbon Liquids. *J. Chem. Phys.* **1993**, 99, 7056-7075.

Schinke, R., Rotational Rainbows in Diatom (Solid) Surface Scattering. *J. Chem. Phys.* **1982**, 76, 2352-2359.

Shirhatti, P. R.; Rahinov, I.; Golibrzuch, K.; Werdecker, J.; Geweke, J.; Altschaffel, J.; Kumar, S.; Auerbach, D. J.; Bartels, C.; Wodtke, A. M., Observation of the Adsorption and Desorption of Vibrationally Excited Molecules on a Metal Surface. *Nat. Chem.* **2018**, 10, 592-598.

Steinsiek, C.; Shirhattii, P. R.; Geweke, J.; Lau, J. A.; Altschaffel, J.; Kandratsenka, A.; Bartels, C.; Wodtke, A. M., Translational Inelasticity of NO and CO in Scattering from Ultrathin Metallic Films of Ag/Au(111). *J. Phys. Chem. C* **2018**, 122, 18942-18948.

Tesa-Serrate, M. A.; Smoll, E. J.; Minton, T. K.; McKendrick, K. G., Atomic and Molecular Collisions at Liquid Surfaces, *Annual Review of Physical Chemistry* **2016**, 67, 515-540.

Tully, J. C., Dynamics of Gas Surface Interactions - Thermal-Desorption of Ar and Xe from Platinum, *Surf. Sci.* **1981**, 111, 461-478.

Tully, J. C., The Dynamics of Adsorption and Desorption. *Surf. Sci*. **1994**, 299, 667-677.
Tully, J. C., Washboard Model of Gas Surface Scattering, *J. Chem. Phys.* **1990**, 92, 680-686.
Van Willigen, W., Angular Distribution of Hydrogen Molecules Desorbed from Metal Surfaces, *Phys. Lett. A* **1968**, 28, 80-81.
Vandoren, J. M.; Watson, L. R.; Davidovits, P.; Worsnop, D. R.; Zahniser, M. S.; Kolb, C. E., Temperature-Dependence of the Uptake Coefficients of HNO_3, HCl, and N_2O_5 by Water Droplets. *J Phys. Chem* **1990**, 94, 3265-3269.
Vanduijneveldt, F. B.; Vanduijneveldtvanderijdt, J.; Vanlenthe, J. H., State-of-the-Art in Counterpoise Theory, *Chem. Rev.* **1994**, 94, 1873-1885.
Wagner, R. J. V.; Henning, N.; Kruger, B. C.; Park, G. B.; Altschaffel, J.; Kandratsenka, A.; Wodtke, A. M.; Schafer, T., Vibrational Relaxation of Highly Vibrationally Excited CO Scattered from Au(111): Evidence for CO^- Formation. *J. Phys. Chem. Lett.* **2017**, 8, 4887-4892.
Wagner, R. J. V.; Kruger, B. C.; Park, G. B.; Wallrabe, M.; Wodtke, A. M.; Schafer, T., Electron Transfer Mediates Vibrational Relaxation of CO in Collisions with Ag(111). *Phys. Chem. Chem. Phys.* **2019**, 21, 1650-1655.
Waring, C.; King, K. L.; Bagot, P. A. J.; Costen, M. L.; McKendrick, K. G., Collision Dynamics and Reactive Uptake of OH Radicals at Liquid Surfaces of Atmospheric Interest. *Phys. Chem. Chem. Phys.* **2011**, 13, 8457-8469.
Watson, L. R.; Vandoren, J. M.; Davidovits, P.; Worsnop, D. R.; Zahniser, M. S.; Kolb, C. E., Uptake of HCl Molecules by Aqueous Sulfuric-Acid Droplets as a Function of Acid Concentration. *J. Geophys. Res.-Atmos.* **1990**, 95, 5631-5638.
Weida, M. J.; Caffey, D.; Rowlette, J. A.; Arnone, D. F.; Day, T., Utilizing Broad Gain Bandwidth in Quantum Cascade Devices, *Opt. Eng.* **2010**, 49, 111120.
Wenaas, E. P., Equilibrium Cosine Law and Scattering Symmetry at Gas-Surface Interface. *J. Chem. Phys.* **1971**, 54, 376.
Whitely, T. W. J.; McCaffery, A. J., Angular Momentum Analysis of Rotational Transfer of Superthermal Relative Velocity Distributions. *J. Phys. B-At. Mol. Opt*. **1996**, 29, 6133-6141.
Wiens, J. P.; Nathanson, G. M.; Alexander, W. A.; Minton, T. K.; Lakshmi, S.; Schatz, G. C., Collisions of Sodium Atoms with Liquid Glycerol: Insights into Solvation and Ionization. *J. Am. Chem. Soc*. **2014**, 136, 3065-3074.
Worsnop, D. R.; Zahniser, M. S.; Kolb, C. E.; Vandoren, J.; Davidovits, P., Uptake of Gaseous HNO_3, N_2O_5, and HCl into Sulfuric-Acid Droplets. *Abstr. Pap. Am. Chem. S.* **1990**, 200, 122-Phys.
Wu, B. H.; Zhang, J. M.; Minton, T. K.; McKendrick, K. G.; Slattery, J. M.; Yockel, S.; Schatz, G. C., Scattering Dynamics of Hyperthermal Oxygen Atoms on Ionic Liquid Surfaces: [emim][NTf2] and [C12mim][NTf2]. *J. Phys. Chem. C* **2010**, 114, 4015-4027.
Xie, X. W.; Li, Y.; Liu, Z. Q.; Haruta, M.; Shen, W. J., Low-Temperature Oxidation of CO Catalysed by Co_3O_4 Nanorods. *Nature* **2009**, 458, 746-749.
Yan, T. Y.; Hase, W. L., Origin of the Boltzmann Translational Energy Distribution in the Scattering of Hyperthermal Ne Atoms Off a Self-Assembled Monolayer, *Phys. Chem. Chem. Phys.* **2000**, 2, 901-910.
Yin; Liebscher, J., Carbon-Carbon Coupling Reactions Catalyzed by Heterogeneous Palladium Catalysts. *Chem. Rev.* **2007**, 107, 133-173.

Zhang, J. M.; Garton, D. J.; Minton, T. K., Reactive and Inelastic Scattering Dynamics of Hyperthermal Oxygen Atoms on a Saturated Hydrocarbon Surface. *J. Chem. Phys*. **2002**, 117, 6239-6251.

Zhang, J. M.; Upadhyaya, H. P.; Brunsvold, A. L.; Minton, T. K., Hyperthermal Reactions of O and O_2 with a Hydrocarbon Surface: Direct C-C Bond Breakage by O and H-Atom Abstraction by O_2, *J. Phys. Chem. B* **2006**, 110, 12500-12511."

Ziemkiewich, M. P.; Zutz, A.; Nesbitt, D. J., Inelastic Scattering of Radicals at the Gas-Ionic Liquid Interface: Probing Surface Dynamics of Bmim-Cl, Bmim-BF4, and Bmim-Tf_2n by Rovibronic Scattering of NO [$^2\Pi_{1/2}$ (0.5)]. *J. Phys. Chem. C* **2012**, 116, 14284-14294.

Ziemkiewicz, M. P.; Roscioli, J. R.; Nesbitt, D. J., State-to-State Dynamics at the Gas-Liquid Metal Interface: Rotationally and Electronically Inelastic Scattering of NO[$^2\Pi_{1/2}$ (0.5)] from Molten Gallium. *J. Chem. Phys*. **2011**, 134.

Ziemkiewicz, M. P.; Zutz, A.; Nesbitt, D. J., Inelastic Scattering of Radicals at the Gas-Ionic Liquid Interface: Probing Surface Dynamics of Bmim-Cl, Bmim-BF4, and Bmim-Tf2n by Rovibronic Scattering of NO ($^2\Pi_{1/2}$ (0.5)), *J. Phys. Chem. C* **2012**, 116, 14284-14294.

Zutz, A.; Nesbitt, D. J., Nonadiabatic Spin-Orbit Excitation Dynamics in Quantum-State-Resolved NO($^2\Pi_{1/2}$) Scattering at the Gas-Room Temperature Ionic Liquid Interface. *J. Phys. Chem. C* **2015**, 119, 8596-8607.

Zutz, A.; Nesbitt, D. J., Quantum State-Resolved Molecular Scattering of NO ($^2\Pi_{1/2}$) at the Gas-[$C_n$mim][Tf_2n] Room Temperature Ionic Liquid Interface: Dependence on Alkyl Chain Length, Collision Energy, and Temperature, *AIP Adv.* **2016**, 6, 105207.

Appendix A

Quantum State and Doppler Resolved Scattering of Thermal/Hyperthermal DCl at the Gas-Liquid Interface: Support for a Simple “Lever Arm” Model of the Energy Transfer Dynamics

Supporting Information

This derivation follows the general form as presented in the Phillips work. Changes have been made to add clarity and rigor to the derivation. As can be seen in the previous work done on thermal capillary waves, the surface height (h) can be described approximately as a being bounded with periodic boundary conditions in a box with side lengths of L which is half the wavelength in which capillary waves are superseded by gravity waves. Solving the standard thermal capillary Hamiltonian gives the following solution for the thermally averaged height of the interface.

$$h(x,y) = \sum_{n,m=1}^{N} \sqrt{\frac{2\,k_b T}{L^2\,\gamma\,(k_{x,n}^2 + k_{y,m}^2)}} \cos(k_{x,n}x + \phi_n)\cos(k_{y,m}y + \phi_m) \qquad \text{Eq. 1}$$

where gamma is the surface tension and phi is a uniformly distributed random phase. The sum is from 1 to N where 1 is equivalent to the smallest allowed momentum and N is the largest. Since the momentum in both the x and y direction can be considered an integer multiple of the smallest momentum allowed in our box, we can make the following substitution.

$$k_{x,n} = \frac{2\,\pi}{L} n \qquad \text{Eq. 2}$$

Thus:

$$h(x,y) = \sum_{n,m=1}^{N} \sqrt{\frac{2\,k_b T}{(2\,\pi)^2\,\gamma\,(n^2 + m^2)}} \cos\left(n\,\frac{2\pi}{L}\,x + \phi_n\right)\cos\left(m\,\frac{2\pi}{L} y + \phi_m\right) = \sum_{n,m=1}^{N} h_{n,m} \qquad \text{Eq. 3}$$

N now can be seen as L/σ where sigma is the smallest allowed distance which in this case is the molecular diameter of the surface molecules. Let us now look at the derivatives of each of the individual mode of this sum.

$$\partial_x h_{n,m} = -\sqrt{\frac{2\, k_b T\, n^2}{L^2\, \gamma\, (n^2+m^2)}} \sin(n\, \frac{2\pi}{L}\, x + \phi_n) \cos(m\, \frac{2\pi}{L} y + \phi_m) \qquad \text{Eq. 4}$$

Averaging over both x and y, we see that:

$$\langle \partial_x h_{n,m} \rangle = 0 \qquad \text{Eq.5}$$

$$\langle \left(\partial_x h_{n,m}\right)^2 \rangle = \frac{n^2}{n^2+m^2}\, \frac{k_b T}{L^2\, \gamma} \qquad \text{Eq. 6}$$

This can be restated as the mean of each of these modes is zero and the variance is finite and known. Since each surface mode has a know and finite mean and a known and finite variance, when they are add together with a randomly distributed phase, the central limit theorem says that the sum of these randomly distributed variables tends to a gaussian distribution. This gaussian has a zero mean and a variance defined as:

$$\sigma^2 = \sum_{n,m=1}^{\sqrt{N}} \frac{n^2}{n^2+m^2}\, \frac{k_b T}{L^2\, \gamma} = \frac{N}{2}\, \frac{k_b T}{L^2\, \gamma} \qquad \text{Eq. 7}$$

Which is the same as the variance derived in the Phillips' work. Notice the change of the sum from N to $\sqrt{N}$. This was done to keep in line with Phillips' paper, which defined N as the total number of modes in a L x L box.

ProQuest LLC
789 East Eisenhower Parkway
P.O. Box 1346
Ann Arbor, MI 48106 - 1346 USA